INTEGRATED AND MINIATURIZED ENDOSCOPIC DEVICES FOR USE DURING HIGH POWER INFRARED FIBER LASER SURGERY

by

Christopher Ryan Wilson

A dissertation paper submitted to the faculty of
The University of North Carolina at Charlotte
in partial fulfillment of the requirements
for the degree of Doctor of Philosophy in
Optical Science and Engineering

Charlotte

2016

Approved by:

_____
Dr. Nathaniel M. Fried

_____
Dr. Michael A. Fiddy

_____
Dr. Gregory J. Gbur

_____
Dr. Susan R. Trammell

_____
Dr. Gloria D. Elliot

ABSTRACT

CHRISTOPHER RYAN WILSON. Integrated and miniaturized endoscopic devices for use during high power infrared fiber laser surgery. (Under the direction of DR. NATHANIEL M. FRIED)

The Thulium Fiber Laser (TFL) is currently being studied as a potential alternative to the conventional, solid-state Holmium:YAG laser (Ho:YAG) for the treatment of kidney stones. The TFL is an ideal candidate to replace the Ho:YAG for laser lithotripsy due to a higher absorption coefficient in water of the emitted wavelength, an ability to operate at high pulse rates, and a near single mode, Gaussian spatial beam profile.

The higher absorption of the TFL wavelength by water translates to a decrease in ablation threshold by a factor of four. High pulse rate operation allows higher ablation rates than the Ho:YAG, thus decreasing operation time necessary to ablate the urinary stone.

The Gaussian spatial beam profile allows the TFL to couple higher laser power into smaller optical fibers than those currently being used for Ho:YAG lithotripsy. This decrease in fiber diameter translates into a potential decrease in the size of ureteroscope working channel, higher saline irrigation rates for improved visibility and safety, and may also extend to a decrease in overall ureteroscope diameter. Furthermore, the improved spatial beam profile reduces the risk of damage to the input end of the fiber. Therefore, the trunk fiber, minus the distal fiber tip, may be preserved and re-used, resulting in significant cost savings.

This thesis details rapid TFL lithotripsy at high pulse rates up to 500 Hz, both with and without the aid of a stone retrieval basket, in order to demonstrate the TFL's superior ablation rates over the Ho:YAG. Collateral damage testing of the TFL effect on the ureter

wall and Nitinol stone baskets were conducted to ensure patient safety for future clinical use. Proximal fiber end damage testing was conducted to demonstrate fiber preservation, critical for permanent fiber integration. Optical fibers were fitted with fabricated hollow steel tips and integrated with stone retrieval baskets for testing. Ball tipped optical fibers were tested to maintain ablation rates comparable to those of the 100-µm-core traditional fiber used in TFL lithotripsy while providing an additional safety feature for initial fiber insertion through the ureteroscope working channel.

Working channel flow rates were explored in regards to diameter and geometry. Illumination sources and configurations were explored in regards to optimized wavelength selection as well as physical geometry of the ureteroscope tip. Ureteroscope designs were devised, modeled, fabricated, and tested, implementing a reduced working channel, and optimized illumination geometry, culminating in an integrated, miniaturized ureteroscope for use in TFL lithotripsy. This final device, coupled with the proven TFL and optimized laser parameters may establish the TFL as a viable replacement to the conventional Ho:YAG laser for treatment of kidney stones.

DEDICATION

This body of work is dedicated…

To my Father and Grandfathers, who taught me how to be the man I am

To my Mother and Grandmothers who nurtured and supported me selflessly

To my Brother, my consigliere and confidant,
who taught me to pursue my dreams wherever they may take me

"*Non Illegitimīs Carborundum*"

To my Hailey, the love of my life, my other half, and my rock,
without whom I never could have accomplished so much

To all who believed in me

It is through you that I truly stand on the shoulder of giants.

ACKNOWLEDGMENTS

I would like to thank Dr. Nathaniel Fried, my advisor, for his continued support and guidance through my research and academic studies. I also appreciate the Graduate Assistant Support Plan (GASP) and Lucille P. and Edward C. Giles Dissertation-Year Graduate Fellowship provided by the graduate school at UNC Charlotte, the travel funding provided by the Center for Biomedical Engineering and Science, the mini grant provided by the Office of Technology and Licensing.

I would like to thank all of my fellow Biomedical Optics Laboratory members and members of other laboratories who have provided insight and assistance throughout my graduate career: Dr. Thomas Hutchens, Dr. Richard Blackmon, William Perkins, Luke Hardy, Chun-Hung (Jack) Chang, Joshua Kennedy, Dr. Kenneth Allen, Dr. Jason Case, Joseph Peller, Frances Bodrucki, Charlotte Stahl, Jason Shultz, and Geoffrey Tuttle.

I would like to thank Dr. Pierce Irby, Director of the Carolinas Kidney Stone Center and an urologist in the McKay Department of Urology at Carolinas Medical Center, for helpful discussions on laser lithotripsy and novel endoscope designs.

TABLE OF CONTENTS

LIST OF FIGURES

LIST OF TABLES

LIST OF ABBREVIATIONS

a	radius
α	absorption coefficient
~	approximately
≈	approximately equal to
CCD	charge-coupled device
COM	calcium oxalate monohydrate
°C	degrees Celsius
Δ	change
dia	diameter
DOF	depth of field
ex vivo	Latin: (out of the living)
FC	fiber connector
FLIR	forward-looking infrared
FOV	field of view
fps	frames per second
Fr	French (1 mm = 3 Fr)
FWHM	full width-half maximum
g	gram
GRIN	graded-index
Ho	Holmium
in vitro	Latin: (within glass)
in vivo	Latin: (within the living)

ID	inner diameter
IR	infrared
J	joule
λ	wavelength
μ-	micro- (10^{-6})
m	meter
m-	milli- (10^{-3})
min	minute
N	number
n	index of refraction
n-	nano- (10^{-9})
NA	numerical aperture
OD	outer diameter
OPD	optical penetration depth
s *or* sec	second
SD	standard deviation
θ_i	incident angle
θ_r	refracted angle
3D	three dimensional
TFL	Thulium fiber laser
UV	ultraviolet
W	watt
YAG	yttrium aluminum garnet

CHAPTER 1: INTRODUCTION

Kidney Stone Disease

Kidney stone disease is a common and costly disorder, affecting ~10% of the U.S. Population [1]. Annual costs to the national health care system are estimated to be $5.3 billion. Each year, over 3 million patient visits to health care providers occur with over 500,000 treatments in emergency rooms for kidney stones [2]. Furthermore, over the last two decades, a marked increase in stone disease has been associated with changing demographics, diet, and lifestyle of our population [3]. On the basis of demographic and lifestyle modeling, continued and further increasing rates of stone disease are expected to occur in the coming decades [4].

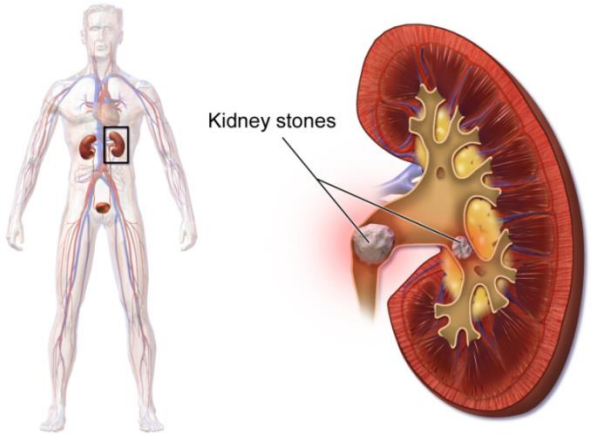

(a) (b)

Figure 1.1: (a) Diagram of the human body illuminating the kidney. (b) Enlarged diagram of the kidney with kidney stones in ureter and major calyces.

As depicted in Figure 1.1, urinary stones may stay in the kidney or travel down the urinary tract and become lodged, reducing urinary flow, and causing severe discomfort and pain [5]. Some stones eventually pass, or flush out of the urinary tract, but larger or oddly shaped stones may remain within the body, requiring immediate medical relief.

Holmium Laser

The solid-state, flashlamp-pumped, Holmium:YAG laser (Ho:YAG) has become the principal laser lithotripter in clinical use over the past 15 years. The laser is typically operated with a wavelength of 2120 nm, pulse energies of 0.5-2.0 J, a 350-700 μs pulse length, pulse rates of 5-20 Hz, and average powers of < 10 W. Low-OH, multimode silica optical fibers with core diameters of 270-1000 μm are commonly used during Ho:YAG laser lithotripsy procedures. The larger fibers (550-1000 μm) are inserted through the working channel of a rigid endoscope for use in the lower urinary tract to fragment large bladder stones. The smaller, more flexible optical fibers (270-365 μm) are used in flexible endoscopes, sometimes under extreme bending conditions, in the upper urinary tract (e.g. in the kidney).

In general, several problems are associated with using optical fibers inside flexible endoscopes. Tight bending diameters (< 1 cm) are necessary to reach stones in the lower pole of the kidney. While the endoscopes satisfy such extreme bending conditions, when a fiber is present in the endoscope working channel, it may hinder endoscope deflection, or even break, resulting in perforation of the endoscope during laser activation [6,7].

Although use of smaller, more flexible fibers would reduce fiber failure, the Ho:YAG laser multimode beam prohibits coupling of high laser powers into small-core fibers, without risking overfilling of the input fiber core, launching into the cladding, and

consequent fiber damage. Ho:YAG lasers typically have beam diameters of 275-500 μm [8], however the smallest Ho:YAG fiber that is used in maximally flexed situations, such as the lower pole calyx, is 200 μm. Fibers larger than this diameter may interfere with flexion of the endoscope.

Several approaches have been used to reduce fiber input end failure during coupling of a high-power Ho:YAG laser beam into connectorized small-core fibers [8,9]. These approaches include: (a) ferrule designs which absorb or direct excess energy away from the fiber cladding, but result in loss of laser power and inefficient fiber coupling, and (b) tapered fiber designs that produce higher order modes which can escape into the fiber cladding creating an even poorer spatial beam profile at the fiber output end. Ho:YAG lasers also produce high amounts of heat, which changes the intensity distribution of the laser spatial beam profile, and potentially leads to misalignment of the laser beam with the fiber input end, thus increasing the probability of fiber damage [10].

During lithotripsy, saline irrigation is flushed through the same endoscope working channel as occupied by the fiber to resolve poor visibility created by stone dust. Frequent irrigation of the working area is therefore necessary; however, irrigation rates are lowered by the presence of larger fibers in the endoscope working channel [11].

Thulium Fiber Laser

Use of fiber lasers for lithotripsy may eliminate some of these limitations. A major advantage of fiber laser technology is the single-mode spatial beam profile as compared to the multimode beam of solid-state lasers. The improved fiber laser beam profile eliminates concerns that affect Ho:YAG laser lithotripsy, including overfilling of the input fiber, inefficient fiber coupling, and thermal lensing effects.

The experimental Thulium Fiber Laser (TFL) is currently being studied as a potential alternative to the Holmium:YAG laser (Ho:YAG) for the treatment of kidney stones. The TFL has several potential advantages compared to Ho:YAG laser for lithotripsy, which are summarized in Table 1.2. First, the TFL wavelength (λ = 1908 nm) more closely matches a high-temperature water absorption peak (λ ~ 1910 nm) in tissue than Ho:YAG wavelength (λ = 2120 nm) [12-14] (Figure 1.2). Water is the primary absorber of laser radiation in tissues in the near- to mid-IR spectrum. The TFL water absorption coefficient at 1908 nm measures ~15 mm^{-1}, resulting in a penetration depth of ~ 70 μm, ~ 4 times lower than for the Ho:YAG laser [15]. This difference in turn translates into a factor of 4 times lower TFL stone ablation threshold [16].

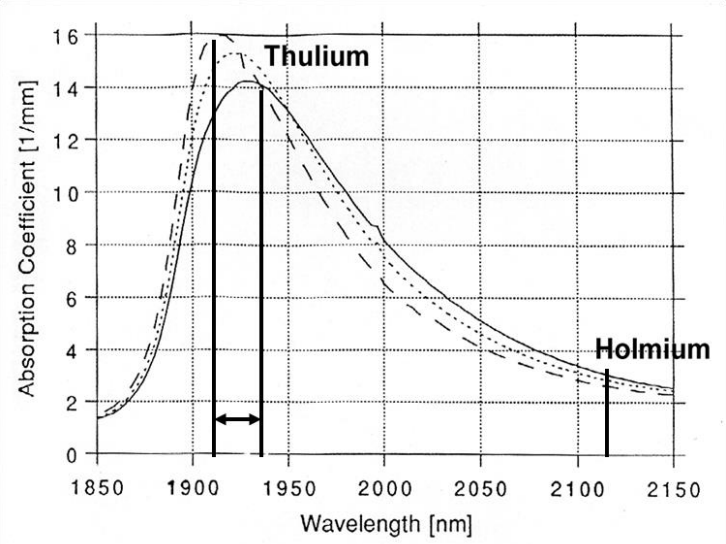

Figure 1.2: The TFL room temperature water absorption peak at 1940 nm shifts to about 1910 nm at ablation temperatures. The major emission lines of the TFL at 1908 and 1940 nm match this shifting peak more closely than the Ho:YAG laser (2120 nm) [13].

Second, the TFL spatial beam profile allows higher power coupling into smaller optical fibers (e.g. 50 and 100-µm-core) than those currently being used for Ho:YAG (>200-µm-core) lithotripsy [17-19] (Figure 1.3). For intricate lithotripsy procedures requiring extreme flexion of the endoscope (e.g. in lower pole of the kidney), a smaller fiber permits greater flexibility of the instrument. The smaller fiber also permits increased irrigation through the small (1.2-mm-ID) working channel within the instrument, resulting in improved visibility and, hence, safety [17-19]. This decrease in fiber diameter translates into a potential decrease in the size of ureteroscope working channel and may also extend to a decrease in overall ureteroscope diameter. Furthermore, the improved spatial beam profile reduces the risk of damaging the input end of the fiber as evidenced by the higher transmission rates and fiber damage thresholds reported in Table 1.1. Therefore, it may be possible to preserve the trunk fiber minus the distal fiber tip, between procedures, thus resulting in significant cost savings.

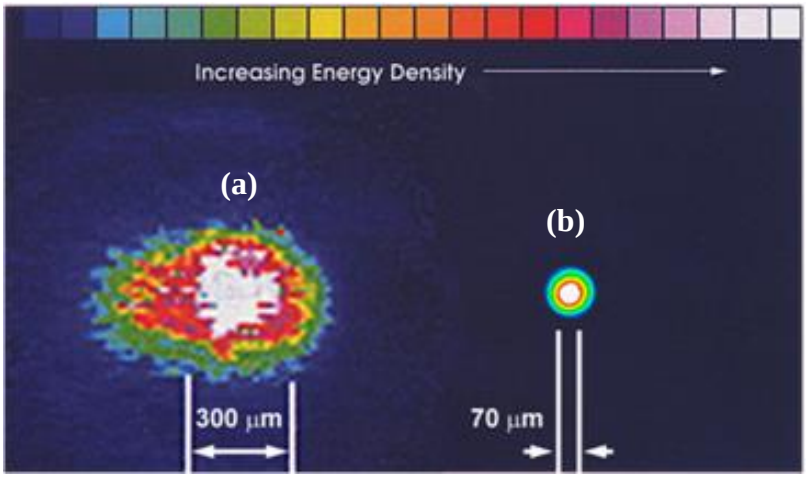

Figure 1.3: Spatial beam waist profiles for (a) Ho:YAG laser (300 µm) on the left, and (b) Thulium fiber laser (70 µm) on the right. Unlike the TFL beam, the multimode Ho:YAG laser beam typically overflows 150 and 200 µm core fibers [8].

Table 1.1: Thulium fiber laser's superior spatial beam profile allows transmission of higher laser power through smaller fibers than Holmium laser.

Fiber Damage Thresholds		
Fiber Core (µm)	Ho:YAG	Thulium Fiber
50	NA	15 W
100	NA	39 W
150	6 W	58 W
200	25 W	> 83 W
365	100 W	NA

Third, while the diode-pumped TFL is limited to low pulse energies, it is capable of operating efficiently at high pulse rates (up to 1000 Hz). On the contrary, although the flashlamp-pumped Ho:YAG laser is capable of operating at high pulse energies (0.5 - 2 J), efficient operation is limited to low pulse rates (< 30 Hz) during lithotripsy [20].

Table 1.2: Comparison of Holmium:YAG and Thulium fiber laser properties for lithotripsy.

Holmium:YAG Laser
Advantages
• Low capital cost due in part to flashlamp-pumped configuration • Operation at high pulse energies (up to 2 J)
Disadvantages
• Wavelength (λ=2120 nm) does not match water absorption peak • Multimode beam profile prohibits use of fibers < 200 μm, and limits access to hard-to-reach locations (lower pole of kidney) • Thermal lensing affects limit operation to pulse rates < 20 Hz • Low wall-plug efficiency (< 2%) requires 220-V electrical configuration and water cooling for high-power operation. • High maintenance costs
Thulium Fiber Laser
Advantages
• Wavelength (λ=1908 nm) matches high-temperature water absorption peak in tissue, providing 4x lower ablation threshold • Single-mode beam profile allows high-power transmission through smaller surgical fibers < 200 μm, which are more flexible and occupy less space in endoscope working channel • Variable laser pulse length • High pulse rates up to 1000 Hz for faster stone ablation • High wall-plug efficiency (~ 10%) may allow high-power operation with 110-V electrical configuration and air cooling • Low maintenance costs
Disadvantages
• Diode-pumped configuration increases capital cost of laser • Electronic modulation limits operation to low pulse energies

Current Research

This thesis details rapid TFL lithotripsy at high pulse rates up to 500 Hz, both with and without the aid of a ureteroscope, in order to demonstrate the TFL's superior ablation rates over the Ho:YAG. Temperature measurements and collateral damage testing of the TFL effect on the ureter wall and Nitinol stone baskets were conducted as safety studies in preparation for future clinical studies. Proximal fiber end damage testing was conducted to demonstrate fiber preservation, critical for permanent fiber integration into endoscopes. Optical fibers were also fitted with fabricated hollow steel tips and integrated with stone retrieval baskets for testing. Ball tip fibers were investigated for comparable ablation rates and atraumatic ureteroscope insertion.

Illumination sources and configurations were designed and tested. Ureteroscope designs were be devised, modeled, fabricated, and tested, implementing reduction of working channel and optimization of illumination, culminating in a novel miniaturized ureteroscope for use in TFL lithotripsy. This final device, coupled with the proven TFL and optimized laser parameters may further establish the TFL as a viable replacement for the conventional Ho:YAG laser for treatment of kidney stones.

High Pulse Rates (Chapter 2)

The experimental Thulium fiber laser was studied as an alternative laser to the standard, clinical Holmium:YAG laser for ablation of kidney stones. TFL operation at pulse rates up to 500 Hz resulted in rapid fragmentation of human uric acid and calcium oxalate monohydrate urinary stones at ablation rates that may be practical for future translation into the clinic.

Collateral Damage Studies (Chapter 3)

Previous experimental and clinical studies have reported perforation of the ureter during Holmium laser lithotripsy [21-23]. Recently, we have also conducted Holmium and TFL lithotripsy in an artificial *in vitro* ureter model, where stone ablation rates and saline temperature readings were compared [24]. The objective of this study was to provide safety data concerning use of the Thulium fiber laser during lithotripsy by characterizing the potential for TFL-induced damage to the porcine ureter wall and to typical instrumentation such as Nitinol stone baskets.

Proximal Fiber Damage (Chapter 4)

To later exercise fiber integration into endoscopes, we demonstrated the ability of the TFL to operate at pulse rates corresponding to clinically significant ablation rates for extended amounts of time while maintaining a pristine and undamaged proximal-end polish consistent with maintaining consistent average output power. We have verified that the proximal end of a 100-μm-core, low-OH silica fiber can sustain an excess of 3,000,000 pulses without degradation, or loss of percent transmission, affirming itself as a candidate for semi-permanent device integration.

A novel 1.9 Fr (0.63 mm) integrated steel-tipped fiber and stone basket device was designed and tested, enabling more efficient Thulium fiber laser ablation of urinary stones with minimal stone retropulsion and improved flexibility, enhanced saline irrigation rates, and decreased fiber burnback, compared to conventional non-integrated fiber and stone baskets.

Illumination (Chapter 5)

Ring illumination has been adapted for use during surgery on a large scale, such as Thoracic procedures [25]. We scale down this technology to a smaller footprint, outfitting the viewing optic with a ring configured illumination bundle. This orientation's purpose is two-fold; first, to provide uniformity of light distribution for enhanced image quality, and second, to reduce the port footprint on the ureteroscope's distal tip. In this study we modified not only the illumination configuration, but also the lighting source itself. Previous studies have explored categories of light sources, even incorporating bandwidth manipulation. We evaluated reflectance spectroscopy results of a broadband-halogen lamp fiber illuminator and human calculi versus ureter tissue in order to determine optimal narrow band illumination. Luminous intensity curves were plotted in multiple axes and combined in a stacked modeling system for future design representations.

Ureteroscope Miniaturization (Chapter 6)

A miniaturized ureteroscope polyamide tubing prototype was designed and tested for use in Thulium fiber laser lithotripsy, towards the development of an office-based procedure. We explore flow rates through working channels of non-traditional diameters and cross-sections in an effort to optimize the working channel for the most advantageous ureteroscope design. Original designs incorporating a combined detection and illumination port as well as a non-radially symmetric working channel, created in a CAD program, were translated into FDM and SLA printed prototypes, further progressing toward a fully functional, test ready prototype. Stereolithography delivered a novel 6 Fr (2 mm), testable ureteroscope tip.

Miniature Ball-tip Fiber (Chapter 7)

A novel ratio 100-µm-core, 300-µm-diameter ball-tip fiber for TFL lithotripsy rapidly fragmented kidney stones at rates comparable to conventional 100-µm-core bare tip fibers at laser parameters of 35 mJ, 500 µs, 300 Hz. While the ball tip fibers did not demonstrate resistance to degradation, the spherical geometry does provide an additional safety feature for initial fiber insertion through the ureteroscope working channel at rates comparable to those of the 100-µm-core traditional fiber used in TFL lithotripsy.

PROJECT TREE

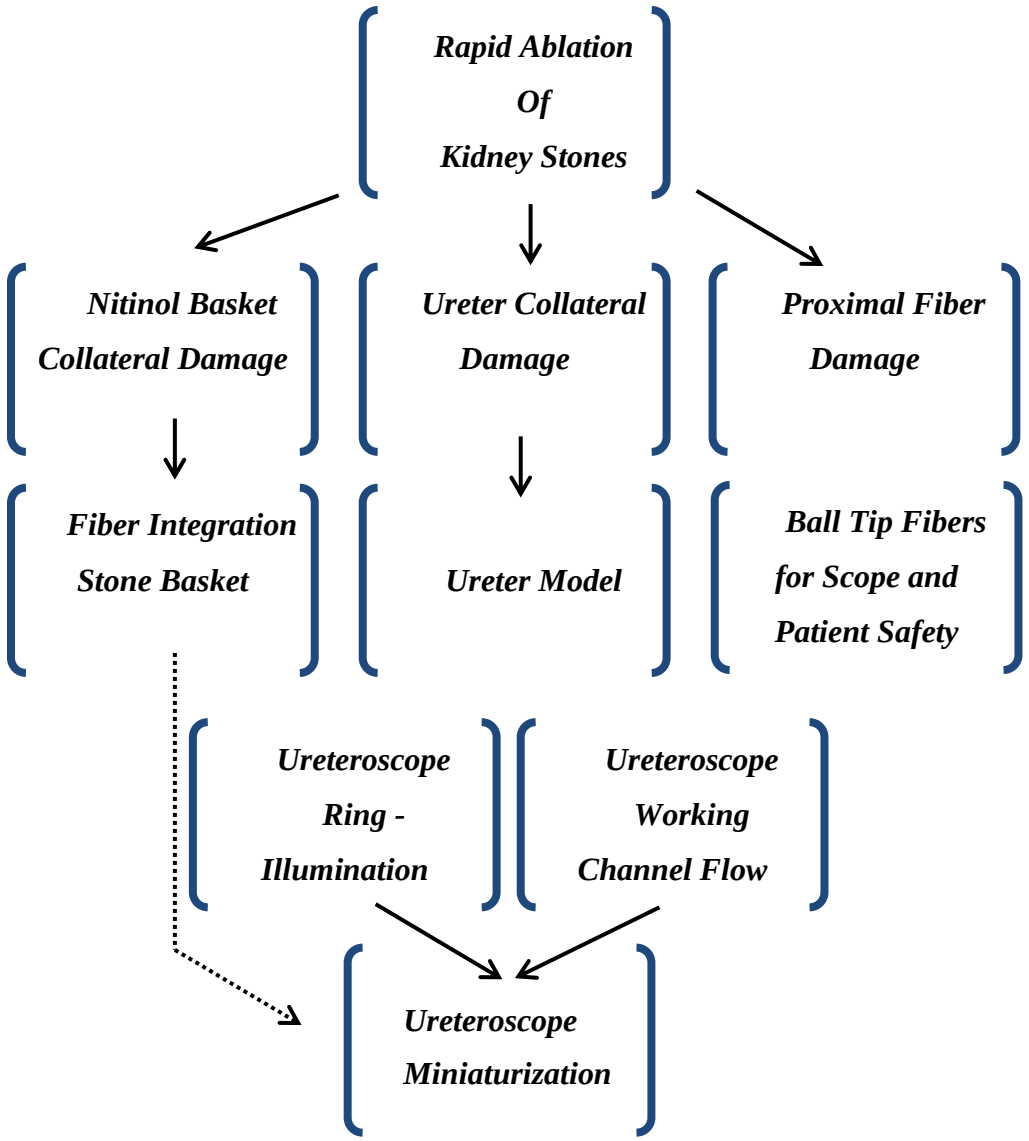

CHAPTER 2: RAPID THULIUM FIBER LASER LITHOTRIPSY AT HIGH PULSE RATES

2.1 Introduction

A significant percentage of kidney stone cases require surgical intervention. Holmium:YAG laser lithotripsy via advanced ureteroscopy has become a major technique for minimally invasive destruction of urinary stones. For small to moderate sized or multiple stones, this technology is the preferred surgical option over extracorporeal shock wave lithotripsy [26,27]. Maximal clinical efficiency of laser lithotripsy is important to decrease operative time, surgical risk, and costs. The rate of stone destruction, or ablation rate, is a significant measure of efficiency. Ho:YAG laser energy propels stones away from the fiber tip (resulting in retropulsion) unless the stone is fixed or impacted by surrounding tissues within the ureter or kidney. Stone retropulsion is a clinically significant phenomenon, as it causes the surgeon to "chase" the stone, resulting in a decrease in ablation efficiency, increase in surgical time and possible collateral tissue trauma [28-33]. Most stone clearance failures can be attributed to stone fragment retropulsion [29]. Therefore, elimination of retropulsion would be desirable. Several endoscopic devices (balloons, stone cones, accordions, baskets, and thermosensitive polymeric jell plugs) have been used to minimize stone retropulsion during lithotripsy [34].

During our previous studies, we have observed that stone phantom retropulsion became significant when operating the TFL at pulse rates > 150 Hz, without assistance of

a stone stabilization device [16]. The objective of this study is to use a clamp or stone basket to minimize stone retropulsion, and thus, allow TFL operation at pulse rates > 150 Hz for more efficient stone ablation.

2.2 Methods

2.2.1 Thulium Fiber Laser Parameters

A 100-Watt Thulium fiber laser (TLR 110-1908, IPG Photonics, Oxford, MA) (TFL) with a center wavelength of 1908 nm was used in these studies. This wavelength was chosen to closely match a high-temperature water absorption peak in tissue in the IR spectrum [12-14]. The continuous-wave TFL was modulated using a function generator (DS345, Stanford Research Systems, Sunnyvale, CA) to operate in long-pulse mode, producing 500-μs pulses for lithotripsy studies, similar to conventional Ho:YAG laser pulse lengths of 350-700 μs. The TFL produced a Gaussian, near single-mode spatial beam profile, originating from an 18-μm-core thulium-doped silica fiber, with a built-in collimator providing a 5.5-mm-diameter output beam. A 25-mm-FL CaFl lens was used to focus the TFL beam down to a $1/e^2$ spot diameter of ~ 75 μm, for coupling into a standard, disposable, low-OH, 100-μm-core silica optical fiber (AFS105/125, Thorlabs, Newton, NJ), for use in stone ablation studies. All experiments were performed with a TFL output pulse energy of 35 mJ, pulse duration of 500 μs, and pulse rates of 10-500 Hz.

2.2.2 Kidney Stone Samples

Human uric acid (UA) and calcium oxalate monohydrate (COM) stone samples with > 95% purity were obtained from several stone analysis laboratories including LabCorp (Oklahoma City, OK), Louis C. Herring & Co (Orlando, FL) and Carolinas Medical Center (Charlotte, NC). These stone samples were chosen because calcium oxalate and uric acid stones comprise ~ 80% and ~ 10%, respectively, of all stone compositions encountered in the clinic [35]. Stone samples were desiccated in an oven for 30 min. and then weighed with an analytical balance (Model AB54-S, Mettler-Toledo, Switzerland) both before and after lithotripsy experiments to determine their mass loss. All experiments were performed with the stone samples completely submerged in a saline bath.

2.2.3 Experimental Setup

Two different techniques were used for stabilizing the stone during laser lithotripsy. The first method was designed to be a simplified representation of an impacted stone, that is embedded in tissue and not free to move on its own. This technique involved mechanically clamping the stone to eliminate stone retropulsion and to determine ablation rates under those specific conditions (Figure 2.1). During this procedure, the laser fiber was kept in close contact with the stone and manually scanned over the stone surface.

The second method involved using a 1.9-Fr (0.6-mm-OD) stone basket (Zero Tip Nitinol Stone Retrieval basket, Boston Scientific, Natick, MA, USA) as a standard clinical approach for stabilization of a stone that would otherwise be free to migrate in the urinary tract. The experimental setup consisted of a rigid ureteroscope (9.5-Fr ID,

Karl Storz, Germany) attached to a light source (X7000, Stryker Endoscopy, San Jose, CA), CCD camera (1188HD, Stryker), and monitor. The laser fiber and stone basket were inserted through the same ureteroscope working channel, and then, placed in contact with the urinary stone sample, which was submerged in a saline bath (Figure 2.2). Illumination from the endoscope and a magnified image from the CCD camera, connected to a monitor, were used to observe the laser lithotripsy procedure. Although the fiber was constrained by the endoscope working channel, the stabilized stone was still free to rotate and translate slightly inside of the stone basket during the procedure.

For both procedures, stone vaporization rate (μg/s) was calculated by determining net mass loss of stones as a function of laser irradiation time. The procedure was only paused momentarily under circumstances in which stone dust or bubble formation impeded the field of view. All residual stone samples > 2 mm were collected in a sieve and included in the stone mass measurements, consistent with the clinical endpoint for successful stone fragmentation, since small stone fragments (< 2 mm) can be naturally passed through the urinary tract. A minimum of five samples were tested for each dataset and the mean + standard deviation recorded.

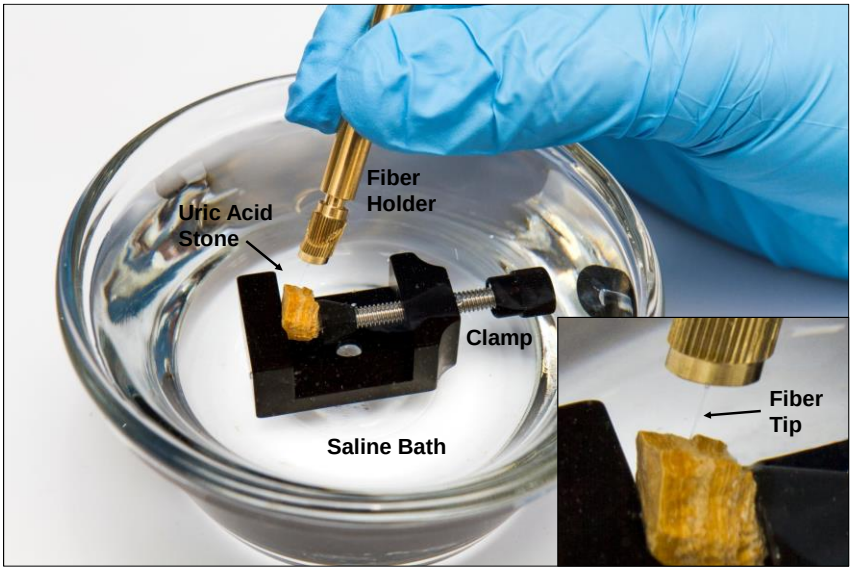

Figure 2.1: Experimental setup for TFL lithotripsy with a uric acid stone immobilized in a clamp and submerged in a saline bath.

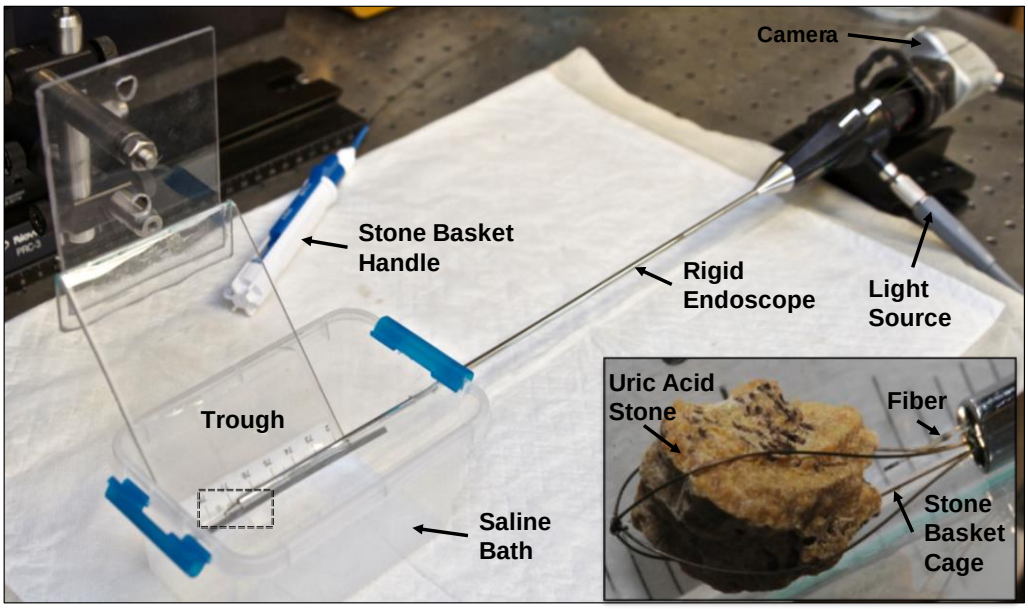

Figure 2.2: Experimental setup for TFL lithotripsy, showing rigid endoscope, optical fiber, and stone basket for grasping a uric acid stone immersed in a saline bath.

2.3 Results

Figure 2.3 shows TFL stone ablation rates as a function of both stone type and laser pulse rate. Pulse energy was fixed at 35 mJ, while pulse rate ranged from 10-500 Hz, translating into average powers of 0.35-17.50 W. TFL ablation of UA stones was 2-3 times faster than COM stones, due in part to differences in stone composition. However, both stone types exhibited a linear relationship between TFL pulse rate and stone ablation rate. The increase in TFL pulse rate compensated in part for low pulse energy output (35 mJ), resulting in higher stone ablation rates than observed in our previous studies [16].

Table 2.1 summarizes TFL stone ablation rates (at 500 Hz) as a function of stone type and stabilization device (clamp or basket). For the clamped stone, ablation and treatment rates were equivalent. Use of a clamp resulted in higher stone ablation rates because the stone was completely stabilized so that every laser pulse delivered to the stone contributed to stone ablation, and there was no restriction in freedom of movement. Use of the stone basket resulted in lower stone ablation rates due to limited freedom of movement of the fiber tip inside the rigid endoscope, and the need to frequently reposition the fiber during the procedure, resulting in some laser pulses being delivered into the saline bath rather than stone surface.

The large error bars for some data points in Figure 2.3 and Table 2.1 may be attributed to several factors, including variable stone mass density and surface texture, small variations in laser irradiation time, and human error during manually scanning of laser fiber across the stone surface.

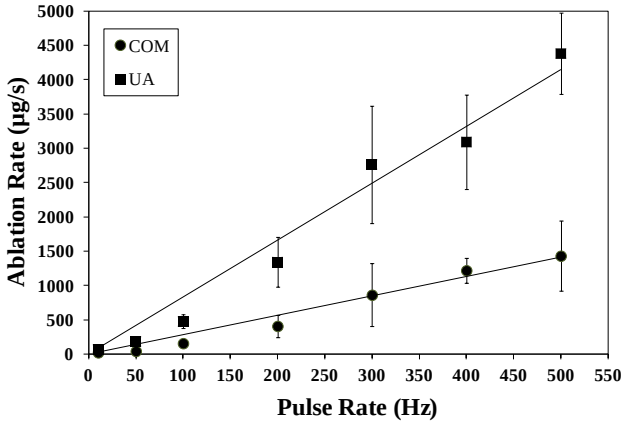

Figure 2.3: TFL stone ablation rate as a function of stone type and laser pulse repetition rate.

Table 2.1: TFL stone ablation rates as a function of stone type and stone stabilization device.

	Clamped Stone	Stone Basket	
	Ablation Rate (µg/s)	Ablation Rate (µg/s)	Treatment Rate (µg/s)
COM	1430 ± 513	703 ± 195	420 ± 134
UA	4377 ± 592	1727 ± 288	1063 ± 352

Figures 2.4 and 2.5 show representative photographs of human UA and COM stones both before and after TFL lithotripsy using a stone basket. The initial stone dimensions and mass provided are typical of stones encountered in the clinic. Laser irradiation time and total treatment time are also given. The UA stone was broken down into fragments < 2 mm diameter in an irradiation time of only 24 s and a total treatment time of only 65 s.

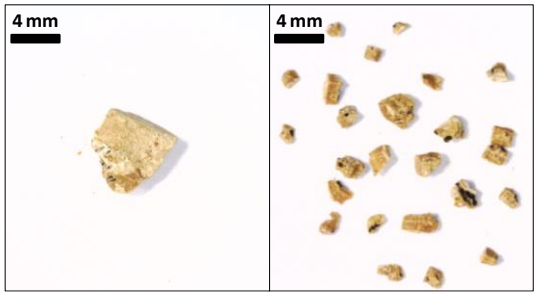

(a) (b)

Figure 2.4: Representative uric acid stone (a) before and (b) after TFL lithotripsy with 35 mJ, 500 µs, and 500 Hz. Total laser irradiation time was 24 s and total treatment time was 65 s. Initial stone size was 8 x 4 x 5 mm and initial stone mass was 135 mg.

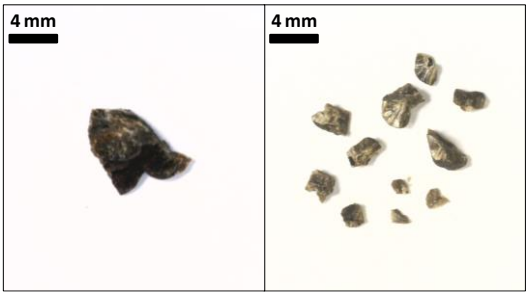

(a) (b)

Figure 2.5: Representative calcium oxalate monohydrate stone (a) before and (b) after TFL lithotripsy with 35 mJ, 500 µs, and 500 Hz. Total laser irradiation time was 83 s and total treatment time was 154 s. Initial stone size was 8 x 5 x 5 mm and initial stone mass was 162 mg.

2.4 Discussion

In previous reports, stone phantom retropulsion during TFL lithotripsy became significant at pulses rates > 150 Hz. However, limiting TFL operation to lower pulse rates unnecessarily limits stone ablation rates as well. It was also concluded, incorrectly, that TFL operation at higher pulse rates resulted in a plateau in the clamped stone ablation rates at ~ 100 Hz [16]. However, as observed in Figure 2.3 in this study, the stone ablation rate is directly proportional to the TFL pulse rate, and ablation rate continued to increase linearly in the entire range studied, from 10-500 Hz.

This study demonstrated that the TFL can be operated at ultra-high pulse rates up to 500 Hz, when used in combination with a commercially available clinical stone basket device. The stone basket served to stabilize the stones, minimizing retropulsion, and thus providing more efficient stone vaporization. It is estimated from these results that a typical stone size encountered in the clinic (5-8 mm diameter), could be treated in 1-2 min for UA stones and 3-5 min for COM stones, with the clinical endpoint being fragmentation into stone fragments $\leq$ 2 mm diameter, for subsequent natural passage through the urinary tract.

Direct comparisons between the clinical Ho:YAG laser lithotripter and the experimental TFL are difficult to perform since the two lasers have fundamentally different operation parameters. The Ho:YAG laser is typically operated at high pulse energy (0.5 - 2 J) and low pulse rates (5-20 Hz), while the TFL has been operated at low pulse energies (35 mJ) and high pulse rates (up to 500 Hz).

However, as both the long-pulse Holmium:YAG laser and the modulated Thulium fiber laser fragment stones based on a predominantly photothermal mechanism, as

opposed to short-pulse infrared lasers (e.g. q-switched) in which the mechanism is predominantly photomechanical, the two laser interactions are comparable to some degree. Despite some differences in laser parameters, it is informative to provide an estimate for comparison of ablation rates between the TFL and Ho:YAG lasers under the most similar conditions available. For example, from Table 2.1, the TFL ablation rate (at 500 Hz) for clamped COM stones measured 1430 ± 513 μg/s. Previous studies reported by our laboratory also measured Ho:YAG ablation rates for clamped COM stones. In these studies, the Ho:YAG pulse rate was fixed at 10 Hz, and Ho:YAG pulse energy was gradually increased. The Ho:YAG ablation rate measured 953 ± 160 μg/s and 1727 ± 485 μg/s at laser pulse energies of 700 mJ and 1000 mJ, respectively [36]. These values demonstrate that COM ablation rates for TFL and Ho:YAG lasers are comparable when the laser is operated with their normal lasers parameters and under similar conditions.

While stone ablation rates between the two lasers are comparable, it should be emphasized that the TFL offers a number of other significant advantages including use with smaller and more flexible fibers (< 270-μm-core) for improved access to hard-to-reach locations (e.g. lower pole of kidney) and higher irrigation rates through the endoscope for improved visibility and safety, more efficient operation, and lower maintenance costs.

2.5 Conclusions

The experimental TFL was studied as an alternative laser to the standard, clinical Holmium:YAG laser for ablation of kidney stones. TFL operation at pulse rates up to 500 Hz resulted in rapid fragmentation of human uric acid and calcium oxalate monohydrate urinary stones at ablation rates that may be practical for future translation into the clinic.

CHAPTER 3: COLLATERAL DAMAGE TO THE URETER AND NITINOL STONE BASKETS DURING THULIUM FIBER LASER LITHOTRIPSY

3.1 Introduction

Previous experimental and clinical studies have reported perforation of the ureter during Holmium laser lithotripsy [21-23]. Recently, we have also conducted Holmium and TFL lithotripsy in an artificial *in vitro* ureter model, where stone ablation rates and saline temperature readings were compared [24]. However, there is currently no safety data available concerning TFL parameters for ureter perforation.

Holmium laser operation (typically at high pulse energies and low pulse rates) also tends to propel stones away from the fiber optic tip, resulting in stone retropulsion, unless the stone is fixed or impacted by surrounding tissues within the ureter or kidney [28-33,37]. Stone retropulsion is a major concern because it causes the surgeon to pursue the stone, resulting in a decrease in ablation efficiency, increase in surgical operation time, and potential collateral tissue trauma as well. Furthermore, most stone clearance failures can be attributed to stone fragment retropulsion [29], so elimination of stone retropulsion is highly desirable. Numerous endoscopic devices have been used in the clinic to minimize stone retropulsion [34]. The stone basket is currently one of the most common devices used to retrieve stone fragments and minimize stone retropulsion during Holmium laser lithotripsy. However, accidental damage to the stone basket's Nitinol wires frequently occurs during endoscopic Holmium laser lithotripsy, leading to ureteral trauma [29,38]. Previous studies have been reported investigating Holmium laser

destruction of stone baskets during lithotripsy [38-42]. However, to date, no data exists concerning potential TFL damage to stone baskets.

The objective of this study is to provide safety data concerning use of the Thulium fiber laser during lithotripsy by characterizing the potential for TFL-induced damage to the porcine ureter wall and to typical instrumentation such as Nitinol stone baskets.

3.2 Methods

Thulium Fiber Laser Parameters

A 100-Watt, continuous-wave, Thulium fiber laser (TLR 110-1908, IPG Photonics, Oxford, MA) with a center wavelength of 1908 nm was used in these studies. A 25-mm-FL plano-convex lens (LA1560-C, Thorlabs, Newton, NJ) was used to focus the 5-mm-diameter collimated fiber laser beam down to a spot diameter of ~ 25 μm ($1/e^2$) for coupling into 100-μm-core, low-OH, silica optical fibers (AFS105/125, Thorlabs, Newton, NJ). The laser was electronically modulated with a function generator (DS345, Stanford Research Systems, Sunnyvale, CA) to produce a pulse energy of 35 mJ, pulse duration of 500 μs, and pulse rates of 50 - 500 Hz for all lithotripsy studies.

Ureter Perforation Studies

The distal tip of the TFL delivery fiber was placed in a fiber chuck, inserted into a fiber holder, and integrated into an x-y-z stage (460A-XYZ, Newport, Irvine, CA). An energy detector (ED-200, Gentec, Canada), connected to an oscilloscope (TDS1002B, Tektronix, Beaverton, OR), was placed behind the sample holder to detect tissue perforation (Figure 3.1). This general setup is consistent with previous experiments measuring laser perforation of the ureter, *in vitro* [43].

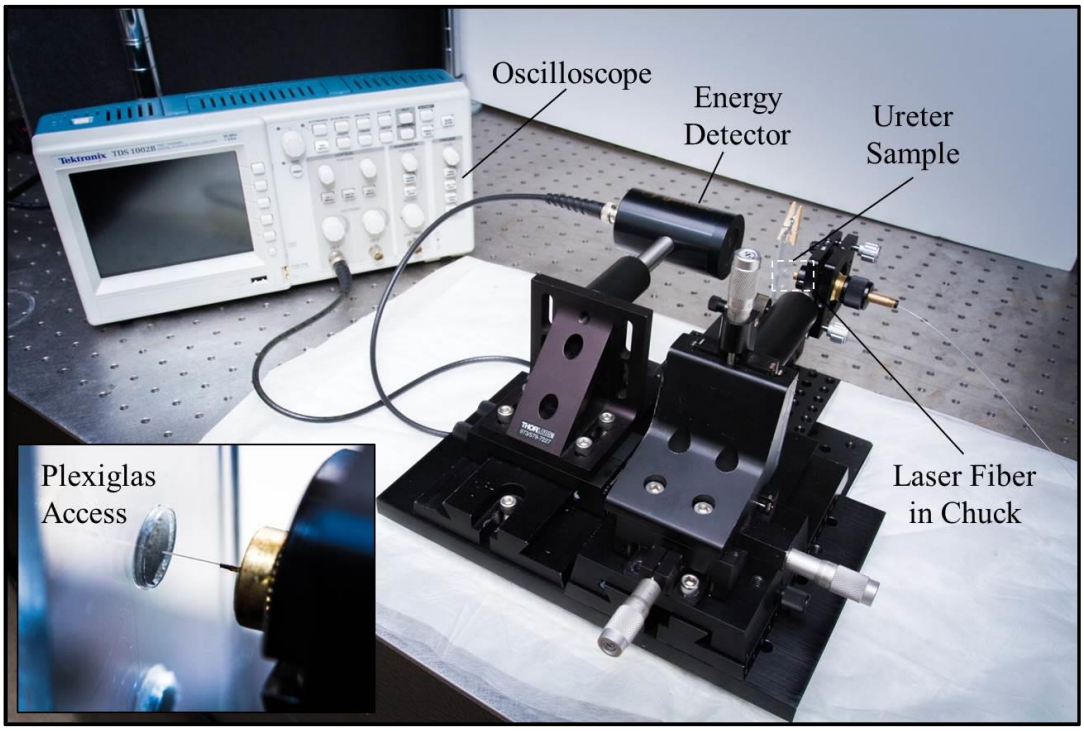

Figure 3.1: Experimental setup used for Thulium fiber laser perforation of porcine ureter, in vitro. Inset shows magnified view of fiber tip and Plexiglas port for tissue irradiation.

Fresh porcine ureters obtained from a slaughterhouse (Animal Technologies, Tyler, TX) were spatulated and then sectioned into 1 x 1 cm samples, with variable wall thickness ranging from 0.5 - 1.75 mm. Sample thickness between TFL data sets (150, 300, and 500 Hz), shown in Table 3.1, was not found to be significantly different ($P > 0.05$). The ureter tissue was kept hydrated in saline in preparation for the studies, and then individual ureter samples were gently compressed between a glass slide and Plexiglas, and held together by screwing a clamp below and tension pin above. Ureter sample thickness was measured using a gap feeler gauge. The sample was placed between laser fiber and power detector, perpendicular to and in contact with fiber tip. A syringe full of saline was used to hydrate tissue samples during studies.

The TFL was ramped up to full power output for the given laser parameters and held on standby via manipulation of the function generator. Laser irradiation was synchronized with oscilloscope's data acquisition time. Once the oscilloscope screen recorded and stored a spike in signal (energy), signifying perforation, the laser and acquisition window were stopped. The ureter sample was then removed and fixed in buffered formalin for further evaluation. This procedure was repeated with a sample size of n = 10 for each TFL data set (150, 300, and 500 Hz). The saved digital waveform was analyzed to determine number of laser pulses delivered before perforation. Each experiment produced an on screen waveform image as well as an Excel readout of the raw signal data in one millisecond increments.

Ureter samples were then imaged with a digital camera for comparison between TFL parameter sets. Samples were also imaged using an Optical Coherence Tomography (OCT) system (Niris, Imalux, Cleveland OH) to view cross sectional images and verify perforation. Finally, samples were sectioned and hematoxylin and eosin (H&E) stained for histology and evaluation of thermal damage dimensions.

Stone Basket Damage Studies

Stone baskets (Zero Tip Nitinol Stone Retrieval Basket, Boston Scientific, Natick, MA) with sheath outer diameter of 1.9 Fr (633 μm) were dismantled to salvage the individual Nitinol wires, which had a diameter of 110 μm. Sufficient material was salvaged to conduct multiple studies with the same parameters on a single wire, thus providing consistency and an accurate averaging of Nitinol damage grades.

Studies were conducted in a saline bath to simulate conditions similar to that of *in vivo* laser lithotripsy procedures. The 100 µm-core laser fiber was locked in a fiber optic chuck with the fiber's optical axis oriented perpendicular to the Nitinol wire via use of an x-y-z micro-positioning stage (460A-XYZ, Newport, Irvine, CA) placed directly above the clamped wire (Figure 3.2). A CCD camera (DCC1645C, Thorlabs, Newton, NJ) was used to view and record real-time video. After each individual experiment with matching parameters, the laser fiber was translated along the Nitinol wire in increments greater than 1 mm, to separate individual tests for accurate damage classification.

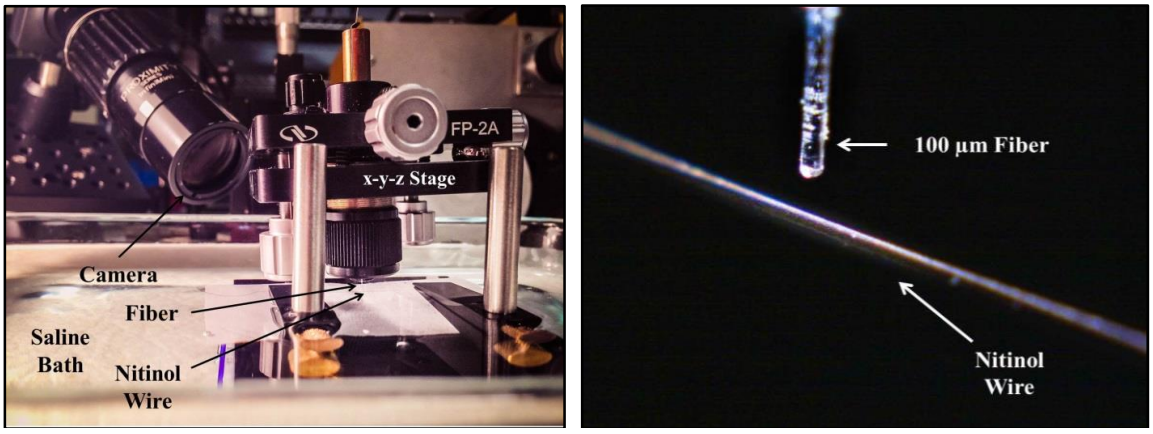

(a) (b)

Figure 3.2: (a) Experimental setup used for Thulium fiber laser induced damage to Nitinol basket wires; (b) Magnified view of fiber optic tip and Nitinol wire alignment.

TFL single pulse and pulse train studies were conducted with the laser fiber directly in contact with the Nitinol wire (n = 10). Damage for these studies was graded in a pass/fail manner, in which the fiber was either destroyed (cut) or remained intact. Testing progressed from single, double, and triple pulses, all the way up to 100 pulses delivered to the wire, one pulse at a time, via hand triggering the function generator.

Previous TFL lithotripsy studies have been reported using laser pulse rates up to 500 Hz [44]. Further studies were therefore conducted as a function of laser pulse rate and irradiation time, each yielding a total of about 500 pulses to directly compare pulse trains. The first study consisted of 50 Hz and 10 s duration, then 100 Hz for 5 s, and so forth, from 50 Hz to 500 Hz.

Finally, TFL pulse train studies were conducted as a function of working distance with the fiber oriented perpendicular to the Nitinol wire and separated by 0.1 mm increments with the working distance ranging from 0.0 - 1.1 mm. Care was taken to confirm that the laser was accurately aligned and that TFL energy which penetrated through the intervening saline layer in non-contact mode was delivered to the wire. Recorded video was reviewed to verify alignment. Damage was evaluated and scored on an individual basis and averaged for each study. Visual inspection and analysis was performed under magnification in still frames. Damage was graded as a function of pulse rate, number of pulses, and working distance. A 0-5 scale was used for evaluation, representing no damage (0%), discoloration, partial cuts (25, 50, 75%), and full cut (100%), respectively (Figure 3.3).

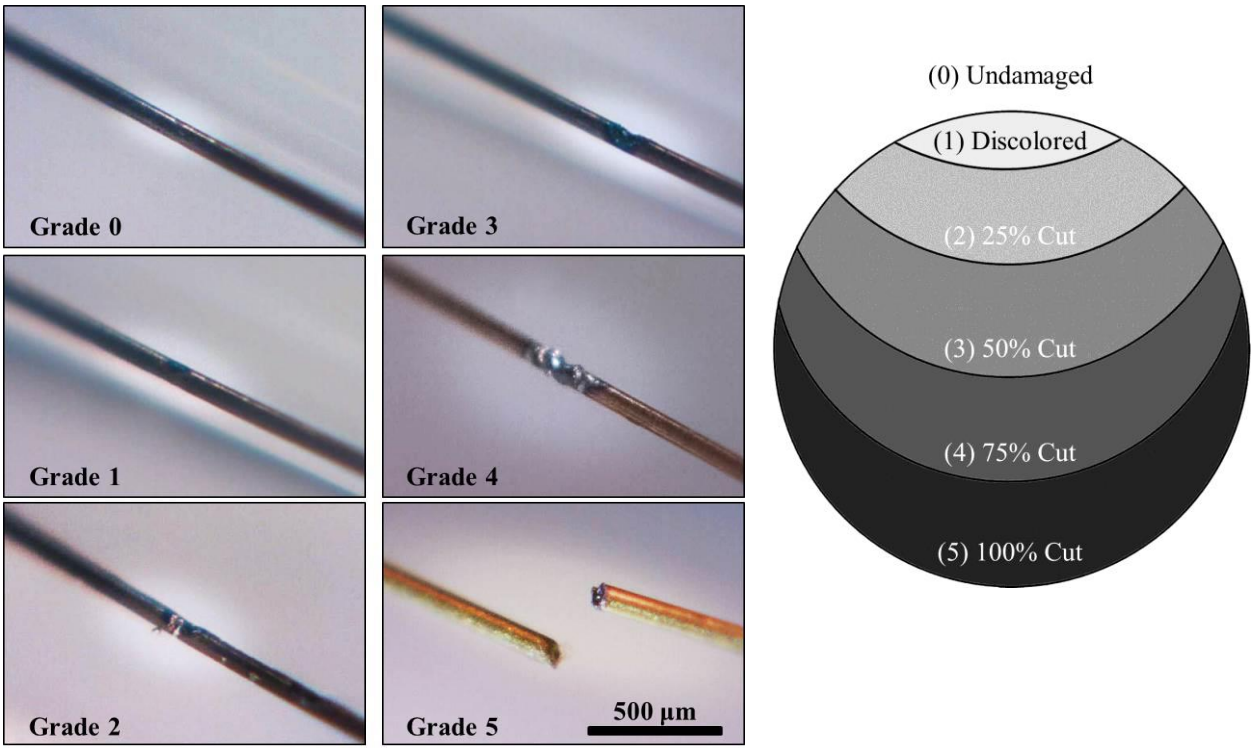

Figure 3.3: (a) Representative images showing damage grading scale (0-5) for Thulium fiber laser induced damage to Nitinol wire; (b) Diagram of Nitinol wire damage grading.

Statistical Analysis

A two-tailed student's t-test was conducted for the ureter perforation studies, including data sets on sample thickness, perforation times, ablation rates, and damage zone dimensions, as a function of TFL pulse duration. A value of $P<0.05$ was considered to be statistically significant.

3.3 Results

Ureter Perforation Studies

Recorded waveform images gave an approximate value for perforation time, and from the raw data, the exact time was determined with 1 ms accuracy. A representative waveform is provided in Figure 3.4. Mean ureter wall thickness, perforation time, and ablation rates were calculated. Mean perforation times decreased with an increase in TFL pulse rate, from 7.921 s at 150 Hz to 1.786 s at 500 Hz. Conversely, ureter ablation rates (μm/s and μm/pulse) increased with TFL pulse rate (Table 3.1).

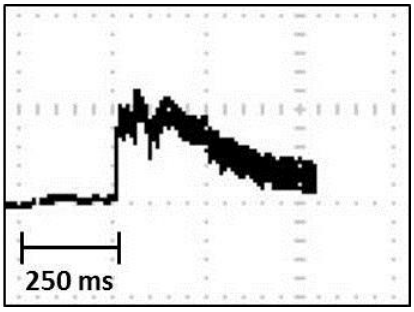

Figure 3.4: Waveform showing TFL perforation using 500 Hz pulse rate. The raw data stored in oscilloscope was used to determine exact perforation time with 1 ms accuracy.

Table 3.1: Ureter wall perforation results as a function of TFL pulse rate (n = 10 each).

Pulse Rate (Hz)	**Thickness** (mm)	**Perforation Time** (s)	**Ablation Rate** (μm/s)	**Ablation Rate** (μm/pulse)	**Damage Zone** (μm)
150	1.13 ± 0.36	7.921 ± 1.927	149 ± 56	0.99 ± 0.38	510 ± 140
300	1.28 ± 0.37	3.849 ± 1.049	337 ± 73	1.12 ± 0.24	370 ± 80
500	1.26 ± 0.34	1.786 ± 0.729	775 ± 237	1.55 ± 0.47	310 ± 70

Photographs of ureter samples indicated similar diameters for damage entrance craters (Figure 3.5a). Exit holes were smaller than their entrance counterpart and decreased in size with pulse rate (Figure 3.5b). Visible inspection revealed increased char at the rim of the ablation hole, consistent with previously observed increased charring of kidney stone ablation craters as pulse rate was increased. Further inspection

revealed a thermal coagulation zone around the perimeter of each ablation hole, which decreased with increasing pulse rate. Perforation was also verified with OCT and thermal damage dimensions were inspected via histology examination (Figure 3.5cd). The histology consistently showed two types of ureter damage along the periphery of the ablation crater. The first type was thermal damage indicated by the discoloration in the tissue from the H&E stain. The second type was mechanical damage indicated by the porous appearance of tissue. Both the larger than expected thermal damage width and presence of stress-induced tissue damage infer that TFL operation at high pulse rates produces a similar tissue effect to quasi-continuous-wave laser operation, with thermal buildup, and tissue expansion, and resultant tissue tearing.

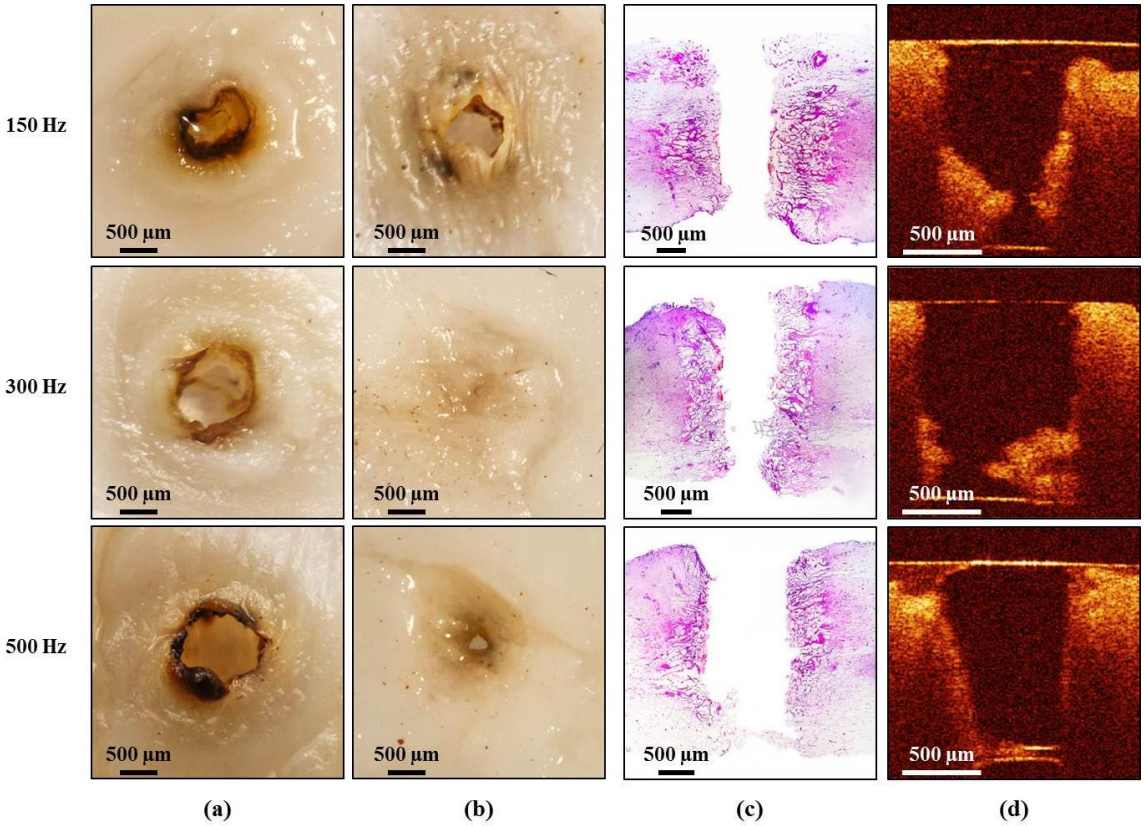

Figure 3.5: Representative images of the perforated ureter for TFL pulse rates of 150, 300, and 500 Hz. (a) Front surface; (b) Back surface; (c) H&E stained histology; (d) Optical coherence tomography. Note that for the OCT images, the horizontal lines in the images are artifacts produced by the back-reflections from the probe tip (top) and microscope glass slide (bottom) which the sample was placed on.

Stone Basket Damage Studies

A single TFL pulse delivered in contact mode with the Nitinol wire thermally altered but did not destroy the wire, as shown in Figure 3.6. Single, double, triple, and even 100 pulses delivered in succession and in contact mode were also insufficient to cut the wire. It was not until 500 pulses were delivered in rapid succession at a pulse rate of 200 Hz or greater, that a complete cut was observed, on the time scale of 2.5 s or less (Table 3.2). TFL perforation at 500 Hz demonstrated a strong dependence on working distance between the fiber tip and the Nitinol wire surface. Complete cutting of the wire occurred on every sample from contact mode up to a non-contact, working distance of 0.3 mm. At working distances greater than 1.0 mm, no visible damage was observed (Table 3.3).

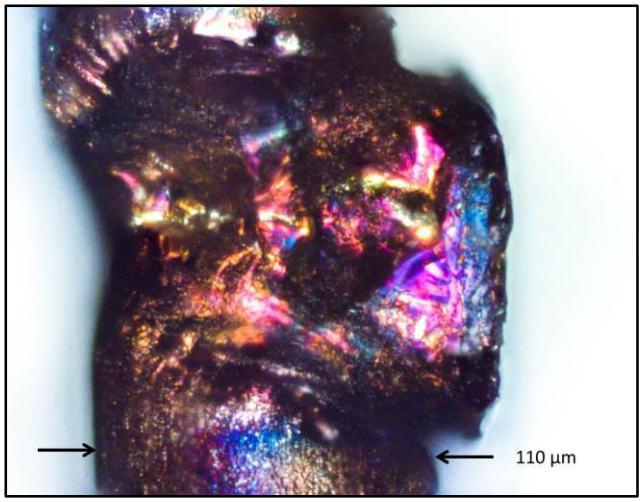

Figure 3.6: Nitinol wire damage by a single TFL pulse. Note that the wire becomes misshapen from the laser-induced thermal damage, but it is not destroyed.

Table 3.2: Nitinol wire perforation as a function of TFL parameters (n = 10 each).

Pulse train (500 Hz)	**Cut?**
50 Hz / 10 s	No
100 Hz / 5 s	No
200 Hz / 2.5 s	No
300 Hz / 1.5 s	Yes
500 Hz / 1 s	Yes

Table 3.3: Nitinol wire damage grade (0-5) as a function of working distance (WD) between fiber optic tip and wire during TFL ablation (n = 5 each).

WD (mm)	**0.0**	**0.1**	**0.2**	**0.3**	**0.4**	**0.5**	**0.6**	**0.7**	**0.8**	**0.9**	**1.0**	**1.1**
Grade	5.0	5.0	5.0	5.0	4.0	3.4	3.4	2.2	1.2	0.6	0.5	0.0
S.D.	0.0	0.0	0.0	0.0	1.0	1.5	1.5	1.9	1.3	0.9	0.6	0.0

3.4 Discussion

Ureter Perforation Studies

The TFL was operated at a pulse rate of 150, 300, and 500 Hz with pulse energies of 35 mJ, on average perforating the ureter wall in about 7.9, 3.8, and 1.8 s, respectively. For comparison, it should be noted that each result provides a greater safety margin than the Holmium laser, which perforated ureters in contact mode in less than 1 s at minimum laser settings of 1.0 W (0.2 J at 5 Hz) using a larger 365 μm fiber, as previously reported [21].

Review of H&E histology revealed the collateral damage at the edge of the ureter ablation crater to be inversely proportional to pulse rate. Mean damage widths of 510, 370, and 310 μm, corresponding to a pulse rate of 150, 300, and 500 Hz, were determined to be significantly different ($P < 0.05$). This was expected as lower pulse rates require longer procedure times in order to perforate the ureter wall, and this corresponding increase in time correlates with a greater damage zone. Steam noted during the experiment, along with the porosity of the histological damage zones suggests a rapid thermal buildup and vaporization of the intracellular and interstitial water, subsequently causing a "popcorn effect" indicative of quasi-CW tissue ablation, as viewed in Figure 3.5c.

It should be emphasized that the experimental setup used in this study represented a worst case scenario in which the fiber optic tip was positioned perpendicular to the ureter wall. Such a configuration is not normally encountered in the clinic. Thus, these results represent the fastest ureter ablation rates and provide a conservative measurement for perforation time. As the fiber optic tip is moved further from the tissue surface, and/or

the fiber incident angle increases, ablation rate should decrease and perforation time increase. This interpretation is in part reinforced by results from the complementary study involving TFL ablation of Nitinol wires as a function of pulse rate and working distance, which yielded complete wire cuts at working distances ≤ 0.3 mm, but revealed no visible damage at working distances ≥ 1.1 mm after 500 pulses and 1 s of laser irradiation.

In the clinic, the laser fiber is more commonly oriented perpendicular to the kidney stone, but parallel to the ureter. For example, as previously noted, the Holmium laser operated at a minimum power setting of 1.0 W (0.2 J at 5 Hz) perforated the ureter wall in less than 1 s, when the fiber tip was placed in direct contact with the ureter. However, in a study of 598 patients spanning from 1993 - 1999, the Holmium laser only produced a single perforation [21,22]. Overall, the FDA has reported 41 adverse events associated with Holmium laser lithotripsy, including three deaths from ureteral perforation and retroperitoneal bleeding using the Holmium laser between 2003 and 2005 [23]. Although more definitive clinical data will ultimately need to be gathered, we speculate that it is possible that the TFL, with its shorter optical penetration depth and lower pulse energy, may result in even fewer accidental ureter perforations.

Another potential safety concern is collateral thermal damage to the ureter during TFL lithotripsy [45]. We have recently observed that TFL kidney stone ablation rates scale linearly with pulse rate, and when operated at pulse rates up to 500 Hz, that the TFL is capable of rapid stone ablation [44]. However, recent studies comparing Holmium and TFL lithotripsy in an *in vitro* ureter model produced peak saline temperatures of 48 ^{o}C when using the TFL at 500 Hz [24]. Saline temperatures may escalate even further and

therefore be of concern if laser irradiation is maintained for prolonged time periods, as it could potentially result in undesirable collateral thermal damage in the urinary tract.

As previously noted, TFL damage tests on ureters would ideally include angle of incidence and working distance dependence. However, in order to conduct these studies, ureters would need to be placed in saline and perforation confirmed without use of an energy detector. Such studies have been conducted in a submerged saline environment with Holmium laser irradiation of ureter outer wall and visible detection of methylene blue upon perforation [21]. However, while this alternative configuration provides ureter pressurization consistent with continuous-volume irrigation, laser energy is delivered to the wrong side of the ureter wall and visible detection of perforation time is less precise.

Stone Basket Damage Studies

TFL studies conducted with the fiber in contact with Nitinol wires demonstrated that a single 35 mJ pulse delivered from the TFL was sufficient to create an ablation crater, but insufficient to sever the entire wire as seen in Figure 3.7. Further pulses delivered manually without repositioning the fiber were also unsuccessful in cutting, even after delivery of up to 100 pulses. Complete cuts from pulse trains 300 Hz and above suggest that thermal superposition through superheating of the saline during ablation begins to play a more dominant role in Nitinol destruction, although this interpretation cannot be directly confirmed without saline temperature data. At a pulse rate of 500 Hz, comparable to previous studies, the wire was cut within 1 s of laser irradiation time, which led us to conduct non-contact fiber working distance studies at 500 Hz as well.

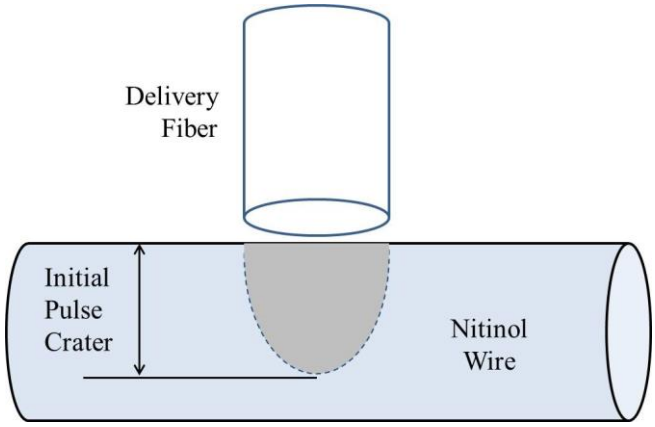

Figure 3.7: Diagram of Nitinol wire damage after a single pulse.

During preliminary studies, a single pulse Nitinol wire ablation threshold of 20 mJ per pulse, corresponding to a fluence of 231 J/cm^2 was observed. The laser fluence at a working distance of 0.1 mm from the fiber tip drops to 198 J/cm^2, below the single pulse Nitinol ablation threshold, and yet, at high pulse rates of 500 Hz, Table 3.3 shows consistent cutting of Nitinol wire at working distances up to 0.3 mm. This discrepancy further supports the interpretation that thermal superposition at high TFL pulse rates plays a dominant role in Nitinol wire ablation.

For both ureter and Nitinol studies, it should be noted that TFL wavelength (λ=1908 nm) closely matches a water absorption peak in tissue, where water is the primary absorber of laser radiation in near- to mid-IR spectrum [12–14]. This water absorption peak shifts from 1940 nm at room temperature (22°C) to 1920 nm at higher water temperatures (70°C) [13]. Water temperatures during tissue ablation are much higher, but no data is currently available at such temperatures. With water heating, the TFL absorption coefficient shifts from about 125 to about 155 cm^{-1}, translating into an optical penetration depth (OPD) shift from 80 to 65 µm. Thus, dissipation of energy and less

damage at working distances greater than this depth are expected. For comparison, Holmium:YAG laser wavelength (λ = 2120 nm) corresponds to a high-temperature water absorption coefficient of ~30 cm^{-1} and an OPD of ~330μm [13].

Nevertheless, TFL-induced wire damage is observed at working distances up to 1.0 mm from fiber tip. This is most likely due to formation of a cavitation (vapor) bubble, which creates a channel for transmission of laser irradiation from the fiber tip to Nitinol wire with minimal saline absorption. This phenomenon resulting in a "parting of the water" is commonly referred to as the Moses effect. Although a fast camera for high speed photography of cavitation bubble dynamics was not available during this study to verify this hypothesis, indirect evidence of TFL cavitation bubble effects has been previously reported [46] and such cavitation bubble effects have also been well studied during pulsed Holmium:YAG laser irradiation in a fluid medium [32,47]. Holmium:YAG laser induced cavitation bubble characteristics during lithotripsy are highly dependent on both the laser parameters and fiber diameter, and bubble dimensions up to 5mm diameter and bubble lifetimes of about 500 ms have been recorded [32,47].

It is also possible to estimate the threshold fluence for bubble formation for the TFL, based on previously measured fluence values for the Holmium:YAG and Thulium:YAG laser wavelengths, and their respective water absorption coefficients. For example, the threshold fluence for bubble formation for Holmium:YAG laser (λ = 2120 nm) was reported to be 40 ± 10 J/cm^2 [48]. The threshold fluence for bubble formation for Thulium: YAG laser (λ = 2010 nm) was reported to be 20.7 ± 2.3 J/cm^2 [49]. Since the high-temperature water absorption coefficient for Thulium:YAG (μ_a = 60 cm^{-1}), is about twice that of Holmium:YAG (μ_a = 30 cm^{-1}) and the absorption coefficient for TFL (μ_a =

155cm^{-1}) is about five times that of the Holmium:YAG, the threshold fluence for bubble formation for TFL wavelength should be about five times less than Holmium:YAG. So, for TFL, the threshold fluence for cavitation bubble formation is estimated to be about 8 J/cm^2. In this study, an energy of 35 mJ/pulse delivered through a 105-µm-core fiber yielded a fluence of 404 J/cm^2, well beyond the estimated threshold (8 J/cm^2) for creating a cavitation bubble at the fiber tip.

The TFL induced cavitation bubble may allow for deeper penetration in the saline environment, but only for a relatively short distance, after which saline absorption again dominates and TFL transmitted energy decreases, thereby decreasing Nitinol wire damage. At distances >1.0 mm, no visible TFL induced thermal damage to the wire was observed. This working distance is about five times smaller than that of Holmium:YAG laser [40], strongly correlating with the approximately five times greater OPD in water for Holmium:YAG laser wavelength compared with TFL [12].

It is also important to consider that the divergent TFL beam exiting the fiber tip will result in a decrease in fluence and irradiance with working distance. Based on TFL (35 mJ/pulse, 500 Hz) and fiber parameters (105-µm-core, 0.22 numerical aperture), the fluence and irradiance can be calculated. Average TFL irradiance ranged from 202 kW/cm^2 in contact with the Nitinol wire to only 6 kW/cm^2 at a 1.1 mm working distance, taking into consideration both fiber NA and beam divergence deviation introduced by cavitation bubble boundary. Fluence ranged from 404 J/cm^2 at fiber tip to 13 J/cm^2 at 1.1 mm. Once the laser radiation crosses into saline, water absorption dominates, resulting in a dissipation of energy about 65 µm beyond the cavitation bubble. The decrease in

irradiance and fluence with working distance, combined with the shallow OPD support the findings that no visible damage was observed at distances greater than 1.0 mm.

Future studies are planned to directly observe the exact cavitation bubble dynamics for the TFL wavelength (λ = 1908 nm) during lithotripsy, as a function of laser pulse energy, pulse duration, and fiber diameter. Previous studies have reported on cavitation bubble dynamics for multiple IR laser wavelengths, including Holmium:YAG (λ = 2120 nm), Thulium:YAG (λ = 2010 nm), and Erbium:YAG (λ = 2940 nm) [50]. It is anticipated that the TFL wavelength, which corresponds to an intermediate OPD in water between that of Thulium:YAG and Erbium:YAG, would also produce bubble characteristics between those two lasers.

3.5 Conclusion

The Thulium fiber laser perforated the ureter wall, with fiber tip in contact mode, in about 8, 4, and 2 s for TFL pulse rates of 150, 300, and 500 Hz, respectively. Nitinol basket wire damage decreased with working distance and was non-existent at distances greater than 1.0 mm. In contact mode, a total of 500 pulses delivered at pulse rates $\geq$ 200 Hz (and times $\leq$ 2.5 s) was sufficient to cut basket wires. Overall, the TFL, operated in low pulse energy and high pulse rate mode, provides a greater safety margin than the clinical gold standard Holmium:YAG laser for lithotripsy. This is apparent from longer TFL ureter perforation times and shorter non-contact working distances for stone basket damage than previously reported with the Holmium laser.

CHAPTER 4: FIBER OPTIC INTEGRATION WITH THULIUM FIBER LASER LITHOTRIPSY DEVICES

4.1 Proximal Fiber Damage Study

4.1.1 Introduction

Holmium laser lithotripsy fibers have been known to fail during procedures due to proximal fiber tip failure. Holmium laser ablation rates have been reported to diminish after delivery of only 50 pulses (or 5 to 10 s at normal pulse rates) due to fiber damage, with laser power stabilizing at a diminished level, with roughly 30% lower transmission [51]. If excessive laser energy is reflected at the proximal connector end, it may also lead to decreased distal fiber tip output and decreased lithotripsy efficiency in a best case scenario, and proximal fiber destruction and laser damage in a worst case scenario [52]. Small (< 300-µm-core) fibers have high rates of connector end failures, including 2% using standard 272-µm-core fibers and 13% failure for 200-µm-core fibers [23].

Typically, single use fibers cost approximately $250 and represent a significant cost to the procedure, motivating development of a more robust, re-usable optical fiber. While multi-use Holmium fibers are also available, and are reported to reduce procedural costs by about $100 per procedure [53], these fibers still experience cumulative laser-induced damage with repeated use.

Fiber optic companies have attempted numerous approaches to reducing fiber failure on the fiber input (proximal) end during coupling of Holmium laser power into small-core fibers [8,9]. Such approaches include ferrule designs which absorb or direct excess

energy away from the fiber cladding. However, these designs result in wasteful losses of laser power and inefficient fiber coupling, in turn resulting in the need for a higher power and more expensive laser.

Our laboratory is currently investigating the experimental Thulium fiber laser (TFL) as a potential alternative to the clinical gold standard Holmium:YAG (Holmium) laser for lithotripsy. We hypothesize that the improved, near single mode TFL spatial beam profile should reduce the amount of laser-induced damage to the proximal fiber tip surface compared to the Holmium multimodal beam profile. If proximal fiber tip damage can be reduced or even eliminated during TFL lithotripsy, and the distal fiber tip can also be either preserved or easily replaced using one of the previously reported approaches, including hollow steel tips [54], tapered fiber tips [18], or detachable fiber tips [55], then the ultimate goal of providing a durable, long lasting optical fiber may be achieved.

4.1.2 Methods

4.1.2.1 Thulium Fiber Laser Parameters

A 100-Watt, continuous-wave, Thulium fiber laser (TLR 110-1908, IPG Photonics, Oxford, MA) with a center wavelength of 1908 nm was used in these studies. A 25-mm-focal-length, anti-reflection coated, plano-convex lens (LA1560-D, Thorlabs, Newton, NJ) was used to focus the 5.5-mm-diameter collimated fiber laser beam down to a spot diameter of 25 μm ($1/e^2$) for coupling into 105-μm-core, low-OH, silica optical fibers (AFS105/125, Thorlabs, Newton, NJ). The laser was electronically modulated with a function generator (DS345, Stanford Research Systems, Sunnyvale, CA) to produce a pulse energy of 35 mJ, pulse duration of 500 μs, and variable pulse rates of 50 - 500 Hz, chosen based on the results of previous studies [44,24].

4.1.2.2 Experimental Design

The optical fiber buffer was removed using a fiber stripper (Micro-Electronics, Seekonk, MA) to expose 5 mm of the fiber core and cladding, and the fiber tip was cleaved using a ruby tipped scribe (S90R, Thorlabs, Newton, NJ). Both proximal and distal ends of the fiber were polished using 0.3 μm grit, aluminum oxide polishing pads and a fiber optic polisher (Fibrmet, Buehler, Lake Bluff, IL). Fiber tips were inspected under magnification using a handheld fiber optic microscope (FS200, Thorlabs, Newton, NJ) to confirm a uniform fiber tip surface.

The proximal end of the TFL fiber was placed in a fiber chuck prior to polishing to reduce potential contaminants in contact with the fiber surface during handling. The fiber chuck was then integrated into a holder and precision x-y-z stage (460A-XYZ, Newport, Irvine, CA) for alignment with the incident TFL beam. The distal fiber tip was aligned

with a detector (PM150, Coherent, Santa Clara, CA) connected to a meter (EPM2000, Molectron, Portland, OR).

Inspection of the proximal fiber surface before and after each study utilized a tilted mirror and a CCD camera (DCC1645C, Thorlabs, Newton, NJ) to view and record images. The mirror was adjusted in and out of position with an articulating arm, mounted with the camera to an optical breadboard. The TFL was electronically modulated to deliver 500,000 pulses at each pulse rate (50, 100, 200, 300, 400, and 500 Hz). Mean fiber output power readings were recorded every 10,000 pulses. Mean energy per pulse and power output were then calculated and plotted.

4.1.2.3 Holmium Laser Parameters

Proximal fiber condition after Holmium laser lithotripsy procedures was studied for comparison with TFL fibers. Twenty fibers were collected after clinical ureteroscopic procedures performed using a Holmium laser (Medilas H20, Dornier Medtech, Wessling, Germany) with a wavelength of 2100 nm. Holmium laser parameter settings (total energy, number of pulses, and time) were recorded, and mean pulse energies were calculated (Table 4.1).

4.1.2.4 Fiber Inspection Techniques

A 0-3 scale was used for fiber damage evaluation, representing pristine surface (0), minor blemishes (1), craters (2), and complete destruction (3), respectively (Table 4.1). Each fiber was imaged using a laser confocal microscope (LEXT OLS4000, Olympus, Tokyo, Japan) at 5x, 10x, 20x, and 50x magnification. The confocal microscope constructed three dimensional (3D) representations via stitching of up to 500 images

obtained with a 405 nm diode laser, to create a high-resolution, wide-field image, allowing for 3D display and measurements. This feature was an essential tool as the high numerical aperture (NA) yields a shallow depth of field which would traditionally render global imaging impossible. This stitching capability further allowed for resolution beyond the diffraction limit, with the ability to resolve 0.12 µm XY line-width, and provide 0.8 nm scale Z-axis mechanical resolution. Line roughness measurement functions within the software allowed for precise measurements across the face of a fiber to quantify ablation crater size and depth observed in the traditional 2D images. However, there were limitations to confocal imaging. While on board algorithms limited aberrations to a degree, microscopic turbulence caused artifacts in the image, potentially adding error to measurements.

Table 4.1: Laser parameters and damage grade for single use fibers following clinical Holmium laser lithotripsy.

Fiber #	Total # Pulses	Total Energy (J)	Total Time (s)	Avg. Pulse Energy (mJ)	Damage Grade (0-3)
1	117	46	120	393	1
2	539	323	91	599	1
3	675	322	114	477	1
4	702	421	118	600	1
5	702	421	81	600	1
6	818	490	70	599	2
7	838	567	142	677	2
8	1391	836	154	601	2
9	1468	811	191	552	1
10	1544	926	828	600	2
11	2439	1463	410	600	2
12	2545	1527	426	600	1
13	3975	2385	337	600	1
14	4774	2140	627	448	3
15	4880	3904	496	800	1
16	6573	6215	552	946	1
17	6787	4072	698	600	1
18	7109	3281	562	462	1
19	9302	5923	802	637	2
20	10677	6387	723	598	2
Average	**3393**	**2123**	**377**	**599**	**1.5**
S.D.	**3200**	**2115**	**267**	**119**	**0.6**

4.1.2.5 Image Post Processing Techniques

A Sobel gradient filter was applied to each image for edge detection and used for locating ablation craters on the proximal fiber surface. The Sobel gradient filter essentially acted like a high-pass filter, attenuating the lower frequencies, and allowing the fine details to prevail. The resultant image was more clearly defined, as the soft details, or lower frequencies, were subtracted from the final figure. The higher spatial frequencies represented feature edges and were highlighted in the processed confocal images as white lines for optimal inspection. The final image clarified craters that were difficult to distinguish in a traditional image.

Histogram averaging, another form of post processing, was also utilized for inspection. This process averaged the most frequent intensity values over the image histogram and effectively increased global image contrast, more clearly defining features such as ablation craters and scratches, without sacrificing low frequency features from the original image.

4.1.3 Results

4.1.3.1 TFL Proximal Fiber Tip Studies

A fiber output energy of 35 mJ per pulse was maintained during delivery of 500,000 TFL pulses at each pulse rate setting (50, 100, 200, 300, 400, and 500 Hz). Mean fiber output power readings were taken every 10,000 pulses. For each pulse rate, pulse energy readings yielded an almost negligible standard deviation of ≤ 0.2 mJ from the selected pulse energy during the experiment (Figure 4.1a and 4.1b). TFL delivery through 105-μm-core fibers was observed without major fluctuation in fiber optic power output, and without any evidence of TFL induced damage to the proximal fiber end. Representative confocal images of the proximal fiber face after TFL experiments are shown in Figure 4.2 at 20x and 100x magnification. Scratches due to the polishing pads are only visible under high (100x) magnification and measure less than 0.2 μm in depth. What appears to be a small oil spot on the scale of 10-20 μm, possibly deposited during handling, is also present.

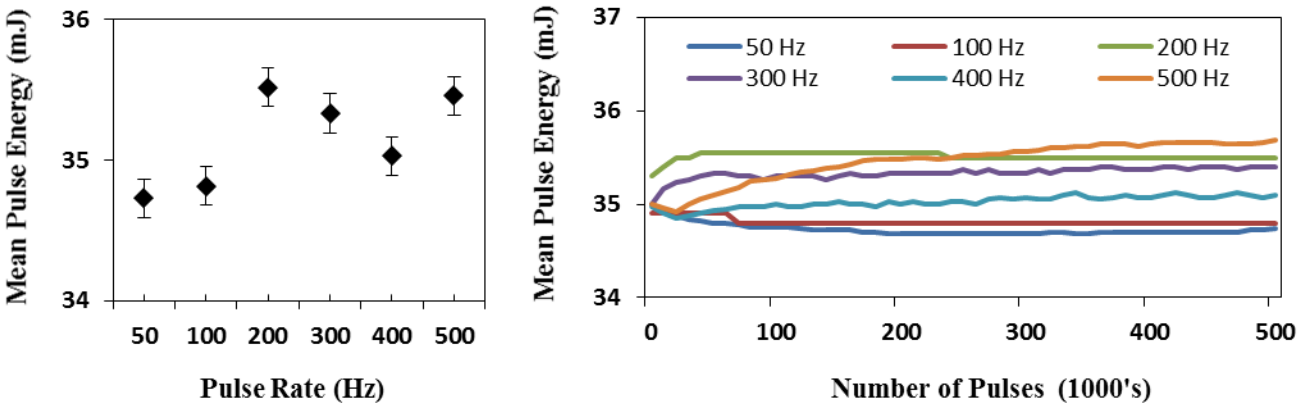

Figure 4.1: (a) Mean TFL pulse energy as function of pulse rate. (b) Mean TFL pulse energy over 500,000 pulses, demonstrating the pulse to pulse stability of the laser.

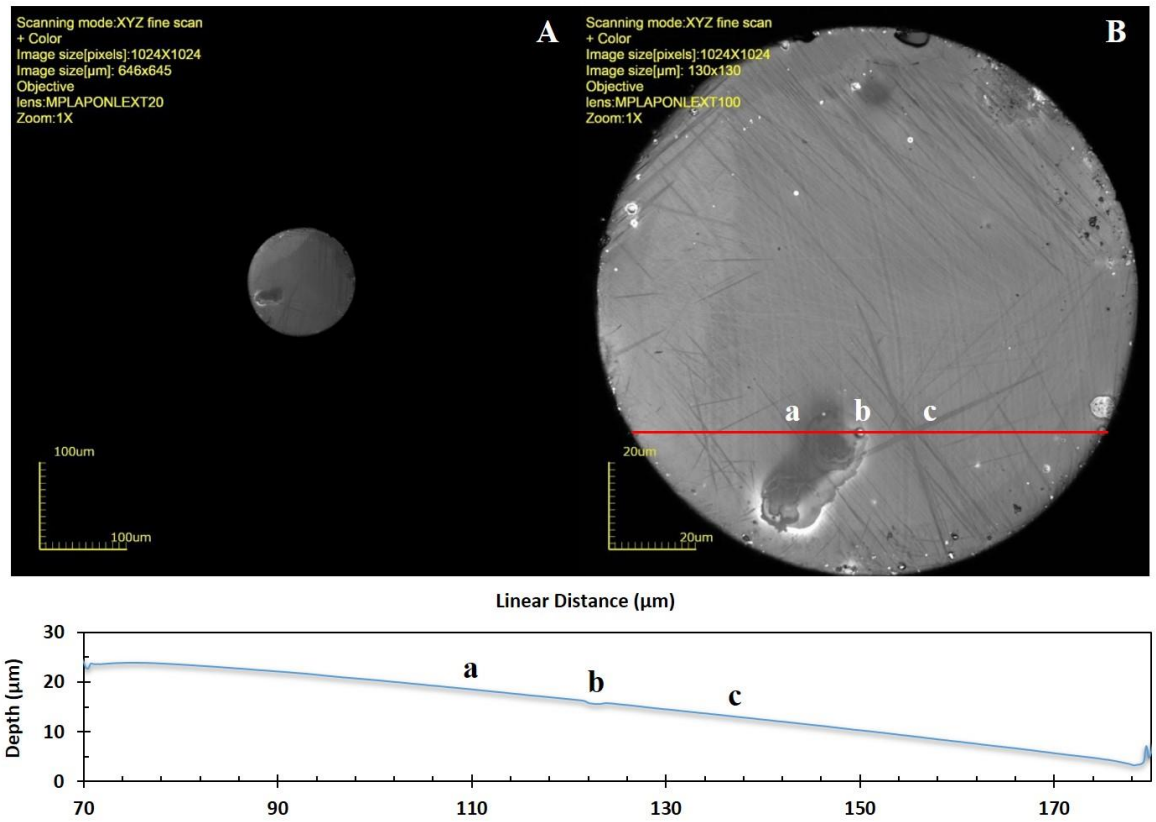

Figure 4.2**:** (A) Confocal (20x) image and (B) Confocal (100x) image of 105-µm-core proximal fiber tip after delivery of 3,000,000 TFL pulses; (C) The lone crater on the fiber surface (b) measures less than 0.2 µm in depth, while what appears to be an oil deposit (a) and scratches due to polishing (c) on the fiber surface do not register any significant damage to the fiber, as expected.

4.1.3.2 Holmium Proximal Fiber Tip Studies

As stated earlier, a 0-3 damage scale was used for evaluation, representing pristine surface (0), minor blemishes (1), craters (2), and complete destruction (3), respectively, of the proximal fiber tip (Table 4.1). The proximal surface of a pristine, control Holmium fiber is shown in Figure 4.3. The dark area visible from 2 to 4 o'clock is a void or defect where glue separated from the fiber and buffer. In general, during inspection of the 20 Holmium fibers, low damage (1) consisted of shallow craters measuring tenths of a micrometer, while higher amounts of damage (2) were observed in the form of larger craters measuring several micrometers in depth (Figure 4.4). A complete grid of

damaged proximal fiber tips is shown in Figure 4.5, with each fiber image labeled with its corresponding fiber number in Table 4.1. These images demonstrate wide variation in crater size and location due to fluctuations in the multimodal Holmium laser beam profile, which creates high intensity hotspots in different locations on the fiber face.

It should be noted that in addition to laser induced proximal fiber tip damage represented by ablation craters, buildup of debris was also observed on some Holmium fiber tips (Figure 4.6). This may be due in part to accumulation of particulates from the creation of the ablation craters, but is more likely due to foreign contaminants produced by the surrounding fiber layers and SMA905 connector materials (e.g. melted glue used to permanently attach silica fiber inside stainless steel ferrule). It is also possible that the Holmium beam either partially overfilled the fiber core and/or was misaligned, so that the incident beam resulted in ablation of the surrounding materials. Finally, a direct comparison of proximal fiber damage induced by the Holmium and TFL is provided in Figure 4.7. These images are at the same scale, representing the difference in amount of proximal fiber tip damage produced by the two lasers.

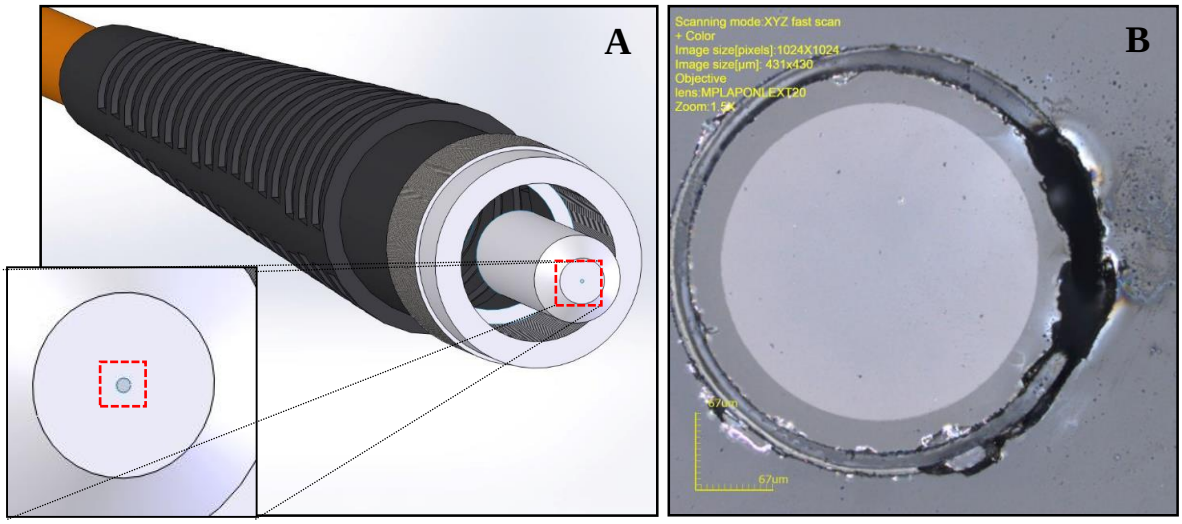

Figure 4.3: (A) Rendering of SMA 905 connector with fiber at center. Inset image indicates area of connector imaged with confocal microscopy. (B) Confocal (20x) image of pristine unused 270-µm-core proximal fiber tip for use in Holmium laser lithotripsy. From center outward the layers are core (light grey), cladding (medium grey), glue (dark grey), and buffer (medium grey) between fiber and metal connector. The dark area visible from 2 to 4 o'clock is a void or defect where glue has separated from fiber and buffer.

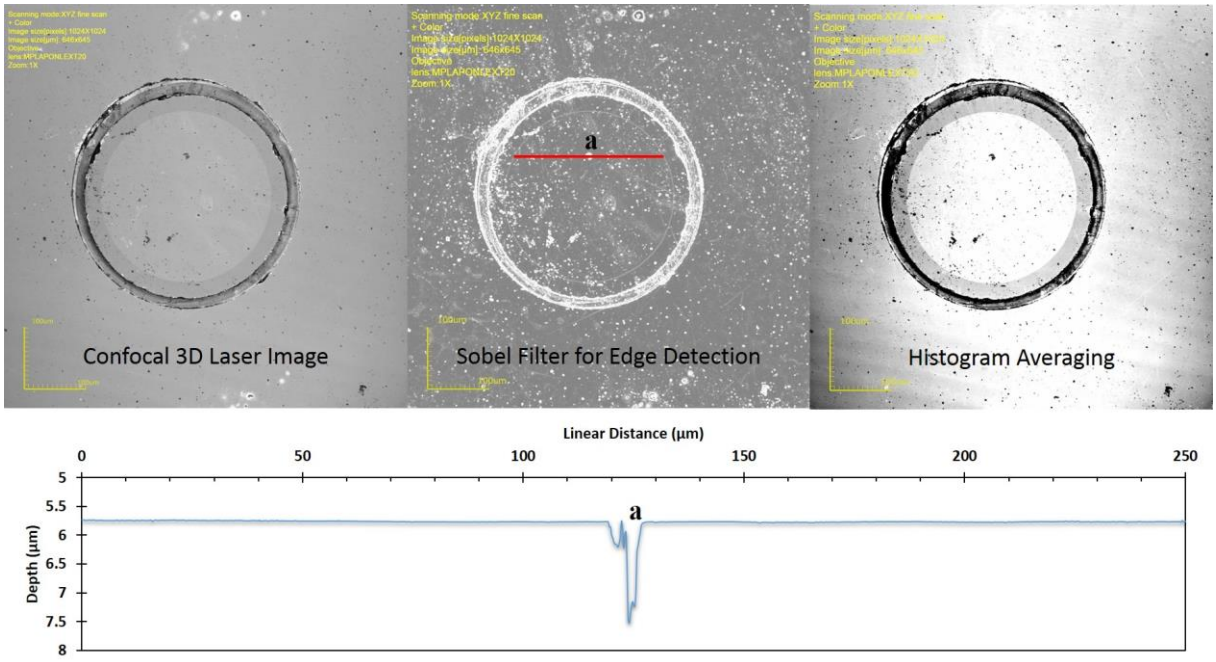

Figure 4.4: (Top) Left to right: Confocal (20x) image of 270-µm-core proximal fiber tip after 9302 pulses during Holmium laser lithotripsy (Fiber #19 in Table 4.1). The center image employs a Sobel filter for edge detection. The right image uses histogram averages for high contrast. (Bottom) Surface roughness measurement in micrometers over specified 1.8 µm deep crater of interest (a), indicated by red line in top center image.

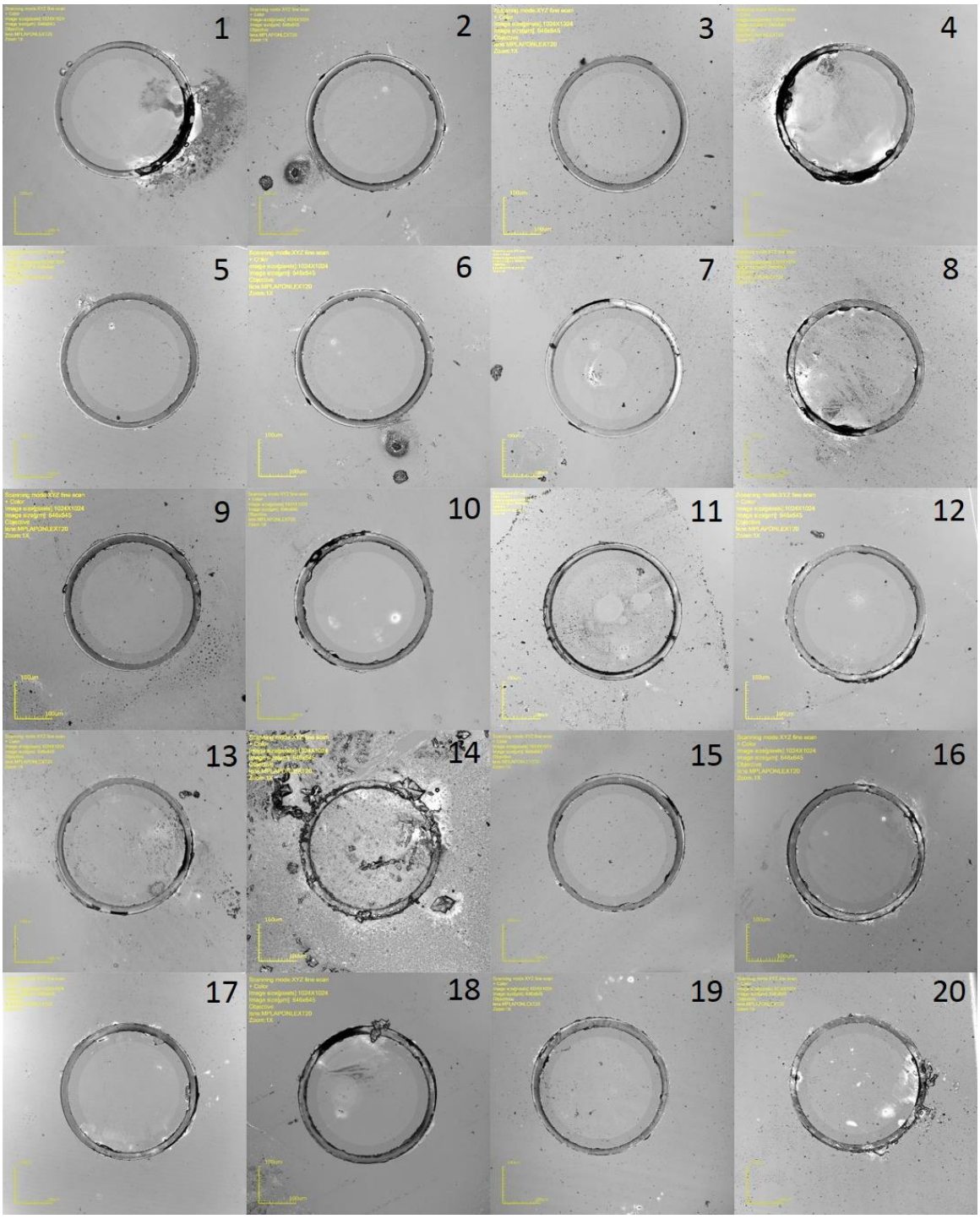

Figure 4.5: Grid showing damaged 270-µm-core fibers following Holmium laser lithotripsy with increasing number of pulses, from left to right and up to down. Dark regions surrounding fiber cladding are voids/defects similar to that seen in Figure 4.3. The number in top right corner of each image corresponds to the fiber number provided in Table 4.1.

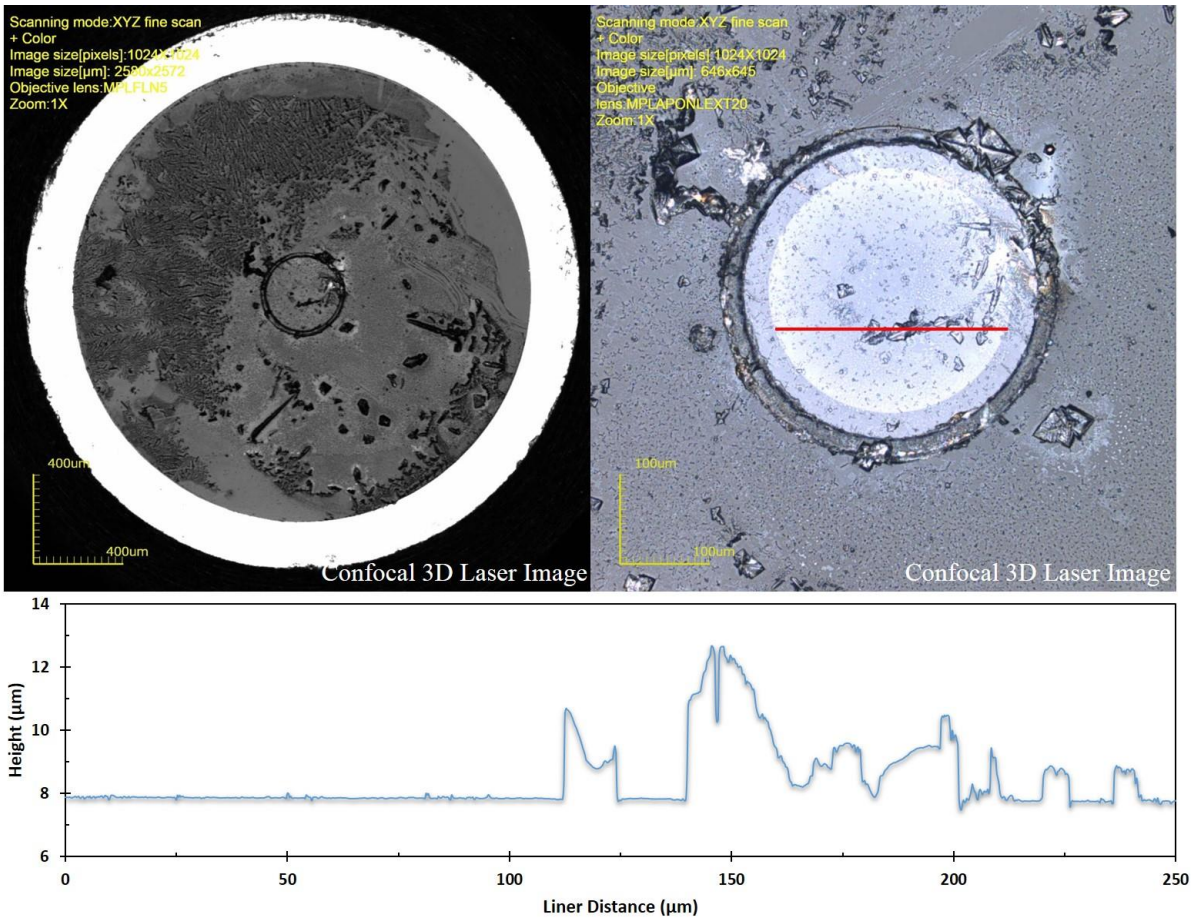

Figure 4.6: (Top) Left to right: Confocal (5x) image of debris covered 270-µm-core proximal fiber tip after 4774 pulses following Holmium laser lithotripsy (Fiber #14 in Table 4.1). Confocal (20x) image of same debris covering proximal fiber tip. (Bottom) Surface roughness measurement in micrometers over specified debris of interest, indicated by the red line in top right image.

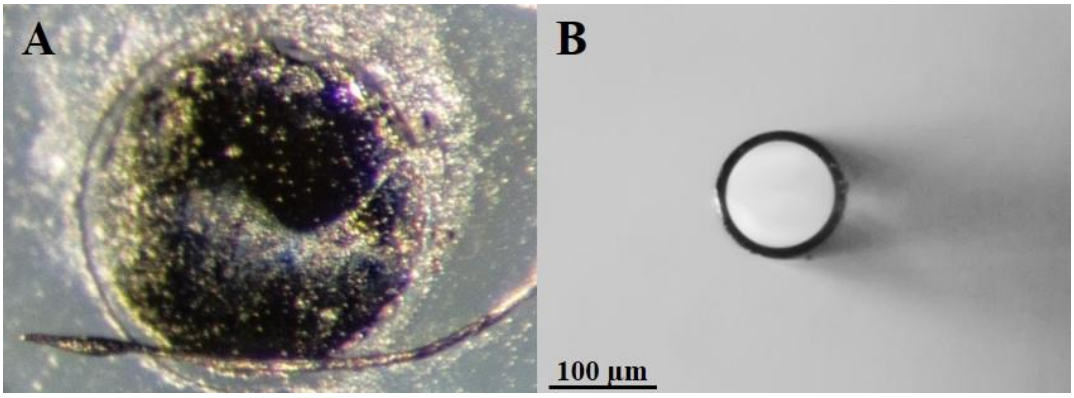

Figure 4.7: (A) Damaged, 270-µm-core proximal fiber tip after a single clinical Holmium laser lithotripsy procedure (600 mJ, 6 Hz, 3.6 W). (B) Undamaged, 105-µm-core proximal fiber tip after delivery of 500,000 pulses (35 mJ, 500 Hz, 17.5 W). Images in (A) and (B) are taken at the same scale.

4.1.4 Discussion

We have previously reported that the TFL, when operated at an energy of 35 mJ per pulse, pulse duration of 500 µs, and pulse rate of 150 Hz or greater, can ablate kidney stones at rates faster than the Holmium laser operated with standard parameters (600 mJ, 350 µs, 6 Hz) [24]. The results of this study also demonstrate that the TFL input fiber can deliver greater than 500,000 pulses at an average power of up to 17.5 W (35 mJ at 500 Hz) without proximal fiber tip degradation, potentially enabling the TFL fiber to withstand use in multiple laser lithotripsy procedures. This result contrasts with the damage observed on the proximal fiber tip after a single Holmium laser lithotripsy procedure at an average power of only 3.6 W (600 mJ at 6 Hz), as shown in Figure 4.7 (a) and the confocal microscope images in Figures 4.4 and 4.5. Although fiber handling in the clinic may have contributed to some of the proximal fiber tip damage observed, Holmium fibers also displayed numerous pock marks and craters that can only be explained by laser induced damage.

It should be noted that this preliminary study only examined one type of Holmium laser, surgical fiber, and connector. There are a variety of Holmium lasers available in the clinic (each with their own integrated fiber coupling optics), just as there are multiple manufacturers of Holmium fibers, and specialty proximal fiber optic connectors available as well. It is therefore reasonable to assume that there will be some variation in the amount of proximal fiber tip damage observed, dependent on the combination of laser, fiber, and connector used and the quality of manufacturing. Nevertheless, despite all of these variables, Holmium laser technology suffers from inherent limitations, including a multimodal beam profile, thermal lensing effects in the laser rod, and overfilling of small

fiber core diameters. These limitations cannot be completely overcome by simply changing manufacturers.

Future experimental studies may require longer fatigue testing of the TFL fibers through delivery of a greater number than the 500,000 pulses used in this preliminary study. A more robust experimental setup capable of recording in real time the formation of ablation craters in the proximal fiber tip of Holmium fibers is also warranted, and would help explain the origins of the damage observed, as well as providing insight into the mechanism of damage. The ability to directly correlate detailed zones of damage on the proximal fiber surface with hotspots from the incident Holmium laser spatial beam profile at a specific time point would also be insightful.

In general, the damage threshold of fused silica is very high, so direct laser induced damage through ablation of a clean silica fiber tip is unlikely. However, even finely polished fiber surfaces may become damaged at relatively low laser pulse energies if the fiber is poorly prepared and the proximal surface becomes contaminated. Out-gassing from the adhesive used during fiber connectorization and/or the hard cladding on the fiber may be sufficient to contaminate the fiber surface. Such materials may preferentially deposit as a thin film on the proximal fiber tip, which is typically cooler than the surrounding stainless steel ferrule during laser irradiation. The presence of these contaminants combined with hotspots produced by the multimodal Holmium laser spatial beam profile may be sufficient to induce thermal damage in the form of ablation craters on the proximal fiber surface, as observed in this study.

The confocal microscope constructs 3D representations via stitching of up to 500 images obtained with a 405 nm laser diode to create a high-resolution, wide-field image,

allowing for 3D display and measurements. This feature is an essential tool as the high numerical aperture yields a shallow depth of field which would traditionally render global imaging impossible. This stitching capability further allows for resolution beyond the diffraction limit, with the ability to resolve 0.12 μm XY line-width, and provides 0.8 nm scale Z-axis resolution. Line roughness measurement functions within the LEXT software allow for precise depth measurements across the face of a fiber which can confirm craters seen in the traditional 2D images. However, there are limitations to confocal imaging. On board algorithms limit aberrations to a degree, but microscopic turbulence can cause artifacts in the image and may potentially add error to measurements.

The Sobel gradient filter used for edge detection constructs an image highlighting the edges by determining the magnitude of local changes in brightness and create a final image pinpointing craters that are difficult to distinguish in a traditional image. A classic example is illustrated in Figure 4.8 which utilizes a form of Sobel filtering on the standard “Lena” image.

Figure 4.8: (Left) Traditional Lena image. (Right) Lena image with sobel filtering mask.

4.1.5 Conclusion

The proximal end of a 105-µm-core, silica optical fiber delivered greater than 500,000 Thulium fiber laser pulses at average power up to 17.5 W, without evidence of degradation (no pits, cracks, or craters). By comparison, fibers collected after Holmium laser lithotripsy procedures in the clinic revealed damage on all 20 fibers examined with as few as 117 pulses delivered, and at average power of 3.6 W. Craters observed were up to several micrometers in depth, on the same order as the Holmium laser wavelength (λ = 2100 nm), supporting previous reports that proximal fiber tip damage reduces laser transmission through the fiber. These results also suggest that the TFL beam profile may reduce or even eliminate proximal fiber tip damage, motivating re-use of fibers during multiple lithotripsy procedures with potential cost savings.

4.2 Stone Basket Integration

4.2.1 Background and Overview

Numerous endoscopic devices, including balloons, stone cones, accordions, baskets, and thermosensitive polymeric gel plugs, have been used in the clinic to minimize stone retropulsion [34]. The stone basket is commonly used to retrieve stone fragments and minimize stone retropulsion during Holmium laser lithotripsy. However, simultaneous application of a standard 270-µm-core Holmium laser fiber (464-µm-OD) and a conventional 1.9-Fr (633-µm-OD) stone basket severely limits saline irrigation rates due to space limitations in the single 3.6 Fr (1.2-mm-ID) working channel of the ureteroscope. Saline irrigation during laser lithotripsy is important for flushing away stone debris and maintaining adequate visibility in the surgical field for safety. While larger basket devices accepting fibers are commercially available, including 2.5 Fr (833-µm-OD) sheath with 150-µm-core fiber and 3.0 Fr (1.00-µm-OD) sheath with 270-µm-core fiber, they do not appear to be widely used, possibly due in part to concerns with reduced irrigation rates and the larger, less flexible stone baskets.

The excellent, near-single mode spatial TFL beam profile allows coupling of higher laser power into smaller fibers than the Holmium laser [17,19]. Therefore, use of smaller 100-µm-core fibers (140-µm-OD) with the TFL may enable further miniaturization of current ureteroscopy tools, including stone baskets, which should in turn translate into higher saline irrigation rates through the ureteroscope working channel, and hence improved visibility and safety as well. Impedance of irrigation through the ureteroscope working channel is a significant clinical concern which has motivated the continued development of smaller diameter stone baskets for improved irrigation [56-58].

Another limitation of smaller fibers is that they are more delicate and hence more susceptible to fiber fracture, degradation, and/or burnback during laser lithotripsy [59]. Our research group has recently reported on use of small fibers with a novel hollow stainless steel distal tip design for reducing fiber damage during TFL lithotripsy [54].

The main objective of this study is to describe construction, characterization, and *ex vivo* testing of a novel miniaturized and integrated hollow steel tip fiber and stone basket device. It is designed not only for minimization of stone retropulsion for more efficient TFL ablation of urinary stones, but also improved flexibility, higher saline irrigation rates and decreased fiber burnback, compared to separate use of non-integrated fibers and stone baskets.

4.2.2 Methods

4.2.2.1 Thulium Fiber Laser Parameters

A 100-Watt, continuous-wave, Thulium fiber laser (TLR 110-1908, IPG Photonics, Oxford, MA) with a center wavelength of 1908 nm was used in these studies. A 25-mm-FL plano-convex lens (LA1560-C, Thorlabs, Newton, NJ) was used to focus the 5.5-mm-diameter collimated fiber laser beam down to a spot diameter of ~ 25 μm ($1/e^2$) for coupling into the 100-μm-core optical fiber (FIP100120140, Polymicro, Phoenix, AZ). The laser was electronically modulated with a function generator (DS345, Stanford Research Systems, Sunnyvale, CA) to produce a pulse energy of 33 mJ, pulse duration of 500 μs, and pulse rate of 500 Hz for all lithotripsy studies. This pulse rate was chosen based on recent studies which showed that high ablation rates could be achieved using bare fiber delivery at pulse rates up to 500 Hz, and that the stone ablation rates scaled linearly with laser pulse rates [44].

4.2.2.2 Hollow Distal Tip Fiber Design

A low-OH, silica trunk fiber with a core and cladding diameter of 100 and 120 μm, respectively, and a length of 2 m was used. The polyimide fiber buffer (140-μm-OD) was removed up to 1 - 3 mm from the distal fiber tip. Stainless steel hypodermic tubing (B000FMWK6A, Amazon Supply, Seattle, WA) with an inner and outer diameter of 178 and 356 μm, respectively, cut to a length of 5 mm was used for each hollow tip. To clean the cut and free burrs from the inner hole, a 170-μm-diameter drill bit (R05WS95, Drill Bit City, Prospect Hts, IL) was used to counterbore the end holes of the steel tube. A micromanipulator (460A-XYZ, Newport, Irvine, CA) was used under magnification to recess the fiber in the tube to the specified depth of 500 μm. This value was based on the

results of previous studies, which showed that a further recession depth would result in significant power loss due to poor wave guiding ability of the hollow tip stemming from features on the tip surface larger than the TFL wavelength, while a shorter recession distance resulted in higher fiber tip degradation during stone ablation [54]. A small amount of high temperature RTV silicone (Permatex, Hartford, CT) was then placed on the back end of the tube and fiber jacket to fix the tube and fiber together. A diagram of the hollow fiber tip is shown in Figure 4.9.

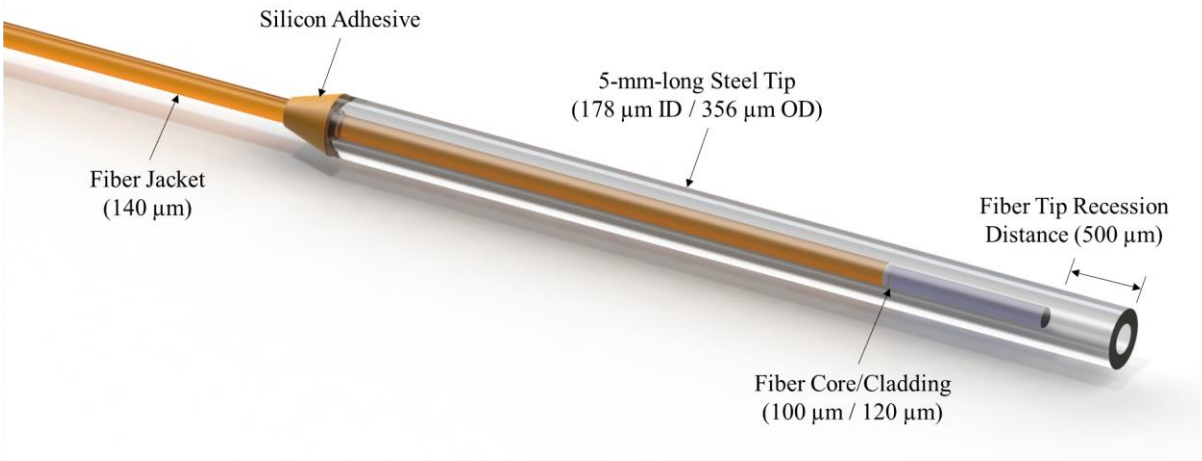

Figure 4.9: Diagram showing 100-µm-core silica distal fiber tip recessed 500 µm inside the hollow stainless steel tubing.

4.2.2.3 Fiber Integration with Stone Basket

A stone basket (Zero Tip Nitinol Stone Retrieval Basket, Boston Scientific, Natick, MA) with sheath outer diameter of 1.9 Fr (633 µm) was dismantled to salvage the insertion sheath. A second stone basket (Optiflex Nitinol Stone Retrieval Basket, Boston Scientific, Natick, MA) with sheath outer diameter of 1.3 Fr (433 µm) was also dismantled for the nitinol 4-wire cage and wire for manipulation. These harvested parts

were then combined with the 100-µm-core trunk fiber and hollow steel tip to comprise an integrated fiber/basket device, as shown in Figure 4.10.

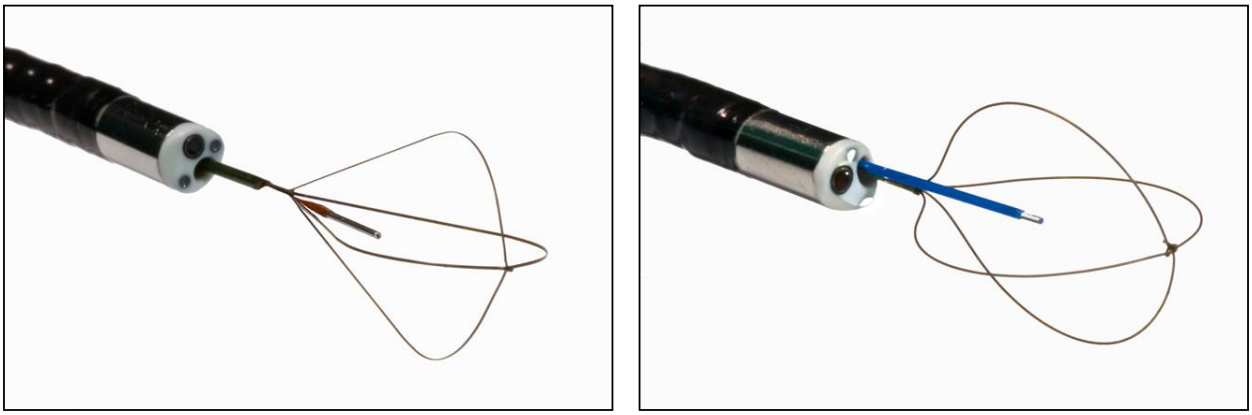

(a) (b)

Figure 4.10: (a) Integrated device consisting of 100-µm-core fiber with hollow steel distal tip and 1.3 Fr basket inside a 1.9 Fr sheath, through the working channel of a flexible ureteroscope; (b) Conventional 270-µm-core fiber side-by-side with 1.9 Fr basket, through the ureteroscope work channel, for comparison.

4.2.2.4 Thulium Fiber Laser Ablation of Kidney Stones

Human uric acid (UA) stones with > 95% purity were obtained from several stone analysis laboratories, including LabCorp (Oklahoma City, OK), Louis C. Herring & Co (Orlando, FL) and Carolinas Medical Center (Charlotte, NC). The UA stone samples ranged in size from 4 - 11 mm and in mass from 164 - 476 mg (mean = 349 ± 142 mg). Stone samples were desiccated in an oven for 30 min. at 70 °C and then weighed with an analytical balance (Model AB54-S, Mettler-Toledo, Switzerland) before and after lithotripsy experiments to determine total mass loss.

The experimental setup consisted of a rigid ureteroscope (MR6, Circon ACMI, Stamford CT) attached to a light source (X7000, Stryker Endoscopy, San Jose, CA), CCD camera (1188HD, Stryker), and monitor. The laser fiber and stone basket were inserted through the 3.4 Fr (1.1-mm-OD) ureteroscope working channel, and then placed

in contact with the stone sample, which was submerged in a saline bath (Figure 4.11). Illumination from the ureteroscope and a magnified image from the CCD camera, connected to a monitor, were used to observe the procedure. The integrated hollow tip testing involved using a 1.3-Fr (0.433-µm-OD) stone basket as a standard approach for stabilization of the stone which would otherwise be free to migrate. The fiber was only manipulated along the z-axis based on the integrated design, under slight pressure to keep the fiber tip in contact mode with the stone surface.

TFL energy was delivered through the hollow fiber tips to the stone surface in contact mode. The stone vaporization rate (mg/s) was calculated by determining the net mass loss of stones as a function of laser irradiation time. All residual stone samples greater than 2 mm were included in the measurements, consistent with the clinical endpoint for successful stone fragmentation. A minimum of five samples were tested for each data set, and the mean $\pm$ standard deviation (S.D.) was recorded. A paired Student's t-test was performed to determine statistical significance ($P < 0.05$).

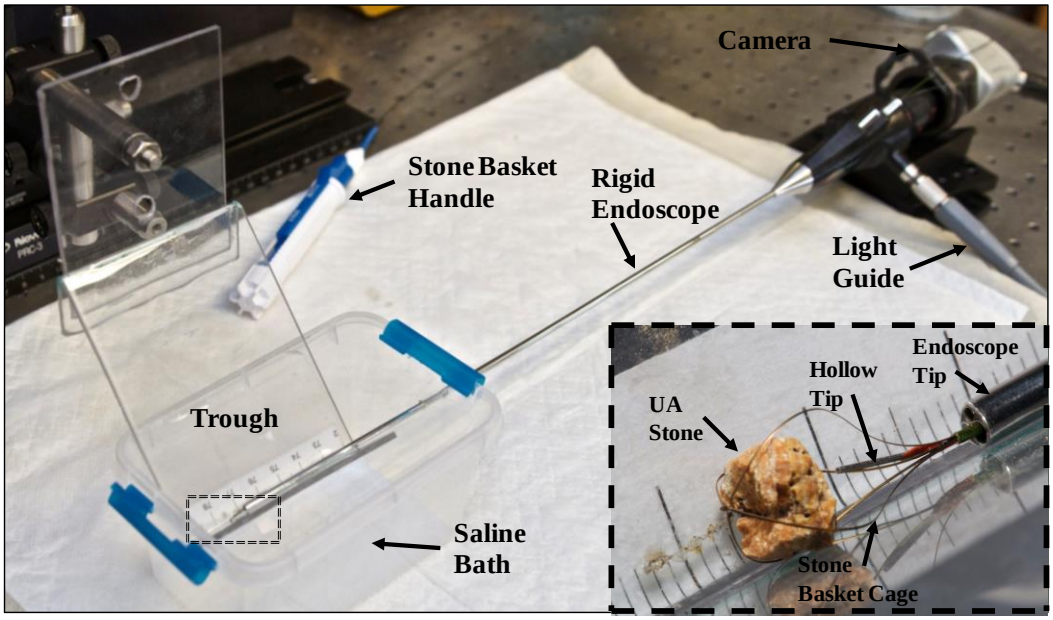

Figure 4.11: Experimental setup used for Thulium fiber laser lithotripsy with integrated fiber and stone basket device.

4.2.2.5 Saline Irrigation Rates

Saline irrigation rates were measured by introducing gravitational flow from a saline bag (at a fixed height of 100 cm) through the 3.6 Fr (1.2 mm) single working channel of a flexible ureteroscope (Uretero-Reno Videoscope URF-V, Olympus, Southborough, MA). Saline flowed freely through the ureteroscope for 2 minutes for each experiment.

Studies were conducted using a combination of different fibers and stone baskets, including experimental 100-µm-core silica fiber (FIP100120140, Polymicro, Phoenix, AZ), clinical 270-µm-core fiber (Holmium Lightguide 270D fiber, Olympus Gyrus ACMI), 1.3 Fr stone basket (Optiflex Nitinol Stone Retrieval Basket, Boston Scientific, Natick, MA) and 1.9 Fr urinary stone basket (Zero Tip Nitinol Stone Retrieval Basket, Boston Scientific). Saline volume was then measured with a graduated cylinder. A sample size of n = 3 was performed for each study with the mean ± standard deviation recorded. The percent flow rate was calculated by dividing flow with an instrument

inserted by flow through the empty working channel (control) without a fiber and/or basket present.

4.2.2.6 Fiber Tip Burn-Back and Degradation

After stone ablation, a separate 140-μm-OD fiber was placed into the distal opening of the hollow fiber tips and the inserted distance was measured. The overall fiber burn-back distance was recorded by comparing this measurement to the original depth before stone ablation.

4.2.2.7 Ureteroscope Bending Tests

The same flexible ureteroscope as used for the irrigation rate studies, described above, was also used to perform primary and secondary deflection tests both with and without the integrated fiber/stone basket inserted through the working channel of the ureteroscope. The maximally flexed ureteroscope configurations were photographed, and then a protractor was used to measure the deflection angle.

4.2.3 Results

4.2.3.1 Stone Ablation Rates

TFL stone ablation rates using the integrated fiber/basket device measured 1.5 ± 0.2 mg/s for the UA stones, comparable to 1.7 ± 0.3 mg/s (P = 0.15) using standard bare fiber tips separately with a stone basket. Figure 4.12 shows a UA stone sample before and after TFL ablation with pulse energy of 31.5 mJ, pulse duration of 500 µs, and pulse rate of 500 Hz.

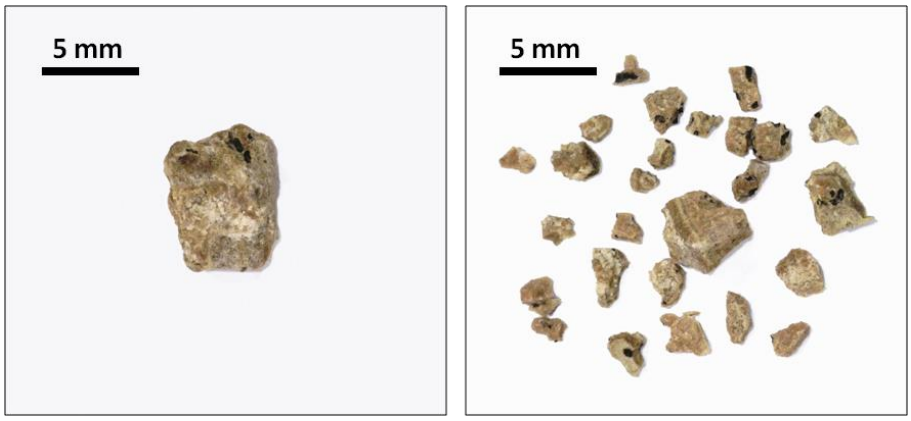

(a) (b)

Figure 4.12: Uric acid stone sample (a) before and (b) after TFL lithotripsy at 31.5 mJ, 500 µs, and 500 Hz with the integrated fiber/basket device. Initial stone size and mass was 6 x 7 x 9 mm and 164 mg, respectively. Laser irradiation time was 75 s.

4.2.3.2 Saline Irrigation Rates

Table 4.2 shows the saline irrigation rates through the single working channel of a flexible ureteroscope as function of the instrument (fiber and/or stone basket) size for the components of our integrated device, and also compares these flow rates to conventional instruments. A comparison of our integrated instrument (100-µm-core fiber, 1.3 Fr basket, and 1.9 Fr sheath) to simultaneous use of conventional 270-µm-core fiber and 1.9 Fr basket provides flow rates of 19.2 % and 7.7 % of the empty channel flow rates,

respectively. Thus, use of the integrated device improved irrigation flow by a factor of 2.5. In other words, the integrated device provided an additional instrument (100-µm fiber) within an overall conventional 1.9 Fr sheath, but with no further reduction in flow rates.

Table 4.2: Irrigation rates through the working channel of a 3.6 Fr (1.2 mm) flexible ureteroscope.

Instrument	Flow Rate (ml/min)	Flow (%)
Empty Channel	31.3 ± 0.6	100
Fibers [core/cladding/jacket] OD (µm)		
100/120/140	25.8 ± 0.5	82.4
270/322/464	13.5 ± 0.2	43.1
Stone Baskets		
1.3 Fr (433 µm)	12.6 ± 0.2	40.3
1.9 Fr (633 µm)	6.0 ± 0.1	19.2
Fiber + Stone Basket		
100/120/140 + 1.3 Fr basket inside 1.9 Fr sheath	6.0 ± 0.1	19.2
100/120/140 + separate 1.9 Fr basket sheath	5.4 ± 0.1	17.3
270/322/464 + separate 1.9 Fr basket	2.4 ± 0.1	7.7

4.2.3.3 Fiber Tip Degradation and Burnback

No measurable amount of distal fiber tip burnback was observed after individual UA stone ablation studies, as determined by inserting a separate fiber into the hollow tip.

4.2.3.4 Ureteroscope Bending Tests

Figure 4.13 shows the influence of the integrated fiber/stone basket device on deflection of a flexible ureteroscope. Primary deflection with and without the device measured 240 and 260 degrees, respectively. Secondary deflection with and without the device measured 155 and 165 degrees, respectively. Previous studies have reported that maximum deflection of this specific ureteroscope decreased from 275 to 217 degrees (primary) and 180 to 161 degrees (secondary) simply with prolonged clinical use [60]. Thus, although there is some measurable loss of ureteroscope deflection using the integrated fiber/basket device, it appears to be minimal compared to the loss of flexion experienced with standard repeated use of the ureteroscope.

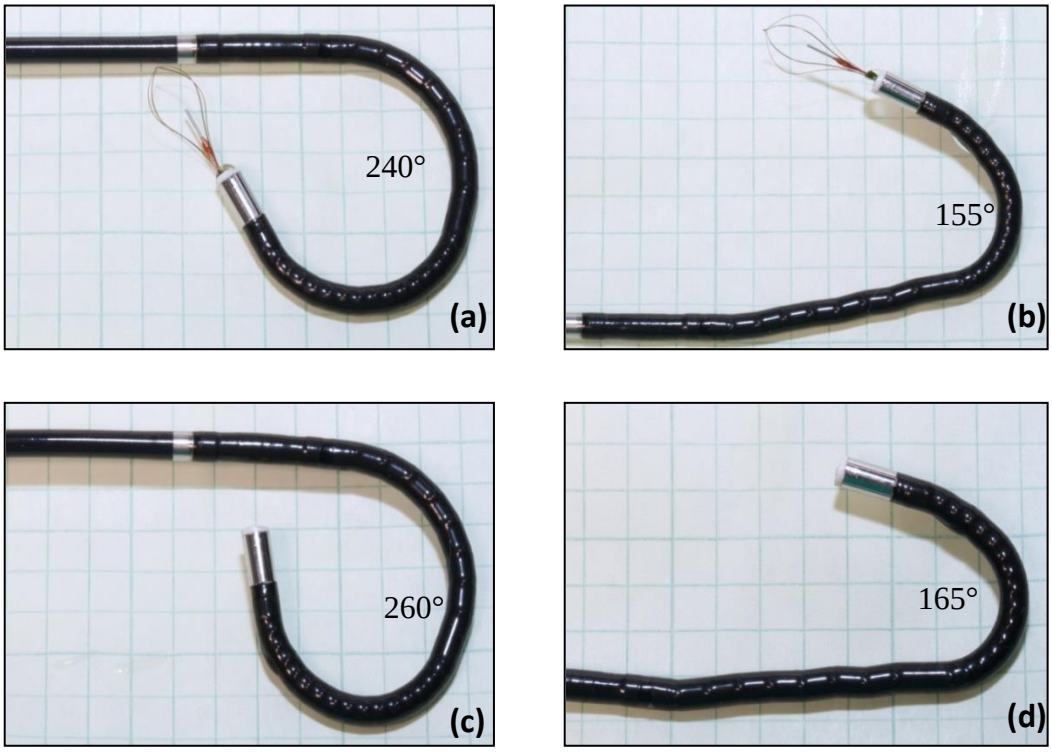

Figure 4.13: Ureteroscope deflection tests performed using integrated fiber/stone basket device inserted through the ureteroscope working channel. (a,c) Primary deflection with and without device; (b,d) Secondary deflection with and without device.

4.2.4 Discussion

An integrated 1.9 Fr (0.633-µm-OD) device consisting of a steel tip fiber and stone basket was successfully built and tested, providing comparable TFL stone ablation rates to that of bare fibers when operated at pulse rates up to 500 Hz. This device may provide not only more efficient stone ablation with minimal stone retropulsion, but also improved flexibility, higher saline irrigation rates, and reduced fiber burnback, compared to current use of separate, non-integrated, fiber and stone baskets. This miniaturized device is also significantly smaller than the smallest commercially available, 2.5 Fr (0.833-µm-OD) stone basket which accepts 150-µm-core fibers (Laser Flat Wire Stone Extractor, Cook Urological, Bloomington, IN). With further development, it may be possible to reduce the size of our integrated fiber/basket device below 1.9 Fr, using even smaller 1.2 Fr stone baskets [58], in combination with our recently tested 50-µm-core, 85-µm-OD fibers [19].

It should also be noted that some of our previous TFL lithotripsy studies reported the use of a different 100-µm-core fiber (AFS105/125Y, Thorlabs) with a thicker 250-µm-OD jacket [17,18,61,62]. However, due to its larger size, use of this fiber was not feasible for integration into the stone basket sheath, compared with the 140-µm-OD jacketed fiber.

There were several limitations of our design that should be addressed. TFL pulse energy measured 35 mJ using the bare fiber tip, but only 31.5 mJ using the hollow steel tip fiber due to transmission losses. This 10% lower output energy at a pulse rate of 500 Hz translates into an average power of only 15.75 W with steel-tipped fiber as compared with 17.50 W using the bare fiber at a full output energy of 35 mJ. This difference may

explain the slightly lower stone ablation rates using the integrated fiber/basket device. However, due to limitations in the TFL power output when operated in pulsed mode, it was not possible to increase pulse energy to compensate for this difference. It is also possible that the different stone basket designs (1.9 Fr vs. 1.3 Fr) contributed in part to the difference in TFL stone ablation rates.

Several modifications were necessary to our initial hollow steel tip fiber design to make it robust enough to withstand TFL lithotripsy at pulse rates up to 500 Hz. First, short steel tips which were initially 2-4 mm long were then extended to a length of 5 mm to provide greater heat conduction and to prevent glue from seeping directly onto the distal fiber tip. The longer steel tubing length also facilitated improved centering of the fiber inside the steel tip due to larger overlapping of the tubing with fiber jacket. Despite this modification, the rigid 5-mm-long steel tip is still significantly shorter than the 10-mm-long steel tips previously reported [54], and the rigid steel tips should be sufficiently short not to impede the maximum flexion of the ureteroscope inside the body. Second, a low viscosity, low temperature (82 ^{o}C) super glue (Locktite, Henkel, Rocky Hill, CT) was replaced with a higher temperature (316 ^{o}C) glue (RTV silicone, Permatex, Hartford, CT) that was also highly viscous. Third, to minimize transmission losses through the steel tip and maximize its waveguiding properties, the steel tip was counterbored, polishing the inner surface to provide maximum reflection. However, even after including these modifications, catastrophic failure of the device was still observed with repeated use of the fiber on multiple stones, due to fatigue at the metal tip, potentially caused by the high ablative temperatures experienced between the fiber tip and stone

surface. Therefore, continued refinement and improvement of the materials used in the design will be necessary prior to clinical use.

4.2.5 Conclusions

A novel integrated 1.9F (0.633-mm OD) device consisting of a steel tip fiber and stone basket was successfully built and tested, providing comparable TFL stone ablation rates to bare fibers when operated at pulse rates up to 500 Hz. This device may provide not only more efficient stone ablation with minimal stone retropulsion, but also improved flexibility, higher saline irrigation rates, reduced fiber burnback, and less probability of laser-induced nitinol wire damage, compared with current use of separate, nonintegrated, bare fiber tips with stone baskets. This miniaturized device is also significantly smaller than the smallest commercially available, 2.5F (0.833-mm-OD) stone basket that accepts 150-µm core fibers (Laser Flat Wire Stone Extractor, Cook Urological, Bloomington, IN). With further development, it may be possible to reduce the size of our integrated fiber/basket device below 1.9F, using even smaller 1.2F stone baskets, in combination with our recently tested 50-µm core, 85-µm OD fibers.

CHAPTER 5: URETEROSCOPE ILLUMINATION OPTIMIZATION FOR USE IN THULIUM FIBER LASER LITHOTRIPSY

5.1 Introduction

The aim of this chapter is to improve upon current clinical devices to increase patient safety. This is accomplished by the alteration of old designs in addition to the introduction of new geometries and light sources in an effort to overcome issues with physician visibility during ureteroscope imaging. Issues with current illumination include presence of shadows and hot spots in the images, made worse by the cavitation bubbles and stone debris present during laser ablation in a liquid environment. These concerns result in a decrease in ablation efficiency, increase in surgical operation time, and potential collateral tissue trauma. Previous experimental and clinical studies have reported perforation of the ureter and other ureteral trauma as a result of accidental damage to stone basket's Nitinol wires during Holmium laser lithotripsy, due in part to poor visibility [21-23, 38,39].

In current lithotripsy procedures, saline irrigation is flushed through the endoscope working channel in an attempt to resolve poor visibility created by stone dust and cavitation bubbles. Frequent irrigation of the working area is necessary; however, poor lighting may compound these problems. In order to increase patient safety from a visibility standpoint, illumination uniformity and image contrast is essential. This is accomplished by improving contrast through the use of ring-lighting geometry and Narrow Band Imaging (NBI).

5.2 Illumination Geometry

5.2.1 Introduction

Current optical illumination techniques used in video ureteroscopy operate under the flawed assumption that a single and sometimes double illumination points on the front face of the ureteroscope are sufficient for physician viewing of the operation area. This point-source illumination method provides a measured 45º of high intensity and a 70º total field of light, causing harsh shadows across stone and tissue surfaces, making differentiation between stones and adjacent soft tissues difficult to resolve. In an effort to counter this effect, many ureteroscope designs incorporate a cross lighting technique by overlapping two point sources similar to automobiles headlights or in the discipline of macro photography. Although this technique provides better coverage than its single point alternative, it still lacks uniformity. Furthermore, this configuration (Figure 5.1) separates the illumination ports from the viewing port, limiting lighting in the foreground.

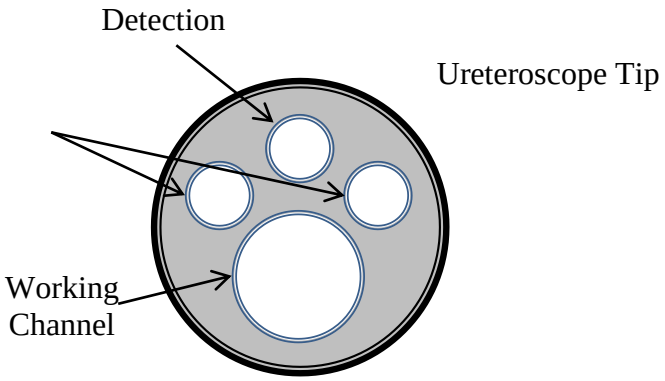

Figure 5.1: Diagram of conventional ureteroscope distal tip.

In macro photography, a common lighting technique for providing uniform illumination involves surrounding the front element of the viewing lens with a ring light. Photographers are often hesitant to use this approach due to cost, however this

configuration is optimal in terms of operation. Ring illumination has been adapted for use during surgery on a larger scale, such as Thoracic procedures [25]. We scale down this technology to a smaller footprint, outfitting our viewing optic with a ring configured illumination bundle (Figure 5.2). This orientation's purpose is two-fold; first, uniformity of light distribution for enhanced image quality, and second, to reduce the port footprint on the ureteroscope's distal tip.

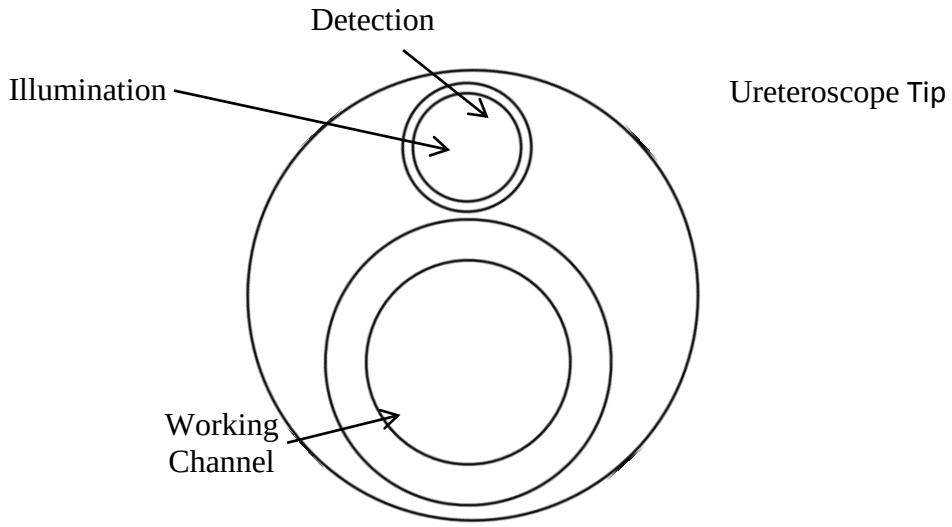

Figure 5.2: Diagram of proposed configuration with illumination ring surrounding the detection port, freeing up space from the dual illumination geometry.

5.2.2 Ring Illumination

Current ureteroscope designs incorporate a cross lighting technique by overlapping two point sources of a relatively high numerical aperture, eliminating harsh shadows in the horizontal direction, but not in the vertical direction. Although, this technique provides better coverage than its single point alternative, it still lacks uniformity necessary for inspection within the body, where short working distances make illumination challenging.

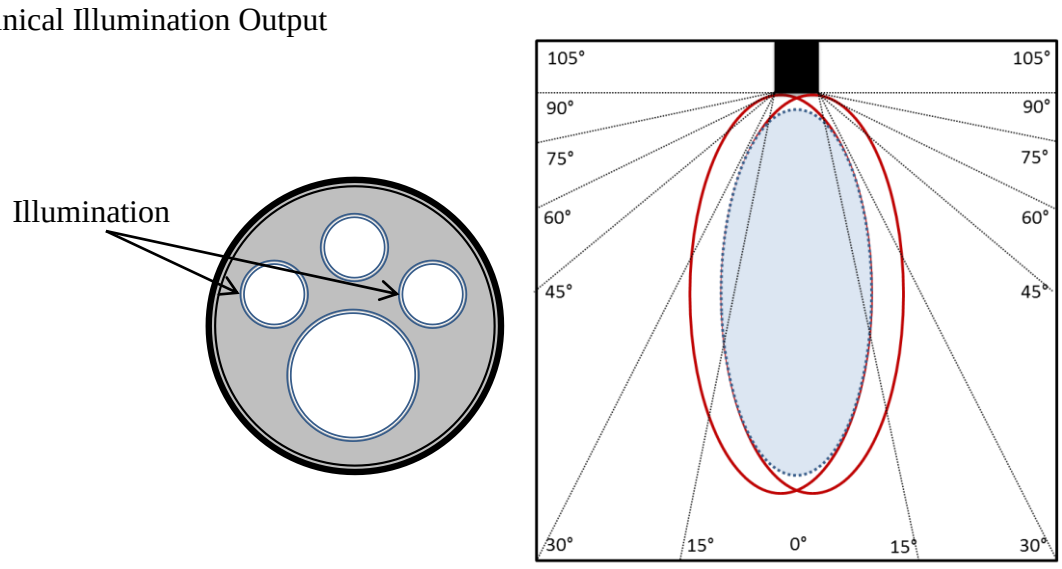

Figure 5.3: Diagram of conventional ureteroscope distal tip and corresponding luminous intensity distribution curve. The red circles represent field of illumination for individual sources, where the blue region signifies overlap of the two fields.

As seen in the luminous intensity distribution curves (LIDC) in Figure 5.3, the conventional illumination geometry for ureteroscopes is based on the cross-lighting principle in which two sources overlap for even lighting centered in front of the viewing optic (blue region). The configuration utilizes each source as a fill light for the other, highlighting dark areas created by its partner (red regions). However, the illumination points shown are not in line with the detection port, casting shadows above the subject,

and limiting visibility in the vertical direction. While this approach works well in aesthetic photography, creating interest and depth, a more disciplined image provided by uniform illumination is necessary for inspection photography or videography.

Uniform illumination has long been used within the macro photography world, even appearing in medical photography, but has been overlooked when medical imaging devices are miniaturized. Ring illumination softens shadows without eliminating necessary depth information. With the incorporation of high NA fibers, ring illumination is distributed over large angles, reducing glinting and hot spots. These hot spots may be further reduced by diffusing the light through polishing the ring lighting with a matte finish where the surface is rough on a microscopic scale.

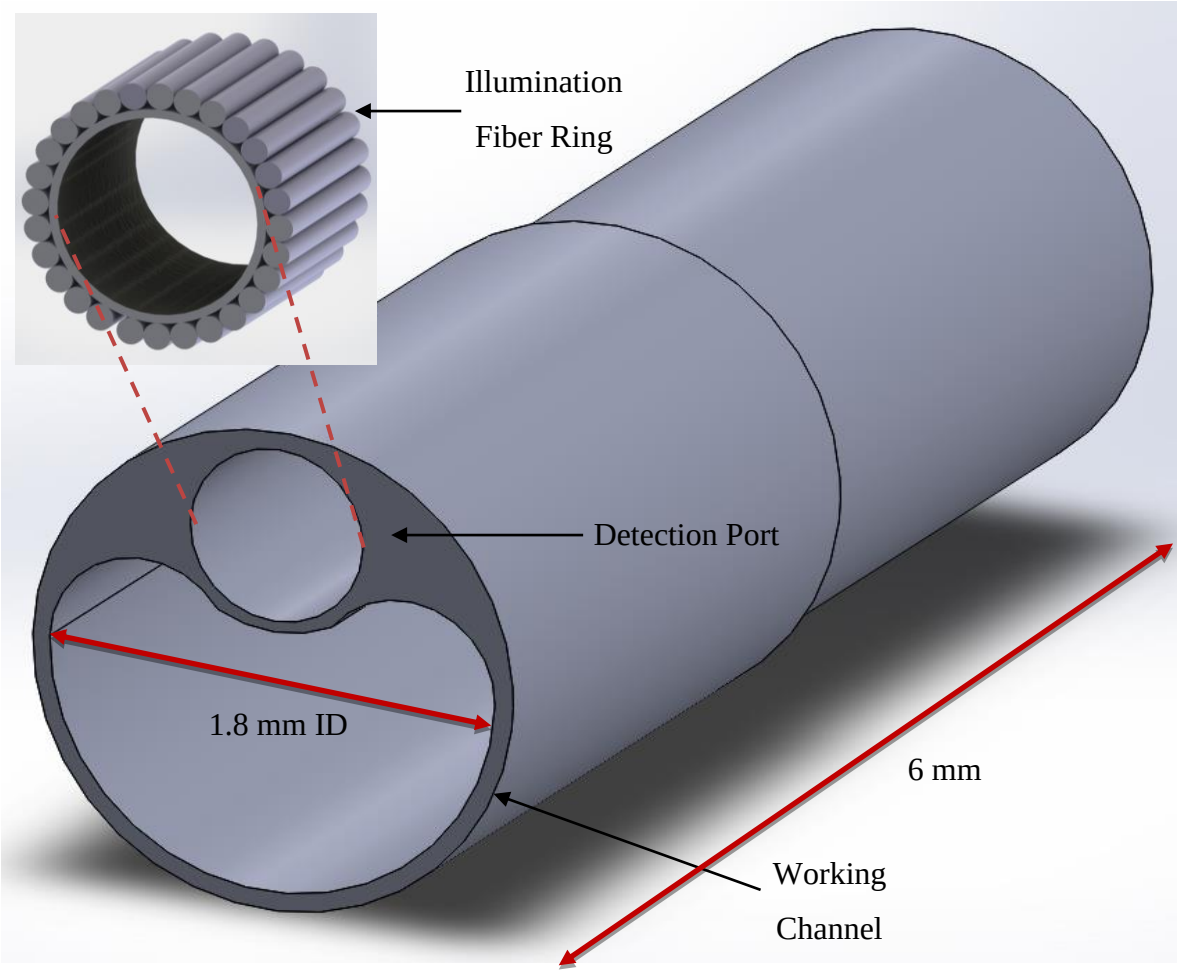

Figure 5.4: (Global) Miniaturized ureteroscope tip with two channels: Channel 1 for illumination and detection, Channel 2 for irrigation, fiber, and guidewire/stone basket. (Inset) Illumination fiber distribution within channel.

Figure 5.4 depicts the ring light geometry as we envision the structure within our miniaturized ureteroscope design along with our prototype coupling device. Ideally, a liquid light guide could be used in the future to eliminate dead space between fibers. The LIDC pictured in Figure 5.5 demonstrates the distribution difference in axially symmetric lighting geometry versus the traditional dual point source geometry. The overlapping field of even illumination is extended across the entire traditional uneven light field. The illumination falls outside the imaging field of view, which means that the experience of

falloff will be less pronounced within the image, even filling in shadows behind the subject through reflection off the kidney or ureter wall.

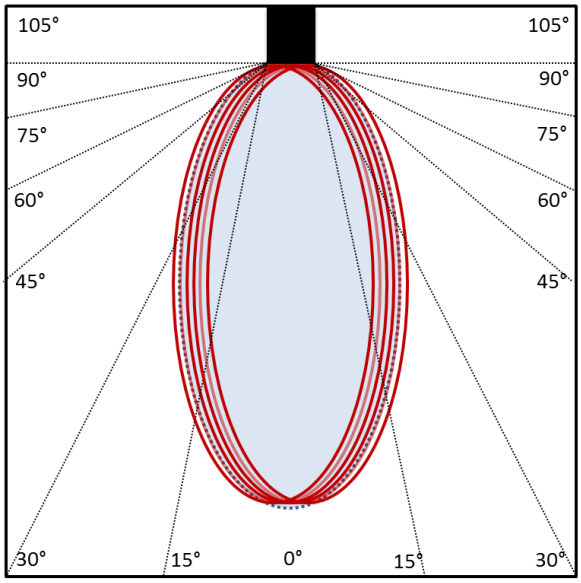

Figure 5.5: Luminous intensity distribution curve demonstrating the ring illumination's uniformity of distribution. The multiple red circles represent field of illumination for individual fiber sources, where the blue region signifies overlap of the multiple fields.

In this study we not only altered the illumination configuration (Figure 5.2), but also the lighting source itself. Previous studies have explored categories of light sources, even incorporating bandwidth manipulation. We evaluated reflectance spectroscopy results of broadband-halogen lamp fiber illuminator and human calculi versus ureter tissue in order to determine optimal narrow band illumination.

5.3 Narrow Band Imaging

Image uniformity and contrast is essential to increase visibility, and by extension, patient safety. This is accomplished by improving contrast through the use of ring-lighting geometry coupled with an optimized illumination spectrum. An optimal illumination will implement a multispectral source that manifests a separation between the main object and the background by way of spectral contrast, or maximizing the color distance between objects through selective absorption and scattering. Narrow Band Imaging (NBI), an optical image enhancement technology in which specific bandwidths are implemented, may be deployed to adapt to specific, differing tissues in order to increase image contrast and therefore visibility.

NBI is currently used in bladder cancer, colonic polyp, and Barret's esophagus detection and diagnostics during cystoscopy, whereby the illuminating light is composed of just two specific wavelength bands, blue (440-460 nm) and green (540-560 nm), which are strongly absorbed by hemoglobin [63-67]. Commercially available NBI integrated systems act by mechanical insertion of narrow band filters in front of a white light source [68, 69], employing 415 nm and 540 nm light sources. [70] In this case, the red light has been removed from the initial white light source via filters which can be electronically activated by the physician during procedure.

The shorter 415 nm wavelength penetrates the superficial layers of the mucosa and is absorbed by capillary vessels giving them an apparent brownish hue. The 504 nm wavelength penetrates more deeply, and is absorbed by blood vessels giving them a blue appearance. Where the shorter wavelength is useful for detecting tumors, the longer gives a better understanding of the vasculature of suspect lesions. [70]

Our need for NBI focuses not on vascularization, but rather the distinction between human urinary stones and the ureter and kidney walls. However, the main principles still apply. Previous experimental and clinical studies have reported perforation of the ureter during Holmium laser lithotripsy, due in part to poor visibility [21-23]. In order to properly use NBI for application in laser lithotripsy, it is necessary to gather spectral signatures for these specific hard and soft tissues to determine maximum color separation and optimal spectral bands for illumination. These spectrums may be obtained through white light reflectance spectroscopy and compared for maximum stone/tissue differentiation.

Brinkman et. al. have recently published findings on stone/tissue differentiation using diffuse white light reflectance spectroscopy as a feedback system for emergency laser shutoff. The group analyzed acquired spectra to discriminate between stone and tissue by the absence or presence of minima due to hemoglobin absorption at $\lambda_1 = 542$ nm and $\lambda_2 = 576$ nm. [71] While ratioed results are not necessary for our purpose, these methods can be extrapolated and applied for use in determining optimal wavelengths for NBI illumination.

5.3.1 Stone Composition

Stone samples used in the *in vitro* spectroscopy measurements were composed of calcium oxalate monohydrate, calcium oxalate dihydrate, uric acid, and calcium phosphate.

Figure 5.6: Representative kidney stones used in white-light reflectance spectroscopy. From left to right: COM, COD, UA, CaP.

5.3.2 Spectroscopy

5.3.2.1 Reflectance Spectroscopy

Reflectance spectroscopy, unlike fluorescence spectroscopy, operates under the principle that reflected light maintains the same wavelength since energy is not lost during scattering. This allows for a simplified model that assumes that all input light is either absorbed or reflected and enables us to determine reflectance spectra that are directly comparable when illuminated with the identical source. Absorption of input light provides information about the biochemical makeup of the illuminated tissue since absorption by the tissues occurs at specific wavelengths. [72]

White light reflectance spectroscopy has been previously reported to differentiate stone from tissue in order to implement an automatic feedback system which turns off the laser when the fiber is incorrectly positioned. [71] Reflectance signals were recorded and spectra were analyzed to discriminate between stone and tissue by the absence or presence of minima due to hemoglobin absorption at λ_1 = 542 nm and λ_3 = 576 nm. Stone and tissue signals may be correctly identified by calculating the ratio R = I (λ_1 = 542nm)/I (λ_2 = 475 nm): Due to the hemoglobin absorption at λ_1, R is smaller for tissue than for calculi.

5.3.2.2 Spectroscopy to Determine Optimal Illumination Wavelength

Reflectance signals from white light reflectance spectroscopy not only provide critical information for tissue differentiation, but further provide the spectra needed to create an optimized illumination spectrum for maximizing color distance between hard and soft tissues present during TFL lithotripsy. An optimized illumination source would allow physicians to more clearly identify and differentiate between stone and ureter and

maximize visibility over current clinical xenon sources, thus increasing patient safety. It is more advantageous for illumination to study direct signal response across the spectrum, and filter out overlapping responses from the source, where wavelength specific signal ratios aid in stone and tissue differentiation for laser cutoff systems.

Reflectance spectra for calculi and ureter have been previously published [71,73], but not separated by stone type. An illumination source could potentially be designed to clearly identify stone type and gain maximum contrast versus ureter, specific to stone composition.

5.3.2.3 Method

Stone and Ureter Samples

Human uric acid (UA), calcium oxalate monohydrate (COM) with > 95% purity, calcium oxalate dehydrate (COD), and 60% calcium oxalate monohydrate and 40% calcium phosphate (CaP) stone samples, were chosen as representative common stones for image testing [35]. Freshly harvested and spatulated porcine ureters were used as tissue samples for *in vitro* experiments. Samples were stored after excision and stored at T = 2°C in 0.9% saline solution. All measurements took place at room temperature in 0.9% saline solution within 48 hours after harvesting tissue.

Experimental Setup

Data was collected in total laboratory blackout with the exception of an illuminated computer screen on opposing end of room. Samples were illuminated with a 150 W quartz halogen fiber optic light source (I-150, Coherent, Santa Clara, CA), positioned 15 cm above the subject. Light was collected via a UV/VIS lab-grade patch cord (P600-1,

Ocean Optics, Dunedin, FL) positioned orthogonally, 5 cm above the target, with an approximate 10 mm field of view to isolate local signals of reflectance and scattering. Collected light was guided to a grating spectrometer (QE-PR0, Ocean Optics, Dunedin, FL) (Effective Measurement Range: 350-700 nm, resolution 1.25 nm).

Dark spectrum and light spectrum signals were acquired prior to stone and ureter reflectance spectrum testing for signal processing. Integration time of the spectrometer detector array was set to t = 100 ms for stones and t = 25 ms for the ureter tissue because signal saturation was high. N = 4 scans were conducted per output spectra, and N = 5 spectra were averaged for final curves by taking measurements at different points on each sample.

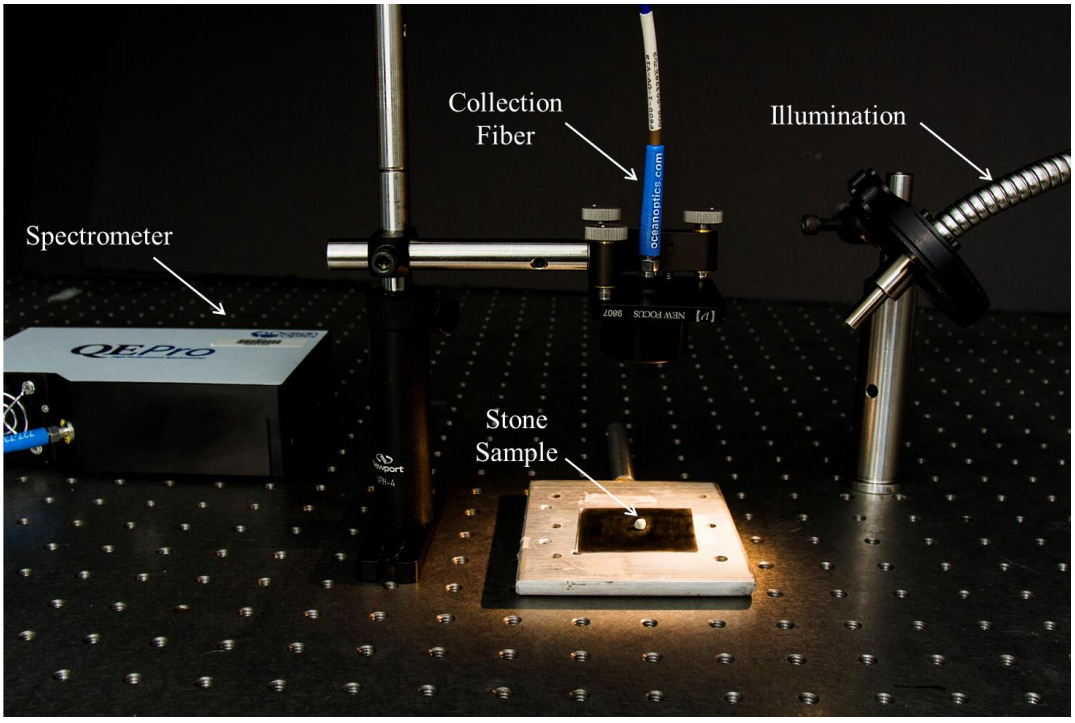

Figure 5.7: Experimental setup for reflectance spectroscopy, showing stone sample illuminated with broadband halogen source and detection fiber placed above sample.

Signal Processing

To determine reflectance profiles for both calculi and ureter, the raw data was corrected for dark spectrum through dark subtraction to first determine absorption using the formula below, where Known is the illumination source profile, Dark is the background spectrum profile, and Signal is the test sample profile.

$$\frac{(Known - Dark) - (Signal - Dark)}{Known - Dark} = Absorption$$

$$Reflection = 1 - Absorption$$

This dark spectrum profile (Known – Dark) refers to the signal detected when no light is present, either from the sample or ambient light. Its subtraction corrects for background noise in the sample signal [74].

5.3.2.4 Results

The porcine ureter reflectance spectrum was obtained and graphically normalized to match the known signal dissipation by the spectrometer of Halogen output, or known source profile from 680 nm to 690 nm (Figure 5.8a). This normalization allowed creation of a percent absorption and reflectance graph across the visible spectrum for ureter tissue as seen in Figure 5.8b. The same process was repeated for each stone type and the resultant percent reflectance values were provided in Figure 5.8c. By subtracting the average stone reflectance values from average ureter reflectance value, the percent difference from ureter reflectivity was determined (Figure 5.8d). In the graph, the percent difference is greater than 40% from 350 – 375 nm, 450 – 525 nm, and 600 – 700 nm, making these regions of the spectrum suitable for high contrast illumination.

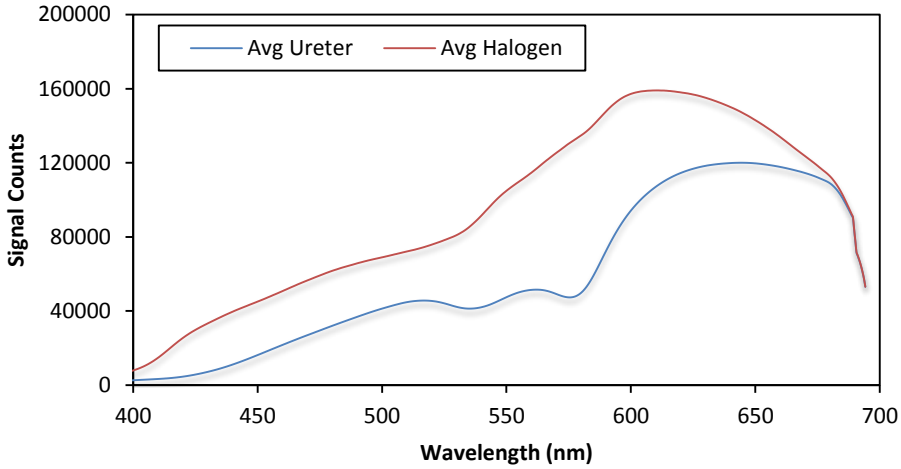

Figure 5.8a: Halogen Output vs Ureter Reflectance Normalized at 690 nm. Graph depicting normalized output of a halogen source vs porcine ureter reflectance within the visible spectrum used to determine absorption and, by extension, reflectance.

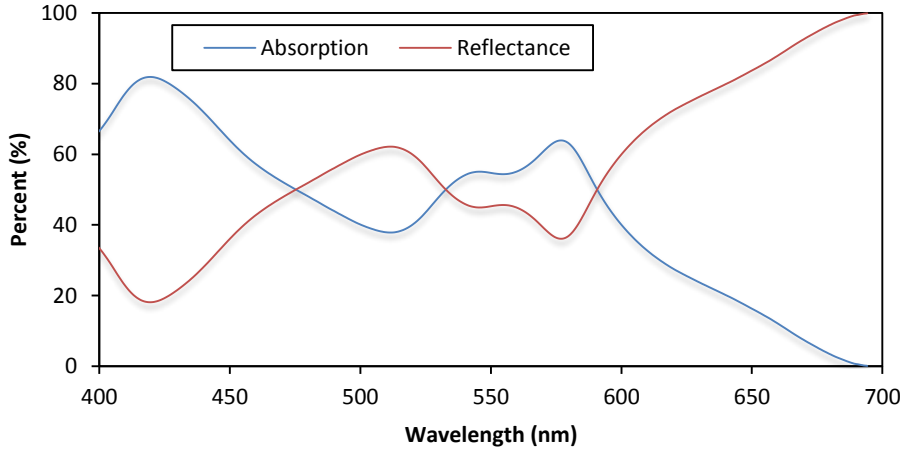

Figure 5.8b: Absorption and Reflectance Spectrums of Porcine Ureter. Graph depicting percent absorption vs reflectance for porcine ureter within the visible spectrum.

It is evident from Figure 5.8a that there are noticeable dips in the reflectance spectra of ureter tissue at ~ 540 nm and ~ 580 nm signifying the presence of residual deoxygenated blood in the sample. Figure 5.8b more clearly demonstrates absorption peaks matching those of oxygenated and deoxygenated blood in tissue (~ 420 nm, ~ 530 nm, and ~ 580 nm). Figure 5.8b is derived from Figure 5.8a through normalization by way of matching known signal tailing off from ~ 690 nm to 700nm. The reflectance signal is then subtracted from the known input signal to derive absorption and reflection.

Reflectance spectrums for kidney stones are comparatively level to that of the ureter, partially due to absorption across the board, giving the stones their dark color. The Uric Acid and Calcium Phosphate stones resemble the same spectral trends, however they yield higher reflectance values since they are more diffusely reflective. Since the stone spectrums are relatively flat, it makes sense that the percent difference graph follows the same trend as the ureter reflectance, with variations in magnitude dependent on the stone type.

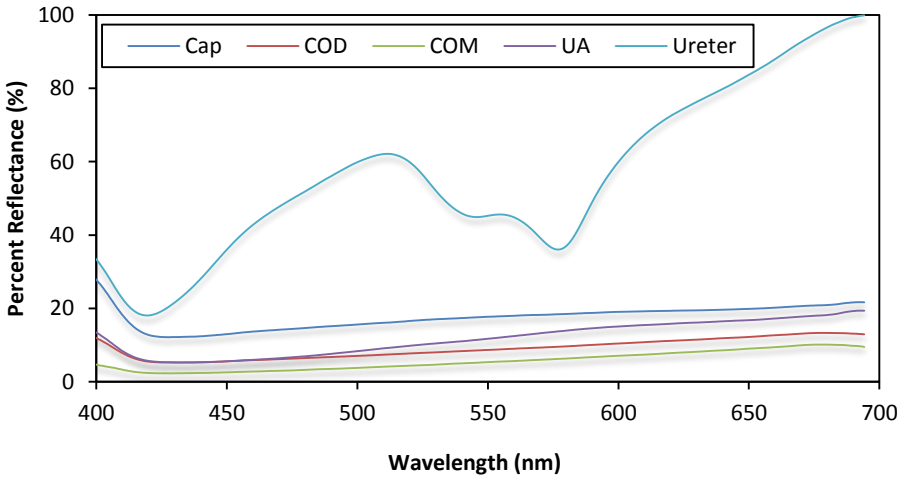

Figure 5.8c: Graph comparing percent reflectance within the visible spectrum between human calculi and urethral wall.

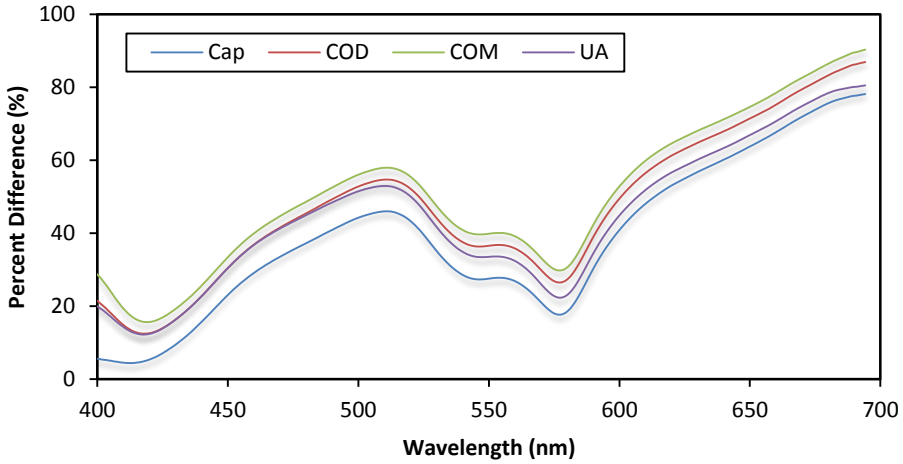

Figure 5.8d: Graph depicting percent difference of reflectivity within the visible spectrum between human calculi vs urethral wall.

5.3.3 Light Source Design

Current clinical procedures favor xenon light sources for their even distribution over the visible spectrum. However, reflectivity differences found in spectroscopy studies suggest an amendment to this current standard. A simple solution that would provide a spectrum peaking in the red in the visible would be to use a laser diode or tungsten-halogen source (Figure 5.9).

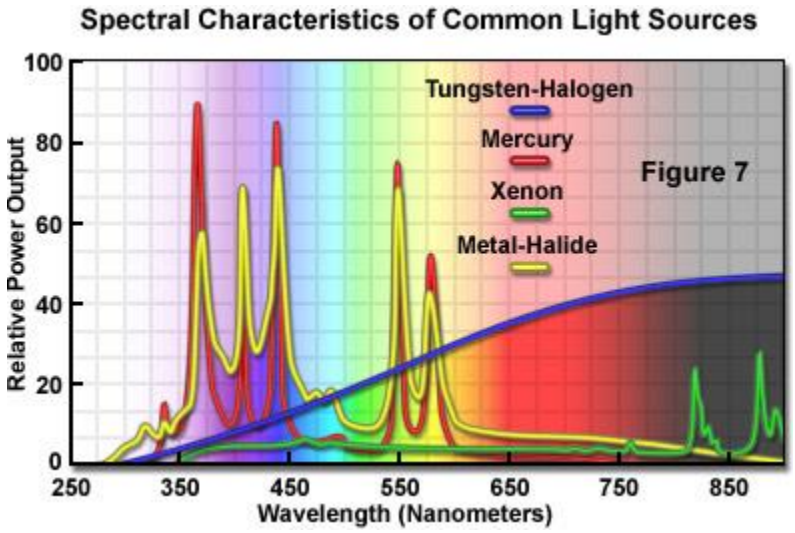

Figure 5.9: Spectral power output for common light sources from Nikon Microscopy. [75]

Diode sources employ this necessary spectral output, however, quasi-monochromatic illumination is harsh to the viewer, as seen in Figure 5.10, and is not practical since it would require changing sources during the procedure. A tungsten-halogen source would be less harsh to the eye and would not require separate sources. However, as shown by the depicted difference in reflectivity of the stones from the ureter, there are multiple wavelength regimes (present in both xenon and tungsten-halogen sources) where the percent difference dips below 40%, making differentiation difficult (Figure 5.11).

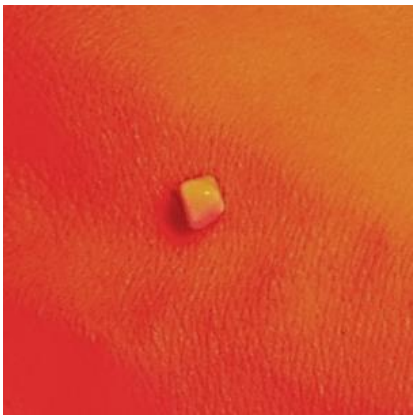

Figure 5.10: Representative CaP kidney stone on human dermis, illuminated with 635 nm laser diode.

A logical method to cut out these adverse sections of the illumination source spectrum would be to use a bandpass filter, allowing only 600 nm and above to propagate as ureteroscope illumination. However, there are not one but two regions where the percent difference is 40% or greater, within the visible spectrum (Figure 5.11).

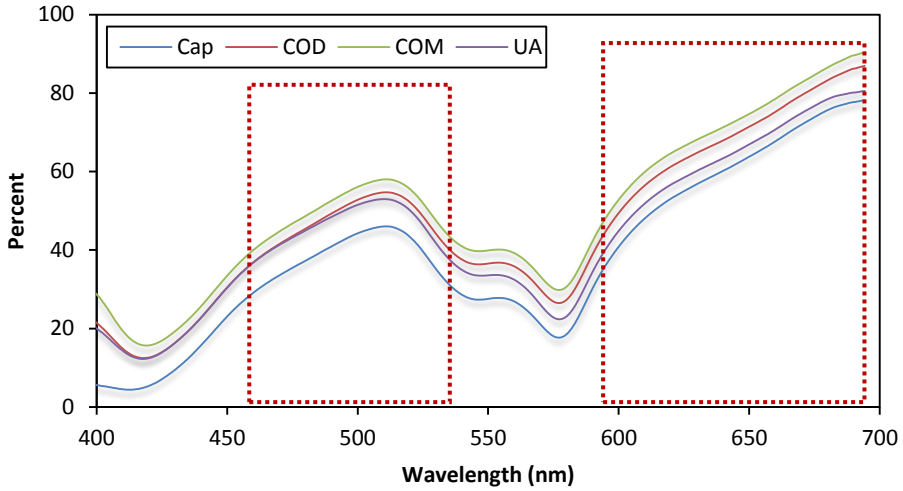

Figure 5.11: Graph depicting portions of the visible spectrum where percent difference of reflectivity between human calculi and urethral wall are 40% or greater.

Notch Filters or bandstop filters could potentially be used to cut out the undesirable range of wavelengths, specifically 375 to 455 nm and 535 to 595 nm.

5.4 Future Work

Physical Component Improvements

While initial studies have been conducted involving high numerical aperture optical fibers in a circular configuration, there is some an inherent loss of potential illumination from interfiber dead space. Future work should evaluate custom built plastic fibers and liquid light guides in the same ring orientation without the undesirable losses from circular fiber bundling. Further studies should also explore diffuse lighting by altering the distal end of the illumination guide to encourage scattering, reducing the “hot spot” effect which can effectively flatten an image by overexposing the foreground and decreasing depth perception.

Light Source Improvements

In this study we focus on multi sample illumination, with an aim to delve further into sample composition specific illumination in the future. Just as it was possible to determine optimal contrast increasing wavelengths for stones versus the ureter and adapt the illumination source accordingly, it is possible to replicate this process for different stone compositions. As the reflectance charts demonstrate, there is a distinct spectral reflectance signature for each stone type. From a research perspective, this is interesting. However, from a clinical standpoint, there is not much advantage in optimizing on a stone by stone basis where the high reflectivity of the soft tissue compared to the stones far surpasses differences in individual stones.

Future studies should explore real time improved ureteroscopy illumination via imaging stones inside sectioned saline submerged ureters with a filtered clinical light source.

5.5 Conclusion

While current optical illumination techniques used in video ureteroscopy allow physicians to perform surgery, current geometries and sources are inadequate to produce the necessary illumination for optimal visibility and safety during procedures. By moving from the single and double point source geometry to a ring configuration, the resulting output becomes more uniform in both axes, cutting down on shadows and increasing depth discernibility. The illumination source may be upgraded with use of narrow band imaging (NBI) to increase contrast between calculi and surrounding soft tissue. The implementation of an altered output from clinically used light sources via optical filters increases contrast and visibility without the added expense of a secondary source. These improved components of ureteroscope illumination may reduce complications from visibility during laser lithotripsy and increase patient safety.

CHAPTER 6: URETEROSCOPE MINIATURIZATION FOR USE IN THULIUM FIBER LASER LITHOTRIPSY

6.1 Ureteroscope Miniaturization

6.1.1 Introduction

Successful ureteroscope access into the ureter and upper urinary tract is a primary concern for urologists during endoscopic procedures, as blockage results in added procedural times, increased cost and potential complications. When the ureteroscope reaches a point where passage is stalled by a narrow lumen diameter, the surgeon must dilate the pathway. This may be performed actively by the use of either (1) a balloon dilator, (2) passage of sequential ureteral dilators or (3) passively via insertion of a temporary stent for approximately one week with the doctor returning to complete the procedure at a later time [76]. Since the limiting factor in this situation is the inner diameter of the ureter, the most direct method of providing easy access is to reduce the cross-sectional area of the ureteroscope. Over the past few years, the industry response has been to miniaturize ureteroscopes, with the smallest commercially available instrument currently having a distal end outer diameter of 5.3 Fr (1.76-mm-OD) through implementation of a bullet shaped (beveled) design, enlarging to 8.4 Fr (2.8-mm-OD) at the proximal end (URF-P5, Olympus, Center Valley, PA). Even this small design is insufficient for unhindered access into the ureter without manipulation techniques, providing either passive or active ureteral dilation, and requiring full anesthesia for the patient. An even smaller ureteroscope design would allow ureteroscope insertion without

need for dilation, saving time and materials costs, and limiting surgical complications and patient morbidity.

Our laboratory is currently investigating the experimental Thulium fiber laser (TFL) as a potential alternative to the clinical gold standard Holmium:YAG (Holmium) laser for lithotripsy. Our laboratory has further explored the use of miniaturized endoscopic devices in conjunction with the experimental TFL to increase patient safety while decreasing instrument size, in efforts to move toward smaller overall ureteroscope design [77-78]. The ultimate objective of this project is to sufficiently reduce the ureteroscope diameter to allow for in-office procedures without the need of a standard operating room suite. Performing procedures in an outpatient office based setting would simplify scheduling of procedures. Patients would also experience more immediate onsite treatment, shorter facility stays, and less administrative coordination with a hospital, thus significantly reducing support staff time and cost to both parties. Current routine, uncomplicated outpatient ureteroscopic stone removal procedures using laser lithotripsy result in costs averaging ~ $25,000. Conservative estimates suggest that these costs could be reduced by up to 80%, simply by performing the procedure in an office-based setting.

Typical candidates for this procedure would have a small to moderate sized stone (2-7 mm diameter) lodged in the lower ureter. Such an event accounts for approximately 40-50% of patients presenting with ureteral stones. More proximal stones, larger stones or stones within the kidney would require more conventional actively flexible ureteroscopes and complex manipulation and are therefore not the focus of this study. Procedures

would potentially be performed in an office setting under moderate to deep sedation, which is quickly reversible, again saving cost, time and improving safety.

Current ureteroscopes used in the clinic often feature only a single working channel for ureteroscopic tool insertion and saline irrigation. However, there is evidence that suggests that a dedicated irrigation channel, separate to that of the primary working channel for device insertion, yields an increased rate of irrigation over comparable cross-sectional size, single channel design [57, 79]. Dual-channel ureteroscopes (Cobra, Richard Wolf, Vernon Hills, IL) are commercially available and have been tested in the clinic, motivating the movement toward multiple channels [80]. It is therefore a logical next step to introduce more dedicated channels beyond irrigation, for different ureteroscopy tools as well (e.g. optical fibers, guide-wires, and stone baskets). Further studies have demonstrated the efficacy of miniaturized ureteroscopes in office based procedures [81].

This study describes the design, characterization, and preliminary testing of novel miniaturized ureteroscope tips for potential use in Thulium fiber laser (TFL) lithotripsy performed in an office-based setting.

6.1.2 Methods

6.1.2.1 Prototype Miniature Ureteroscope Tip Design

A first generation prototype ureteroscope tip was constructed (Figure 6.1) out of translucent amber polyimide tubing (Amazon Supply, Small Parts), housing five cylindrical channels: a 200-µm-ID central channel for small fiber insertion and four surrounding working channels each with 510-µm-ID for instrumentation, irrigation, imaging, and illumination, respectively. These individual channels were then enclosed within another 4.35 Fr (1.45-mm-ID) / 4.5 Fr (1.51-mm OD) polyimide sheath.

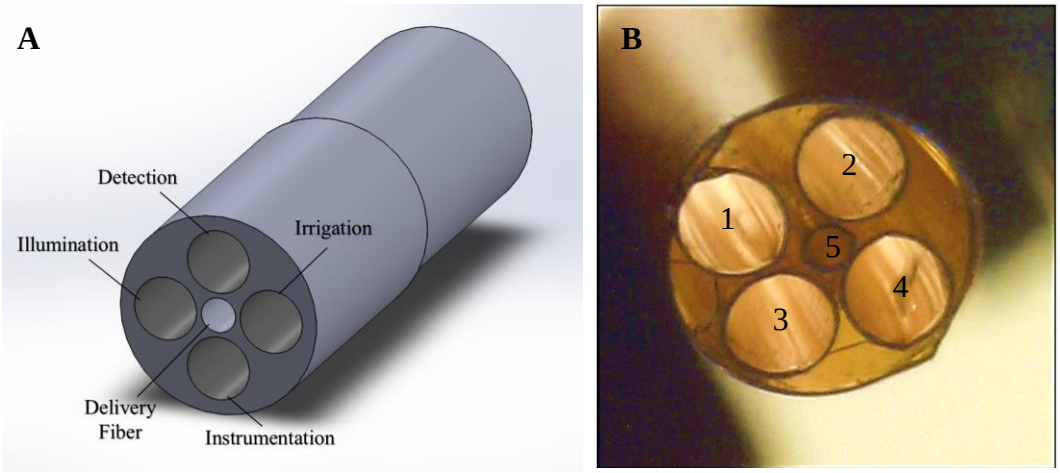

Figure 6.1: (A) Diagram and (B) photograph of miniaturized, 4.5 Fr (1.51-mm-OD) ureteroscope tip with five channels: (1) Illumination, (2) Detection, (3) Guidewire/stone basket, (4) Irrigation, and (5) Optical fiber.

6.1.2.2 Instrument Insertion

Passage of a small optical fiber (100-µm core, 170-µm-OD, Polymicro, Phoenix, AZ) through a 200-µm inner diameter central channel may free up valuable space that could be used to either decrease tip outer diameter or provide more room for larger diameter working channels while still within the desired outer diameter range of 5 Fr (1.67 mm).

The TFL lithotripter allows use of smaller optical fibers compared to the conventional Holmium:YAG laser lithotripter. Hydrophilic guide wires are used to facilitate passage of ureteroscopes into difficult to reach anatomical locations such as the ureter. Guide wire insertion was successfully conducted with a 450-µm-OD (0.018 in) diameter hydrophilic guide (Terumo, Somerset, NJ) through one of the instrumentation working channels. A 1.3 Fr (450-µm-OD) stone basket (Optiflex Nitinol Stone Retrieval Basket, Boston Scientific, Marlborough, MA) was also successfully inserted through a working channel (Figure 6.2).

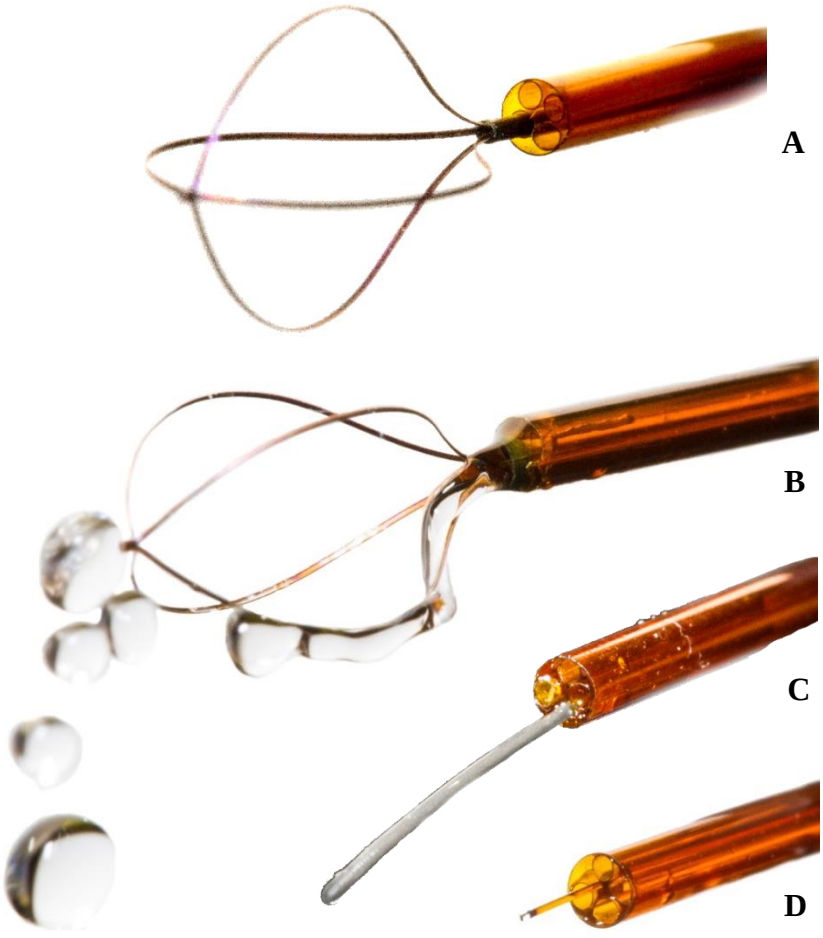

Figure 6.2: Miniaturized ureteroscope tip with device demonstrations: (A) 1.3 Fr stone basket insertion (B) Stone basket insertion with saline flow (C) Guidewire insertion (D) 100-µm-core (170-µm-OD) delivery fiber insertion through central channel.

6.1.2.3 Prototype Testing – *In Vitro* Imaging

A 0.4 mm, 3,000 pixel, commercially available borescope (Milliscope II Fiber Scope, Advanced Inspection Technologies, Melbourne, FL) was selected for initial imaging testing for our prototype. The Milliscope II provides a 55º field of view, 8 mm bending radius, and 4-10 mm adjustable depth of field. A 50 Watt LED light source (LLS-050, Advanced Inspection Technologies, Melbourne, FL), was used in conjunction with the borescope for illumination.

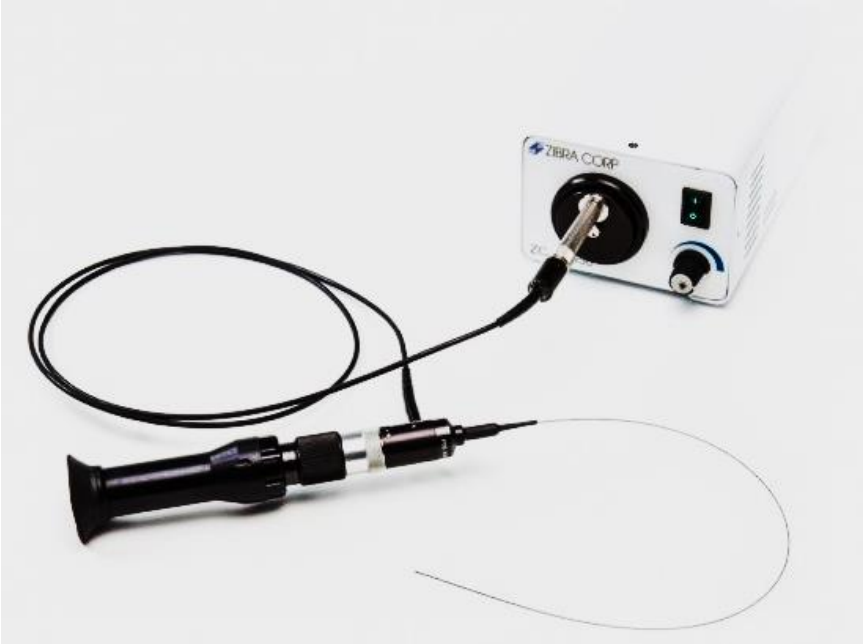

Figure 6.3: Miniature Borescope (Milliscope II) with 50W LED light source setup for 3,000 pixel imaging tests.

Fresh porcine ureters obtained from a slaughterhouse (Animal Technologies, Tyler, TX) were sectioned into ~ 7 cm long samples to serve as a representative model to simulate in vivo imaging through the ureteroscope prototype. The ureter tissue was kept hydrated in saline in preparation for the studies, and then individual ureter samples were

gently compressed between a v-grooved optics mount and a tension pin above. The distal end of the ureter was clamped with sufficient force to prevent light from entering the opening. The sample was submerged in a saline bath to hydrate tissue samples during studies as well as to simulate in vivo conditions. Uric acid (UA), calcium oxalate monohydrate (COM) with > 95% purity, calcium oxalate dihydrate (COD), and 60% calcium oxalate monohydrate / 40% calcium phosphate (CaP) stone samples were chosen as representative common stones [35], then placed in porcine ureters submerged in saline for image testing (Figure 6.4).

Figure 6.4: Representative kidney stones used in borescope resolution comparison. From left to right: COM, COD, UA, CaP.

6.1.2.4 Comparison of Miniature Borescopes

The 6k and 10k pixel flexible fiber optic endoscopes (Myelotec, Roswell, GA) were selected for image quality comparison (Table 6.1). The endoscopes, too large for insertion through the prototype working channels were operated freely by an experienced urologist in vitro in clamped tygon tubing submerged in a saline bath. The United States Air Force resolution test was used to compare images acquired through borescopes of 3k, 6k, and 10k pixels at working distances from 1 - 5 mm, typically used in the clinic

(Figure 6.5). Each miniature borescope was aligned to image quadrant (-2, 3), which was printed at ~ 1.75 lp/mm (line pairs per mm).

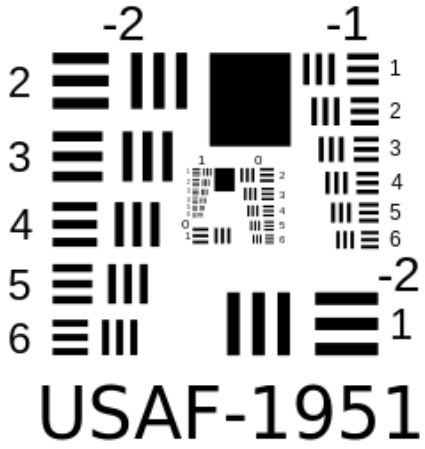

Figure 6.5: 1951 USAF resolution test chart used for standardized borescope imaging comparison.

Table 6.1: Comparative Borescope Standard Specifications.

Pixel Count	3,000	6,000	10,000
FOV	55º	65º	70º
Working Distance (mm)	4 - 10	3 – 12	3 - 15
OD (mm)	0.4	0.6	0.9
Bend Radius (mm)	8	15	10

6.1.3 Results

Borescope calibration results using an USAF resolution test chart are shown below for the three miniature borescopes tested (3k, 6k, and 10k pixels) (Figure 6.6).

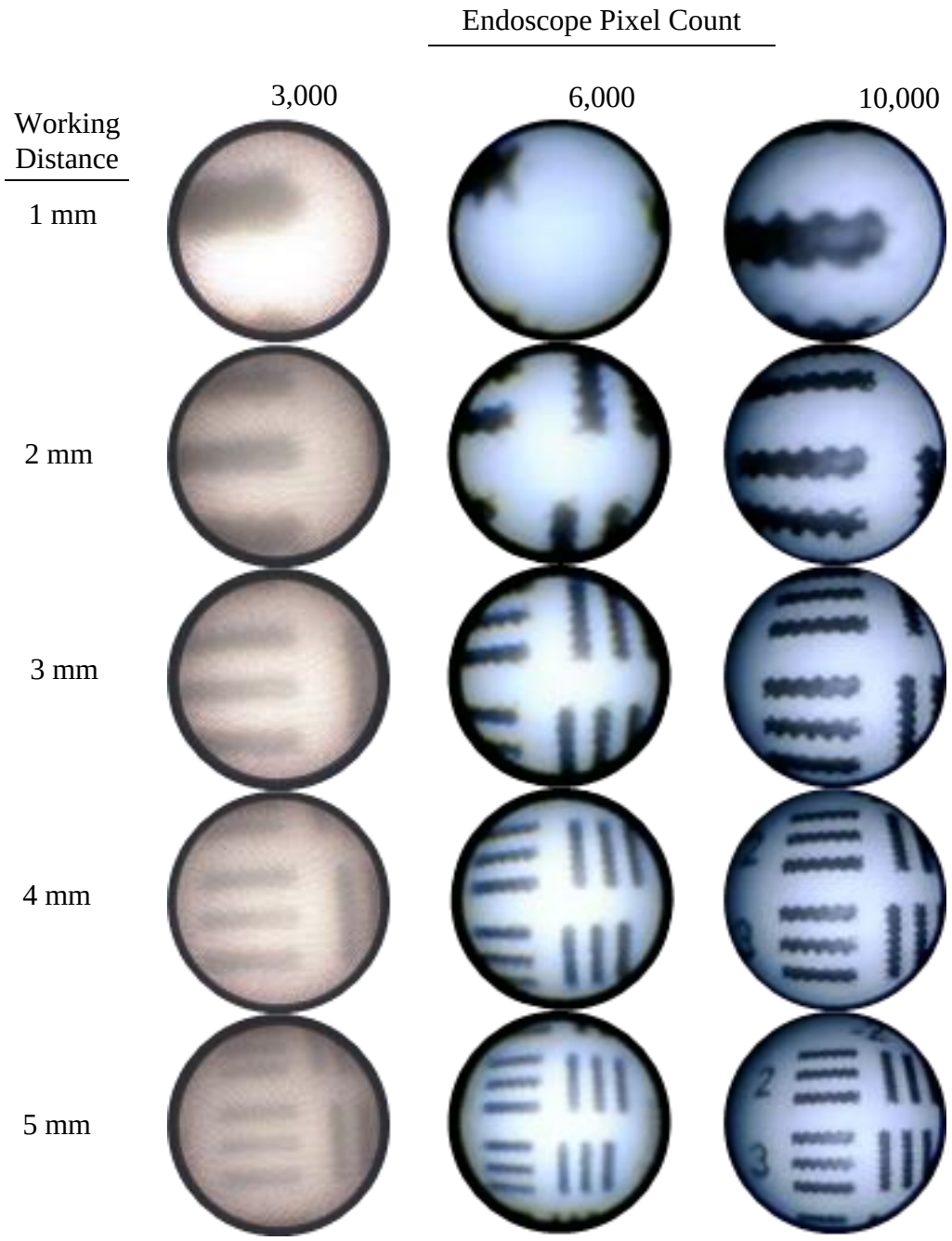

Figure 6.6: *In Vitro* image quality comparison of 3k, 6k, and 10k pixel borescopes (left to right) using the 1951 USAF resolution test chart. Pictured working distances range from 1 - 5 mm.

An *in vitro* porcine ureter model was also used to demonstrate image contrast between four different common urinary stone types (COM, COD, UA, CaP) and the ureter for each of the miniature borescopes (Figure 6.7).

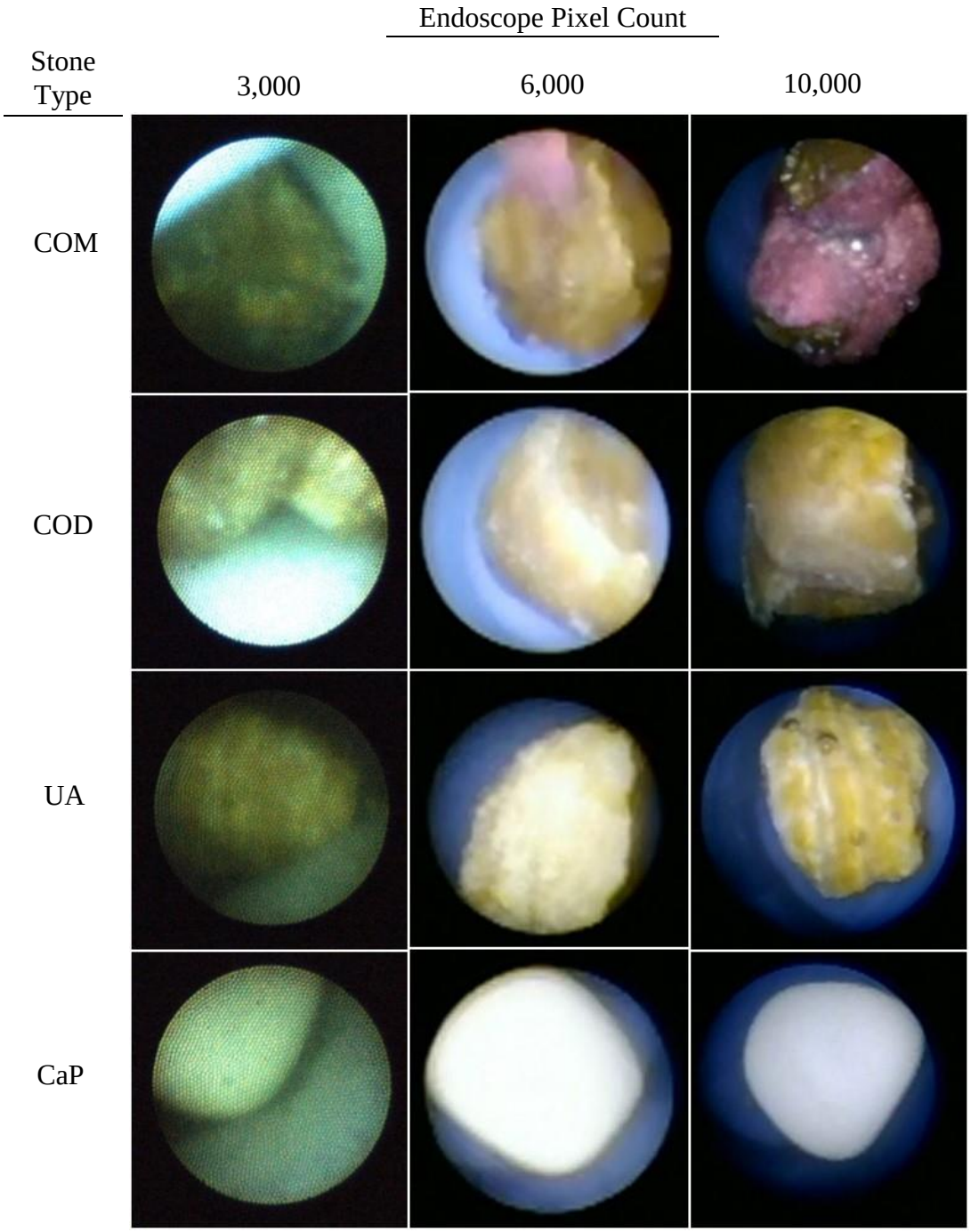

Figure 6.7: *In Vitro* image quality comparison of COM, COD, UA, and CaP stones (top to bottom) with 3k, 6k, and 10k pixel borescopes (left to right).

Image comparison demonstrated the 3k pixel borescope to be a workable option. However, both 6k and 10k pixel borescopes outperformed their lesser counterpart, as expected. The 6k pixel borescope, having an outer diameter of 0.6 mm would be a viable candidate with minor alterations to the prototype endoscope tip geometry. For example, incremental expansion of the working channel from 510 µm to 600 µm would allow for use of this borescope.

6.1.4 Discussion

The TFL fiber has an inherently small cross-sectional area, thereby increasing the saline flow rate through a standard 1.2 mm diameter working channel compared with the standard Holmium 270-μm-core fiber. As a result, such a large working channel may be unnecessary during TFL lithotripsy. In our novel, five channel prototype ureteroscope tip design, every instrument as well as irrigation flow has a dedicated channel. The significant decrease in the inner diameter of the four channels, from 1.2-mm to 0.51-mm, also results in a greater than desired decrease in the flow rate, by almost an order of magnitude (31.3 ± 0.6 vs. 3.9 ± 0.2 ml/min). However, this decrease in irrigation rate can be compensated for by the addition of manual pump-assisted irrigation, which yielded 37.9 ± 10.5 ml/min during preliminary laboratory testing. If current prototype dimensions were left unchanged, such a proximal pumping mechanism would need to be integrated into the final ureteroscope tip design to provide suitable visibility and safety during laser lithotripsy.

As design iterations have progressed, we have strived to combine certain optical elements, for example, coupling illumination with imaging as seen in industrial borescopes and endoscopes, and/or fiber integration with the stone basket, which may free up cross-sectional area in the ureteroscope geometry as well as render obsolete the high number of ports in the five channel design. These advances may allow construction of a 2nd generation prototype incorporating fewer working channels, thus reclaiming some of the unused space in between channels in the previous design, for either increased irrigation or further miniaturization. Similarly, since we have demonstrated the feasibility of a less than 5 Fr design, the working channels may be redesigned with

altered arrangements, diameters, and geometries within the same total area “footprint”, for desired functionality. Enlarging one of the 510 µm working channels to 600 µm in order to accommodate the diameter of the 6k pixel integrated scope is one such possibility that has been considered. In this case, since illumination is integrated into the borescope, a dedicated illumination working channel could be removed, freeing up another 510 µm of usable area. As subsequent prototypes become more sophisticated, the polyimide tubing model may be replaced with a more robust prototype material such as machined steel or printed metal castings to more closely resemble a commercial ureteroscope tip.

6.1.5 Conclusions

A prototype, 4.5 Fr (1.5-mm-OD) ureteroscope tip was developed, housing a 200-µm-ID central channel for insertion of small fibers and four surrounding channels, each with 510-µm-ID for instrumentation, irrigation, imaging, and illumination. Optical fibers, guidewires, and stone baskets were successfully inserted through the prototype's working channels to demonstrate feasibility. Low irrigation rates were measured, due to the smaller working channels, requiring manual pump-assisted irrigation during potential clinical use. Imaging was performed with 3k, 6k, and 10k pixel miniature flexible borescopes with outer diameters of 0.4, 0.6, and 0.9 mm, respectively. The 3k pixel borescope with integrated illumination, successfully differentiated between COM, COD, UA, and CaP urinary stones and the ureter wall, critical for visibility and safety during potential clinical use. However, the 6k pixel borescope provided improved image quality with only slightly larger outer diameter. The miniaturized ureteroscope tip and borescope combination has potential to eliminate need for full anesthesia and dilation, increase comfort and safety of laser lithotripsy via ureteroscopy, and significantly reduce hospital costs via an office based procedure.

6.2 Rapid Prototyping

6.2.1 Additive Manufacturing

One key hindrance to research and design is fabrication cost and time. From idea, to design, to rendering, the process flows virtually unencumbered by physical constraints, but can be easily halted by outsourced manufacturing which can take weeks to produce a prototype that may not function as desired; at which point the process must start over again. One enabling technology which allows us to combat this stagnation is additive manufacturing, or 3D printing.

While a number of 3D printing techniques exist, cost of both printer and materials, minimum wall thickness/hole diameter capabilities, and in-house availability played a crucial role in our printing process selection. Two techniques were selected for initial testing, fused deposition modeling (FDM) and stereolithography (SLA). These techniques were chosen for print speed and choice, color, and cost of the materials.

Both processes began with a design and rendering in Solidworks, a form of computer aided design (CAD) software, and were converted into each printer's proprietary modeling program which allows them to determine support structures, print path, and print time.

FDM vs SLA

In fused deposition modeling the part is produced by extruding a continuous bead of thermoplastic filament which is heated in an extrusion nozzle head and deposited at a predetermined speed and path, allowing the plastic to harden nearly immediately as successive layers are deposited on top of the previous layer, similar to a glue gun. Servo

motors and microcontrollers are often employed to move the extrusion head in 3 axes of motion.

One limitation of FDM is the resolution at which the nozzle is able to deposit filament. While a machine may boast certain layer and feature thicknesses, the finished product may vary greatly. After one layer has been printed, the following layer may begin to print before the initial layer has cooled, allowing the piece to “bleed” and in extreme cases, causing the print to lift from the print bed entirely.

During SLA additive manufacturing, the part is built via curing liquid resin with a UV laser. Specifically, we used the Formlabs Form 1+ tabletop SLA 3D printer (Cambridge, MA), which incorporates a high precision, galvanometer driven, optical system that guides a 405 nm, 120 mW laser across a tank of liquid resin, solidifying layers as thin as 25 microns as the build platform pulls the part upwards, out of the tank. [82].

One limitation of SLA is that the choice of resin dictates the final print resolution because optical properties of the resin play a role. White or clear resin allows the user to better visualize inner geometry, however this also allows the laser to penetrate into and cure excess resin onto the surface of the previously cured part, lowering the effective resolution, filling holes and adding to wall thickness. More absorptive black resin can be substituted which makes processing harder to visualize, but prevents stray laser curing, producing finer detail parts than clear or white resin. Furthermore, since the laser beam must propagate through the print bed into the resin vat, it is important that its surface is pristine. Scratches and blemishes in the bed cause cascading print defects and misprints, rendering the resulting pieces useless.

While both printing techniques were at our disposal, only one provided the precision results needed for meticulous and uniform manufacturing. Stereolithography delivered beautiful, functional parts that the plastic extrusion printer was unable to perform.

6.2.2 3D Printed Prototypes

FDM vs SLA 4/5 Channel Design

Initial prototype designs contained four working channels. However, since it was observed that a small fiber might fit through the center tubular hole formed by their arrangement, a five channel tip design proved a possibility. Both 4 and 5 channel designs proved impossible to produce via tabletop 3D printing because the aspect ratio of feature size proved to be beyond their resolution limits. After this realization, the polyamide prototype was constructed as proof of concept.

2nd Generation Design

A 2nd generation design was adapted to incorperate a detection and ring illumination dedicated port that could fit a currently available 6,000 pixel imaging borescope, allowing for future integration of our own imaging system. This generation further combined remaining ports into a single channel for irrigation similar to the previous design with the alteration of making the single working channel a rounded hemispherical passage in an attempt to eliminate wasted space between channels.

Due to limitations of the printing process, the diameter of the printed tip was scaled up to a 6 Fr (2 mm OD) as opposed to the 1.67 Fr design achieved with polyamide tubing.

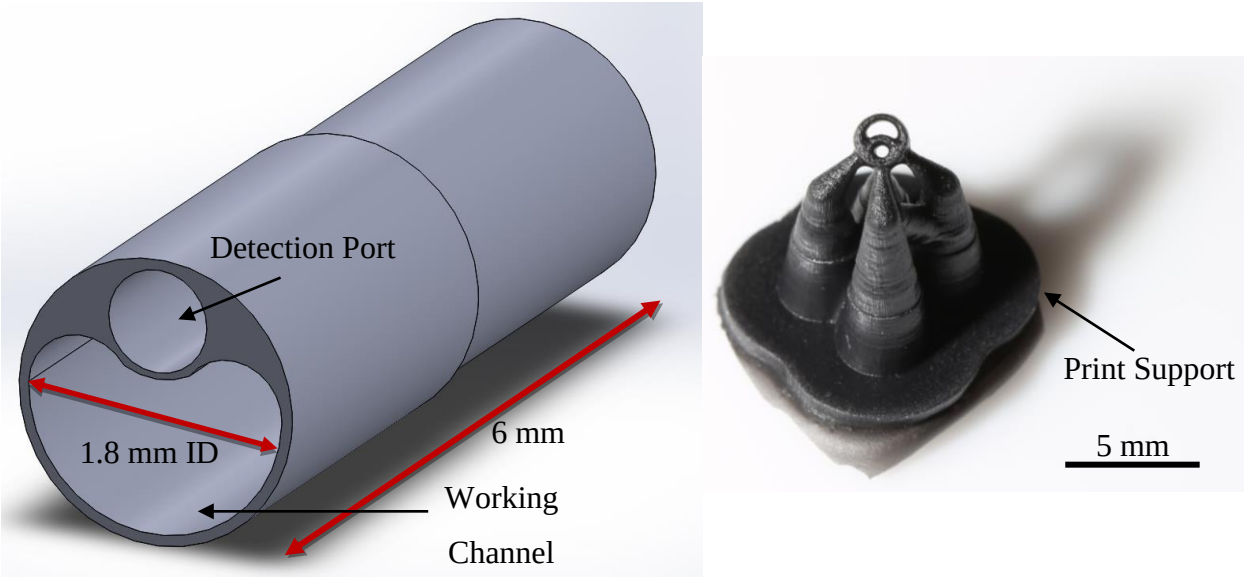

Figure 6.8: Miniaturized ureteroscope tip with two channels: One for illumination and detection, the other for irrigation, guidewire/stone basket, and fiber. (Left) Solidworks rendering. (Right) SLA printed tip on print support raft.

Irrigation Testing

Saline irrigation rates were measured by introducing gravitational flow from a saline bag (at a fixed height of 100 cm) through the 5.4 Fr (1.8 mm) single working channel of the printed prototype tip. Saline flowed freely through the ureteroscope for 2 minutes for each experiment.

Studies were conducted using a combination of different fibers and stone baskets, including experimental 100-µm-core silica fiber (FIP100140170, Polymicro, Phoenix, AZ), clinical 270-µm-core fiber (Holmium Lightguide 270D fiber, Olympus Gyrus ACMI), and 1.3 Fr stone basket (Optiflex Nitinol Stone Retrieval Basket, Boston

Scientific, Natick, MA). Saline volume was then measured with a graduated cylinder. A sample size of n = 3 was performed for each study with the mean ± standard deviation recorded. The percent flow rate was calculated by dividing flow with an instrument inserted by flow through the empty working channel (control) without a fiber or basket present.

Table 6.2: Irrigation rates through the 5.4 Fr (1.8 mm) single working channel of the two channel printed prototype tip.

Instrument	**Flow Rate (ml/min)**	**Flow (%)**
Empty Channel	39.9 ± 1.6	100
Fibers [core/cladding/jacket] OD (µm)		
100/140/170	28.3 ± 0.4	70.9
270/322/464	19.5 ± 0.6	48.9
Stone Basket		
1.3 Fr (433 µm)	18.7 ± 0.7	46.9

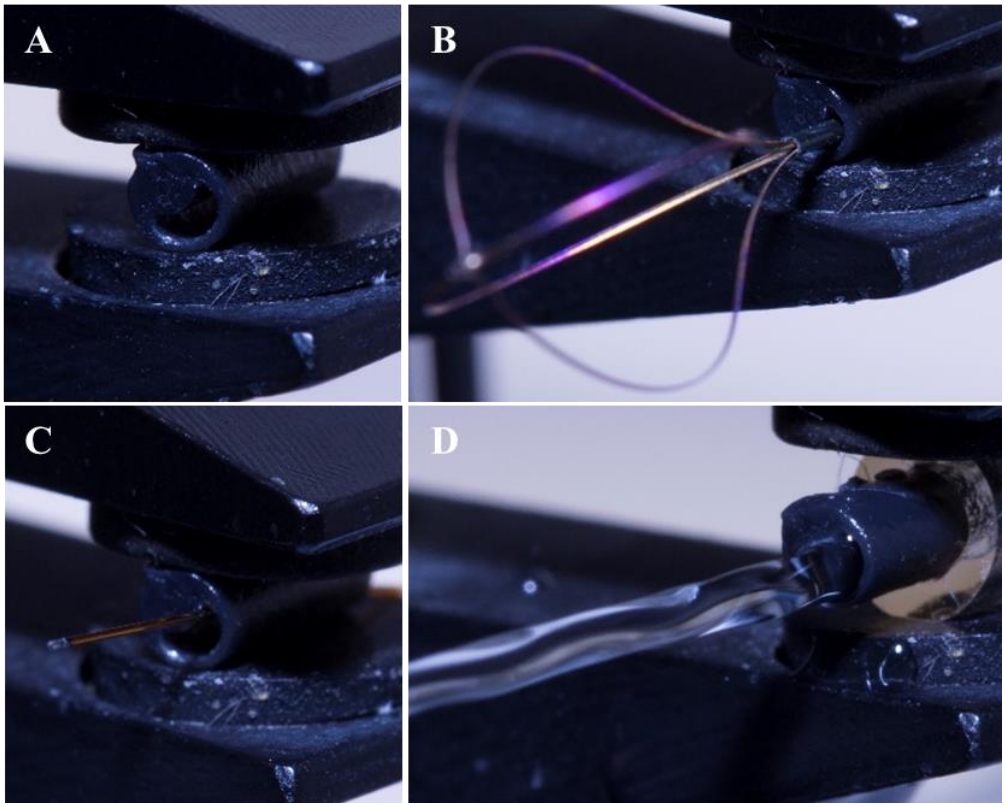

Figure 6.9: Miniaturized 6-Fr-OD (2 mm) ureteroscope tip with device demonstrations: (A) Prototype alone (B) 1.3 Fr stone basket insertion (C) 100-µm-core (170-µm-OD) delivery fiber insertion (D) Saline gravity flow from standard 1 m height.

Table 6.2: Comparison of irrigation rates through the 3.6 Fr (1.2 mm), 1.5 Fr (0.51 mm), and 5.4 Fr (1.8 mm) working channels of the standard and prototype tips with open channel and various instruments based off of the standard scope.

Instrument	**Flow Rate (ml/min)**	**Flow (%)**
Standard 3.6 Fr Scope		
Empty Channel	31.3 ± 0.6	100
Fibers [core/cladding/jacket] OD (µm)		
100/120/140	25.8 ± 0.5	82.4
270/322/464	13.5 ± 0.2	43.1
Stone Baskets		
1.3 Fr (433 µm)	12.6 ± 0.2	40.3
1.9 Fr (633 µm)	6.0 ± 0.1	19.2
5 Channel Prototype		
Empty Channel	3.85 ± 0.15	12.3
3D Printed Prototype		
Empty Channel	39.9 ± 1.6	127.5
Fibers [core/cladding/jacket] OD (µm)		
100/140/170	28.3 ± 0.4	90.4
270/322/464	19.5 ± 0.6	62.3
Stone Basket		
1.3 Fr (433 µm)	18.7 ± 0.7	59.7

When comparing gravitational flow saline irrigation rates for empty standard working channel versus those of our prototypes, it is evident that the 5 channel design is insufficient, even if two ports were utilized for saline flow. However, the SLA printed tip's 1.88 mm hemispherical design surpassed the standard flow rate by an additional 27.5 %. [Table 6.2] Current ureteroscope designs provide minimal irrigation, often slowing to a drip with the introduction of urological tools. Figure 6.9 depicts a steady stream ejected from the tip, making these reported irrigation rates clearly superior.

CHAPTER 7: THULIUM FIBER LASER LITHOTRIPSY USING A MINIATURE BALL-TIP FIBER

7.1 Introduction

7.1.1 Ball Tip Fibers in Laser Medicine

Ball-tip optical fibers have been used in laser medicine since the 1990's, first for laser angioplasty [83,84] and neurosurgery [85], and more recently for endovenous laser therapy [86-89]. Laser angioplasty employs the ball tip design by allowing the quartz fiber to taper from a small core to a larger diameter, smooth, rounded ball tip, thus minimizing the probability of mechanical dissection or perforation of the blood vessel wall. Neurosurgical procedures utilize a carbon coated, "hot" ball tip fiber to absorb light and convert it into heat, thus providing ablative temperatures at low power and increasing safety margins near delicate tissues. Endovenous laser therapy also employs ball tip fibers to prevent fiber induced mechanical perforation of veins.

7.1.2 Holmium:YAG Laser Lithotripsy using Ball Tip Fibers

In a similar approach, use of ball tip fibers during laser lithotripsy is motivated by the desire to prevent fiber induced mechanical damage to the inner lining of the ureteroscope working channel and potential perforation of the ureter wall as well. Damage to the working channel is of great concern to patient safety and of further concern to clinicians, since instrument repair is costly, with single ureteroscope average repair costs ranging from $4,500 to $13,200 [6,90]. Damage may occur from both fiber insertion through the

working channel during ureteroscope deflection, as well as premature laser activation with the fiber still inside the ureteroscope.

Several devices have been introduced to reduce the probability of ureteroscope damage in both situations, such as the Endoscope Protection System (EPS) [91], which employs an optical sensor that shuts off the laser if the distal fiber tip is still inside the ureteroscope working channel, and Flexguard [92], a protective fiber sheath that insulates the fiber from the ureteroscope. While both of these solutions address laser induced damage, only the Flexguard sheath additionally prevents mechanical damage. However, the trade-off for a protected working channel is a decrease in ureteroscope deflection capability and saline irrigation rates needed for visibility and safety, due to the size of the sheath and the additional space that it consumes within the working channel. While laser induced damage to the inner lining of the ureteroscope working channel constitutes a majority of ureteroscope failures [93], mechanical damage also contributes to ureteroscope failure, and is typically caused by the sharp-edged distal tip of the laser fiber [94].

A ball tip fiber for use in Holmium:YAG laser lithotripsy was recently introduced (Flexiva TracTip 200, Boston Scientific, Marlborough, MA) in the form of a 240-µm-core fiber with 450-µm-diameter ball tip, to address these concerns [95-101]. Ball-tip fibers provide an additional safety margin by allowing for simplified advancement through the ureteroscope working channel without unnecessarily bulking up the working channel wall itself through use of a protective sheath, which would otherwise translate into further loss of ureteroscope deflection and irrigation. The ball tip also prevents chipping of the distal fiber tip during laser lithotripsy, which could otherwise result in

angled, side-firing laser irradiation and thermally induced damage to the ureter wall, as previously reported [102].

7.1.3 Thulium Fiber Laser Lithotripsy using Ball Tip Fibers

Ball tip fibers have not yet been tested using small fibers (< 200-µm-core) unique to the Thulium fiber laser (TFL) for lithotripsy. Their potential advantages are three-fold: (1) the ball geometry may provide a beam waist with higher power density in front of the fiber, increasing stone ablation rates; (2) the rounded surface may reduce fiber tip burn-back by allowing stone fragments to deflect off the tip without causing fiber tip degradation; (3) the smooth surface may enable atraumatic tracking of the fiber through the ureteroscope, thus preventing damage to the lumen of the working channel during fiber advancement while under ureteroscope deflection. Extensive simulations describing the beam characteristics of ball tip fibers immersed in both air and water mediums have been previously reported in detail for other applications [103].

Conventional bare tip fibers suffer from damage in the form of distal fiber tip "burn-back" during TFL lithotripsy, attributed to excessive temperatures and mechanical stress caused during stone fragmentation, as well as pressures generated during implosion of the cavitation bubble at the fiber tip [54]. Such degradation in the clinic may result in the costly disposal of the fiber either during or after the procedure is completed. Previous studies have been conducted to demonstrate the TFL's ability to spare the proximal fiber tip during lithotripsy [104]. Multiple studies have also attempted to reduce distal fiber tip degradation through the use of hollow steel tips [54], tapered fiber tips [18], detachable fiber tips [55], and now ball-tip fibers in this study.

The TFL near-single-mode, Gaussian spatial beam profile also allows higher laser power to couple into smaller fibers (e.g. 50 and 100-µm-core) than used for Holmium laser lithotripsy. For difficult laser lithotripsy procedures requiring extreme flexion of the ureteroscope (e.g. in lower pole of the kidney), a smaller fiber permits greater ureteroscope flexibility. The smaller fiber also allows increased irrigation through the small (1.2-mm-ID) ureteroscope working channel, which should translate into improved visibility and safety [18,17,19].

The ball tip geometry eliminates the possibility of mechanical damage observed with use of conventional traumatic flat fiber end faces, and allows for unperturbed insertion through the ureteroscope. Therefore, a 100-µm-core silica trunk fiber with 300-µm-diameter distal ball tip is tested, combining general properties of ball tip fiber with small fiber design for TFL lithotripsy.

7.2 Methods

7.2.1 Thulium Fiber Laser Parameters

A 100-Watt, continuous-wave, Thulium fiber laser (TLR 100-1908, IPG Photonics, Oxford, MA) with a center wavelength of 1908 nm was used in these studies. A 25-mm-focal-length, plano-convex lens was used to focus the 5.5-mm-diameter fiber laser beam from the built-in collimator to a spot diameter of ~ 25 μm ($1/e^2$) for coupling into a separate 100-μm-core, low-OH, silica optical fiber with 300-μm-diameter ball tip (FIPE100140170/2M Ball Lens, Polymicro, Phoenix, AZ). The protective jacket at the distal end of the trunk fiber was stripped back, exposing the cladding for a short length of 2 mm near the ball tip. The laser was electronically modulated with a function generator (DS345, Stanford Research Systems, Sunnyvale, CA) to produce pulse energy of 35 mJ, pulse duration of 500 μs, and pulse rate of 300 Hz, selected based on optimal results from previous studies [24].

7.2.2 Ball-Tip Fiber

There are several methods for fashioning ball-tip fibers. Below, we mention one possible method to form the ball-tip on a bare fiber in which the fiber is melted and the "ball" drawn from the core and cladding. This is accomplished by:

1. Mounting an optical fiber on a lathe;
2. Heating the optical fiber to a sufficient temperature to cause the fiber to begin to melt while turning the lathe at a high speed to provide uniform heating;
3. Continuing the heating for a long enough period to cause the natural surface tension to expand the diameter of the optical fiber;

4. Moving the source of heat along the longitudinal axis of the optical fiber to form the desired taper shape and length;
5. Heating of the taper end of the optical fiber to form a round end portion of the desired diameter [105].

7.2.3 Kidney Stone Samples

All kidney stone samples were composed of 60% calcium oxalate monohydrate and 40% calcium phosphate (Figure 7.1b). These stones were chosen because calcium oxalate stones comprise about 80% of all stone compositions encountered in the clinic [35]. The stone samples were obtained from a single source and had a consistent mass (50 to 80 mg), size (4 to 5-mm diameter), shape, and color. Stone samples were desiccated in an oven at a constant temperature of 70 °C for a time of 15 min and then weighed with an analytical balance (Model AB54-S, Mettler-Toledo, Columbus, Ohio) before lithotripsy experiments to determine their initial mass. The stone samples were then placed in a wire mesh cradle and immersed in a saline bath. TFL lithotripsy experiments were conducted after a rehydration time of 1 min, using a handheld ball-tip fiber. Stone ablation rate was calculated by dividing stone mass by laser operation time. A minimum of ten stone samples were used for each study group (bare fiber and ball-tip fiber configurations). For data analysis, “Single Use” referred to data obtained from the optical fiber during its initial ablation of each stone sample. “Multiple Use” referred to data obtained from the same ball tip fiber used in multiple stone sample studies. The distinction arises because fibers not showing evidence of distal tip damage or degradation during a study were re-used to determine their maximum number of uses until fiber failure.

7.2.4 Experimental Setup

A 1.5 mm mesh sieve was integrated into a 70 mm diameter, 150 mL transparent plastic sample container, and bowed in a concave orientation while remaining level at the conic epicenter (Figure 7.1). Kidney stones were submerged in a saline bath and placed in the center of the sieve curvature. All stone samples were free to move inside the sieve cone during the studies. The fiber was held manually in contact with the stone samples during the entire study, and only repositioned to target fragments that were displaced during irradiation. Stone samples were irradiated until all ablated fragments were sufficiently small (< 1.5 mm diameter) to pass through the mesh sieve. Laser fragmentation times were recorded for each experiment, which were equivalent to total procedure times, since significant stone retropulsion was not observed and repositioning of the fiber to treat individual stone fragments was minimal.

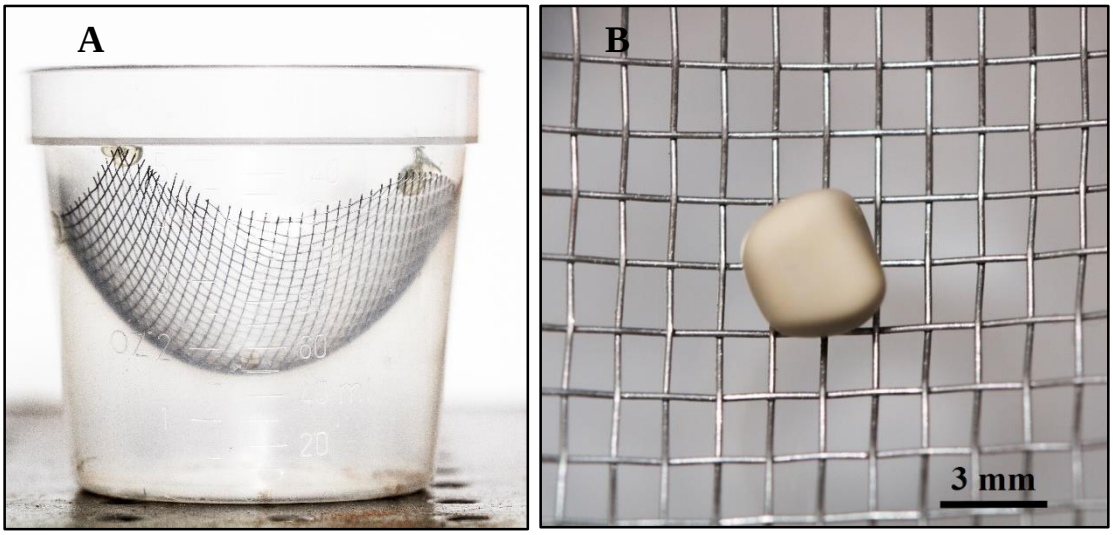

Figure 7.1: (A) Experimental setup for TFL lithotripsy, and a 1.5 mm mesh sieve integrated into 150 mL transparent plastic sample container, filled with saline. (B) 60 % COM / 40 % $CaPO_4$ kidney stone resting on mesh sieve.

Damage inspection of the ball tip fiber was conducted using a CCD camera (DCC1645C, Thorlabs, Newton, NJ) to record images before and after fiber use (Figure 7.2). Undamaged fibers were re-used for another stone sample ablation study. Degraded fibers had their ball tip clipped and the fiber re-polished for direct comparison as bare tip fiber control studies.

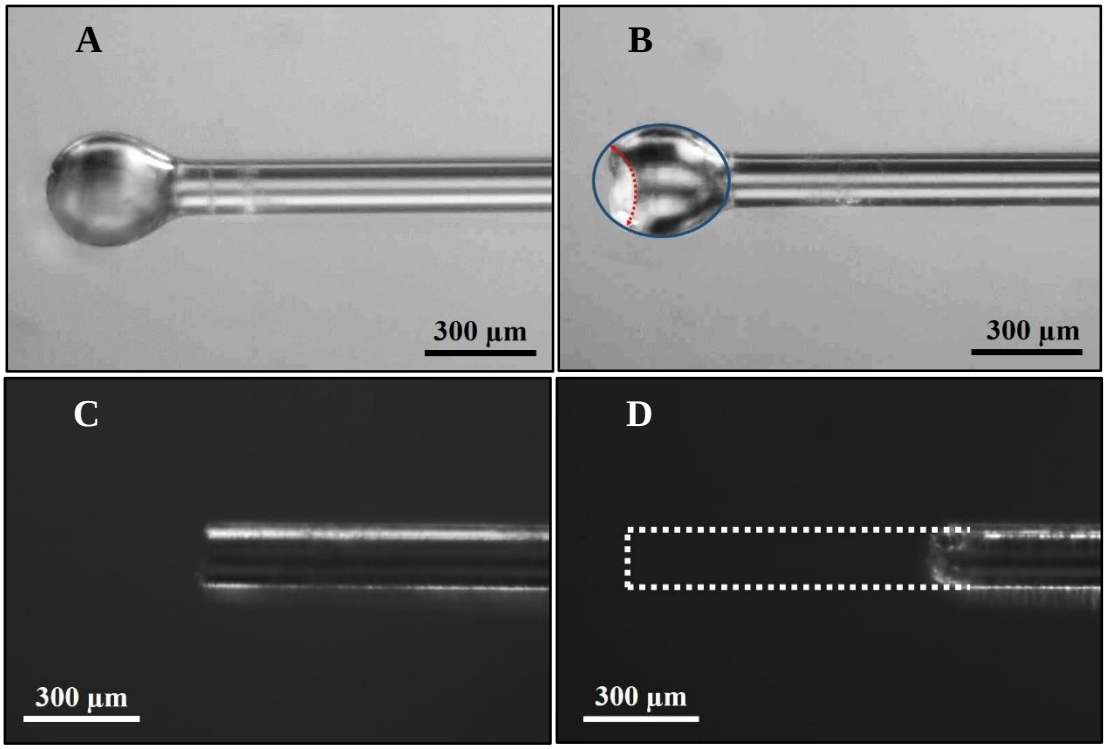

Figure 7.2: (A) Ball tip fiber prior to TFL lithotripsy. (B) Degraded ball tip fiber after TFL lithotripsy, with ~ 100 µm of burn-back. (35 mJ, 500 µs, 300 Hz, ~ 16,500 pulses, 55 s) (C) Control fiber prior to TFL lithotripsy. (D) Degraded control fiber tip after TFL lithotripsy, measuring ~ 1 mm of burn-back represented by the dotted line. (35 mJ, 500 µs, 300 Hz, ~ 12,000 pulses, t = 40 s)

7.2.4 Ureteroscope Irrigation Rate Studies

Saline irrigation rates were measured by introducing gravitational flow from a saline bag (at a fixed height of 100 cm) through the 3.6 Fr (1.2 mm) working channel of a flexible ureteroscope (Uretero-Reno Videoscope URF-V, Olympus, Southborough, MA).

Saline flowed freely through the ureteroscope for two minutes for each experiment. Studies were conducted using the same 100-μm-core fiber with 300-μm-diameter ball tip inserted through the working channel. Saline irrigation volume was then measured with a graduated cylinder. A sample size of n = 4 was performed with the mean ± standard deviation recorded. Percent flow rate was calculated by dividing flow with a fiber inserted by flow through the empty working channel (control) without a fiber present.

7.2.5 Ureteroscope Deflection Tests

The same flexible ureteroscope described above was also used to perform primary (forward) and secondary (backward) deflection tests both with and without the ball tip fiber inserted through the working channel. The maximally flexed ureteroscope configurations were then photographed, and a protractor used to measure the maximum deflection angle.

7.2.6 Cavitation Bubble Studies

The TFL operating at 1908 nm with 35 mJ pulse energy, 500 μs pulse duration, and 300 Hz pulse rate delivered laser energy through the 100-μm-core, silica ball tip fiber. The fiber tip was submerged in a saline bath, either by itself, or in contact with a kidney stone sample. Cavitation bubble dynamics using both bare and ball tip fibers were recorded. Imaging was performed using a high speed camera (SA5, Photron, Tokyo, Japan) at 105,000 frames per second and with 10 μm spatial resolution.

7.3 Results

7.3.1 Stone Ablation Rates

Stone samples were irradiated until all ablated fragments were sufficiently small (< 1.5 mm diameter) to pass through the mesh sieve, in accordance with acceptable clinical criteria for stone fragment size. Figure 7.3 shows a stone prior to TFL lithotripsy and stone debris after experiments. Ball tip fibers produced a sizeable amount of residual dust in addition to traditional larger fragments. This may be attributed to the lensing effect evidenced by the caustic formation of the modeled laser output beam emanating from the ball tip. (Figure 7.4)

Figure 7.3: Human urinary stone with remaining stone dust from single ball tip fiber study with 3 urinary stone samples.

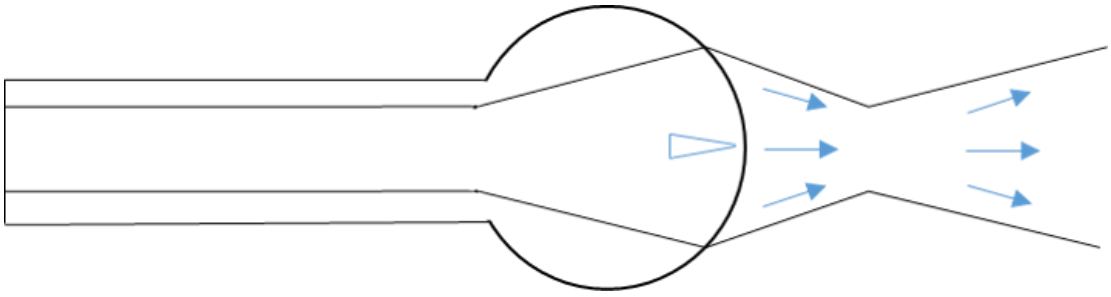

Figure 7.4: Ball-tip fiber output diagram.

Table 7.1: TFL stone ablation rates (mg/s) and total operation times (s) to fragment 4 to 5 mm diameter calcium oxalate stones into fragments smaller than 1.5 mm.

	100-µm Ball Tip Fiber		**100-µm Bare Tip Fiber**
	Single Use	Multiple Use	Single Use
Ablation Rate (mg/s):	1.3 ± 0.4	1.3 ± 0.5	1.3 ± 0.2
Operation Time (s):	61 ± 21	55 ± 24	54 ± 9
Stone Mass (mg):	73 ± 13	66 ± 13	71 ± 6
Number of Samples (N):	10	44	10

Measured laser operation times and calculated stone ablation rates during TFL lithotripsy experiments using ball tip and bare tip fibers (control) are summarized in Table 7.1. Initial stone mass was similar for all data sets and measured 73 ± 13, 66 ± 13, and 71 ± 6 mg for single-use ball tip, multiple-use ball tip, and bare tip fiber control studies, respectively ($P > 0.05$). Operation times were recorded and measured 61 ± 21, 55 ± 24, and 54 ± 9 s for each group ($P > 0.05$). There was no statistical difference ($P > 0.05$) between stone ablation rates for single-use ball tip fiber (1.3 ± 0.4 mg/s), multiple-use ball tip fiber (1.3 ± 0.5 mg/s), and conventional single-use bare tip fibers (1.3 ± 0.2 mg/s). The TFL with a low pulse energy and high pulse rate produced a vibrational effect, which led to the stone oscillating in the same relative position, only requiring local pursuit of the stone within a few millimeters of the initial stone location. It should be noted, however, that the presence of the sieve may have distorted to some degree the normal retropulsion movement typically encountered in the clinic.

Ball tip fibers found to be undamaged after single use were re-used for ablation of multiple samples. This process continued for each ball tip until it showed significant degradation and diminished energy output, evidenced by a sharp increase in operation time and a corresponding sharp decrease in stone ablation rate. Only then were the ball

tips clipped and bare fiber tip re-polished for use in control studies. First time use of samples was noted for each fiber as well as number of succeeding samples tested (Table 7.2).

Table 7.2: Number of samples successfully fragmented by each ball-tip fiber.

Fiber # Treated	**#Samples**
1	1
2	3
3	9
4	2
5	3
6	2
7	2
8	14
9	4
10	4
Average	**4.4**
S.D.	**3.8**

7.3.2 Saline Irrigation Rates

Saline irrigation flow rates through the ureteroscope working channel with and without the insertion of the 100-μm-core/140-μm-cladding/170-μm-buffer trunk fiber and 300-μm-diameter ball tip fiber yielded values of 23.0 ± 0.8 and 27.7 ± 1.0 ml/min, respectively. This translated into an 83% flow rate with the ball tip fiber present. These values are consistent with measurements reported during previous studies testing a wider range of both smaller and larger fibers, and the 83% flow rate with ball tip fiber is significantly higher than the 43% flow rate using a standard 270-μm-core Holmium fiber [18,19,106].

7.3.3 Ureteroscope Bending Studies

Figure 7.5 shows the influence of the ball tip fiber on deflection of a flexible ureteroscope. Primary (forward) deflection with and without fiber inserted measured 267 and 268 degrees, respectively. Secondary (backward) deflection with and without fiber inserted measured 169 and 170 degrees, respectively. These values are within the error for measurement and show that the ball tip fiber did not significantly impede ureteroscope deflection. Previous studies have reported that maximum deflection of this specific ureteroscope decreased from 275 to 217 degrees (primary) and 180 to 161 degrees (secondary) simply with prolonged clinical use [60], so the small changes in deflection angles measured in this study are insignificant.

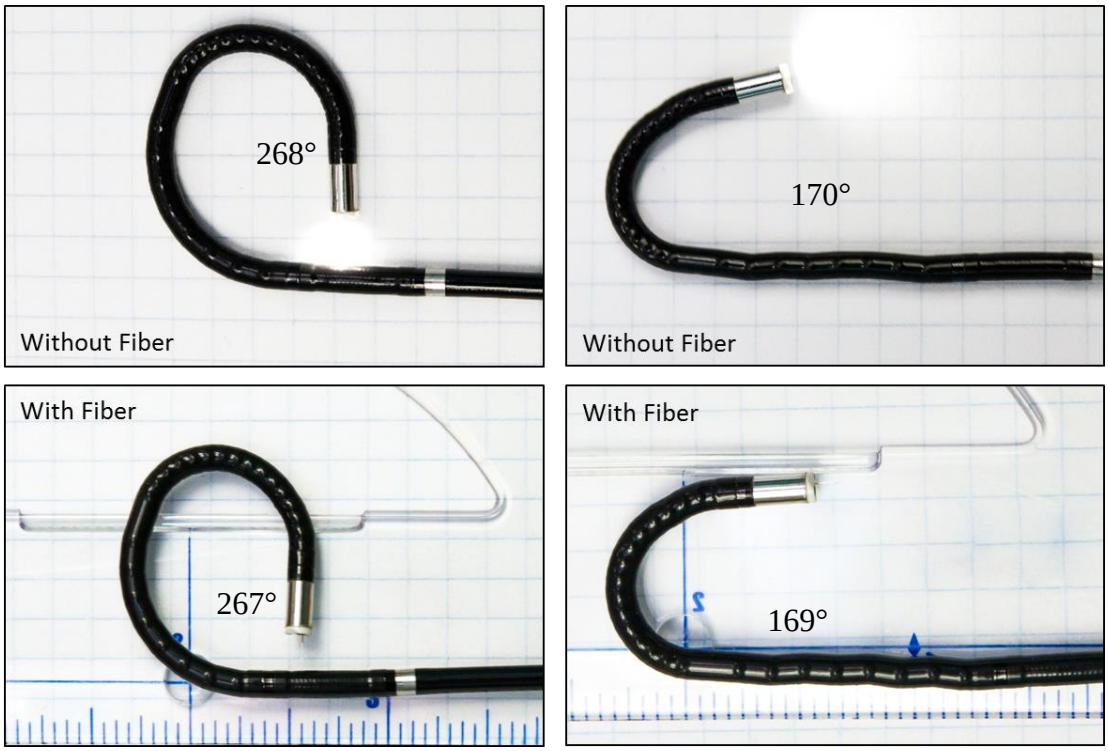

Figure 7.5: Ureteroscope deflection studies conducted with a flexible digital ureteroscope (URF-V, Olympus, Southborough, MA). (A, B) Maximum primary and secondary deflection of flexible ureteroscope with empty working channel (without ball tip fiber inserted through ureteroscope). (C, D) Maximum primary and secondary deflection of flexible ureteroscope with ball tip fiber inserted through ureteroscope. Note that ureteroscope deflection is not significantly affected by the presence of the fiber.

7.3.4 Cavitation Bubble Studies

A stream of cavitation bubbles was observed during delivery of a single 500 μs long TFL pulse in saline (Figure 7.6). Representative images for the ball tip fiber with and without a stone sample, are shown in Figure 7.7ab. The maximum bubble diameter of 600 μm was observed 900 μm from the ball tip, and the bubble stream extended 2400 μm, at t = 440 μs. However, as expected, the presence of the stone altered the geometry of the cavitation bubble. The stone not only impeded cavitation bubble expansion in the forward direction, but also ejected stone material most likely contributed to pressure variations as well. Representative cavitation bubble images near the bare fiber tip both with and without stone sample are also shown for comparison (Figure 7.7cd). For bare tip fiber with similar laser settings, a maximum bubble diameter of 440 μm was observed 460 μm from the fiber tip, and the bubble stream extended for 1080 μm, at t = 280 μs. The cavitation bubble stream length at the bare fiber tip was shorter due to the divergent laser beam exiting the fiber, as compared with the focused beam from the ball tip fiber.

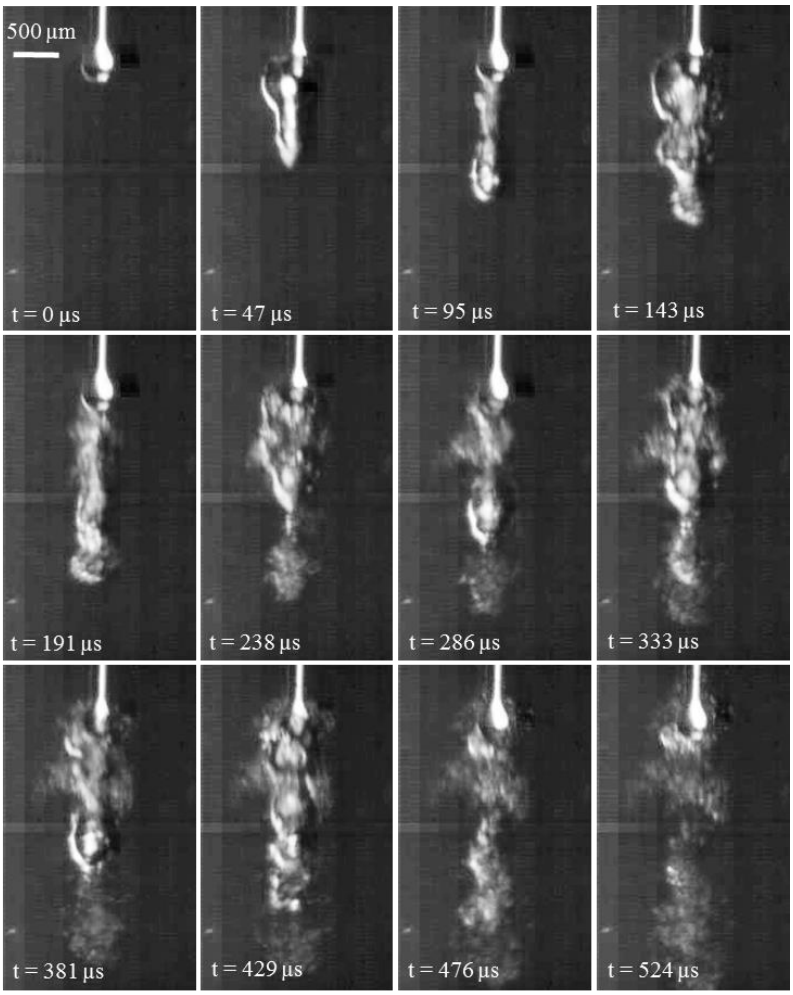

Figure 7.6: Images taken every ~ 50 µs with a high speed camera (105,000 frames per second) of the cavitation bubble dynamics near the distal end of the ball tip fiber during a single 500 µs long Thulium fiber laser pulse.

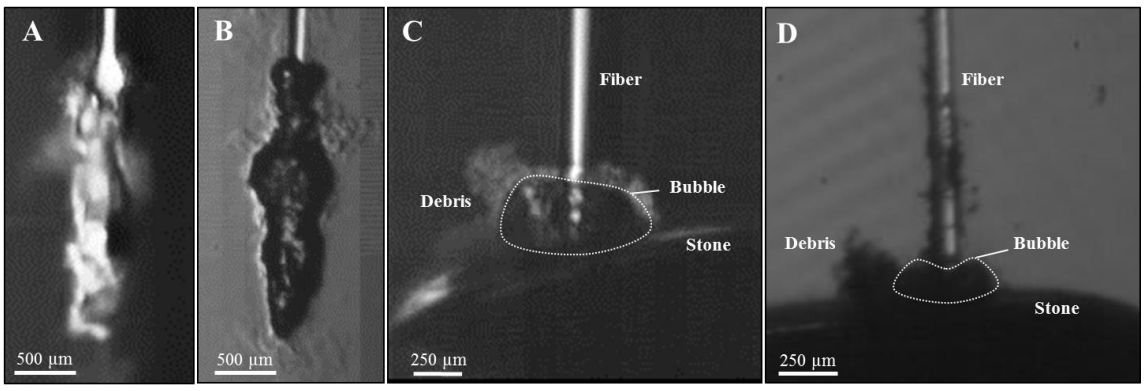

Figure 7.7: (A) Propagation of TFL beam from 100-µm-core / 300-µm-diameter ball tip fiber into saline and subsequent cavitation bubble formation, with bubble stream measuring 2400 µm length by 600 µm width at t = 440 µs. (B) Bubble formation with identical parameters and ball tip fiber placed in contact with stone. (C) Propagation of TFL beam from 100-µm-core bare tip fiber into saline and subsequent cavitation bubble stream at its furthest expansion, measuring 1080 µm length and 440 µm width at t = 280 µs. (D) Bubble formation with identical parameters and bare tip fiber placed in contact with stone.

Beam Propagation Simulations

Ball tip fiber beam propagation was modeled within the geometrical optics limits, using FRED optical engineering software (Photon Engineering, LLC, Tucson, AZ), illustrated in Figures 7.8 (a), 7.9, 7.10, and 7.11. The FRED software package provides the user with a realistic output profile, simulating the propagation of light through an optical system by ray tracing. As the user has full autonomy of selecting sources, geometry, and propagation mediums, one can readily simulate visible beam propagation for comparison with experimental images to determine if the simulation is acceptable for direct comparison with dissimilar immersion mediums and input wavelengths.

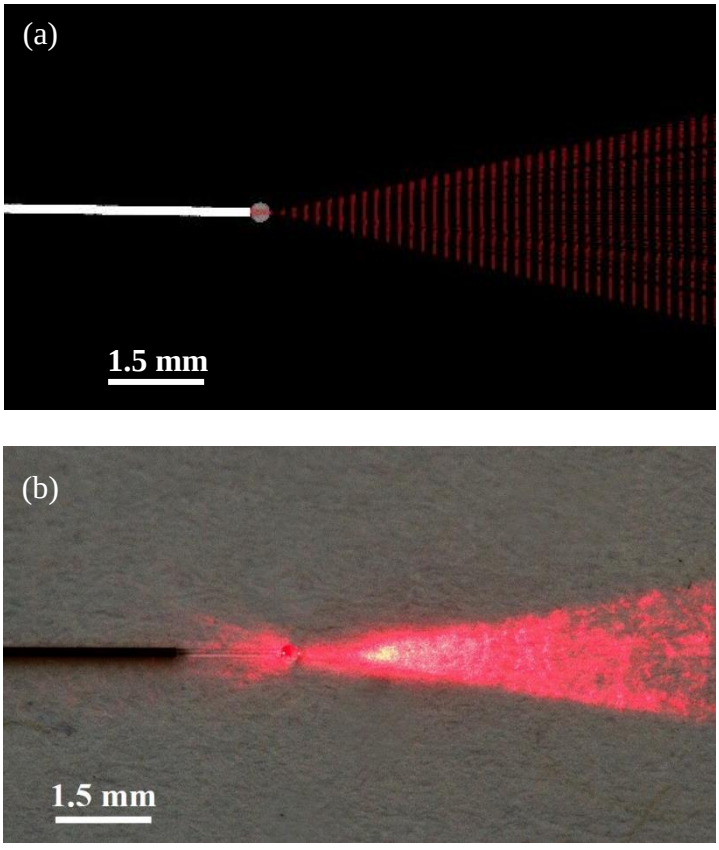

Figure 7.8: (a) Illustration of FRED ray tracing performed to simulate HeNe propagation in air. (b) Propagation of HeNe laser beam through experimental 100-µm-core / 300-µm-diameter ball tip fiber.

Figure 7.8 compares the theoretical HeNe laser propagation based on simulations with the actual propagation presented with an image from experiments. As the two do in fact correspond, we may expect the representation of an IR laser to propagate accurately, even without experimental image comparison. The investigational simulation models output of the 100-Watt Thulium fiber laser (TLR 110-1908, IPG Photonics, Oxford, MA) with a center wavelength of 1908 nm, exhibiting a Gaussian, near single-mode spatial beam profile, originating from a built-in collimator providing a 5.5-mm-diameter output beam. The beam propagates through free space until transmitting through a 25-mm-FL plano-convex lens (representing LA1560-C, Thorlabs, Newton, NJ) to focus the TFL beam down to a $1/e^2$ spot diameter of ~ 25 μm, for coupling into a 100-μm-core, low-OH, silica optical fiber with 300-μm-diameter ball tip (FIPE100140170/2M Ball Lens, Polymicro, Phoenix, AZ). Energy density graphs in Figure 7.10 illustrate ray divergence for both contact mode and 1 mm from the ball surface. All elements with the exception of the tip distal surface are immersed in air, while the final stage demonstrates propagation through saline solution.

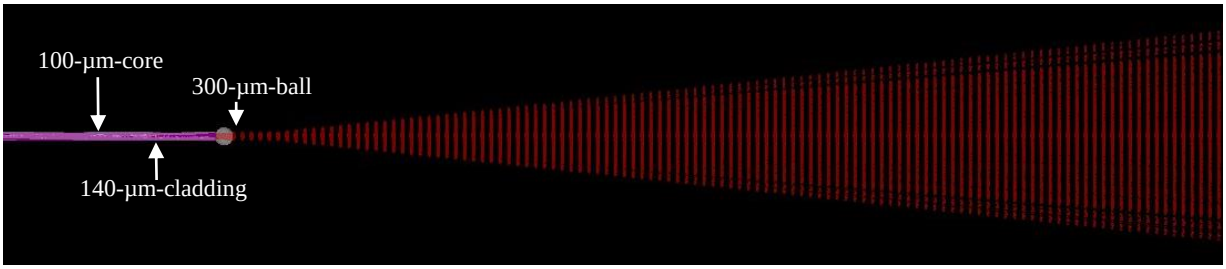

Figure 7.9: Illustration of FRED ray tracing performed to study the beam shape and energy density output as a function of distance.

The energy density simulation graphs pictured in Figure 7.10 do not directly give final values in terms of energy density as the input energies required for beam propagation within the simulation were not representative. However, the footprint extrapolated from the profiles provides cross-sectional information useful for our own z-axis fiber alignment and acceptance cone matching.

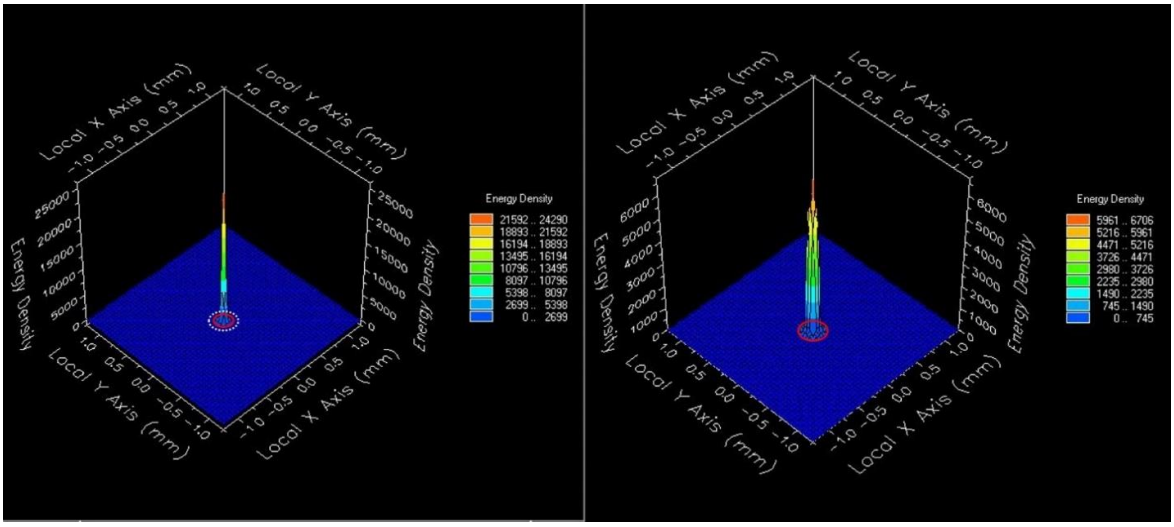

Figure 7.10: Energy density simulation graph of TFL propagation in contact (left) and 1 mm from ball tip surface (right). White dotted circle represents beam footprint at 1 mm overlaid with in-contact beam footprint.

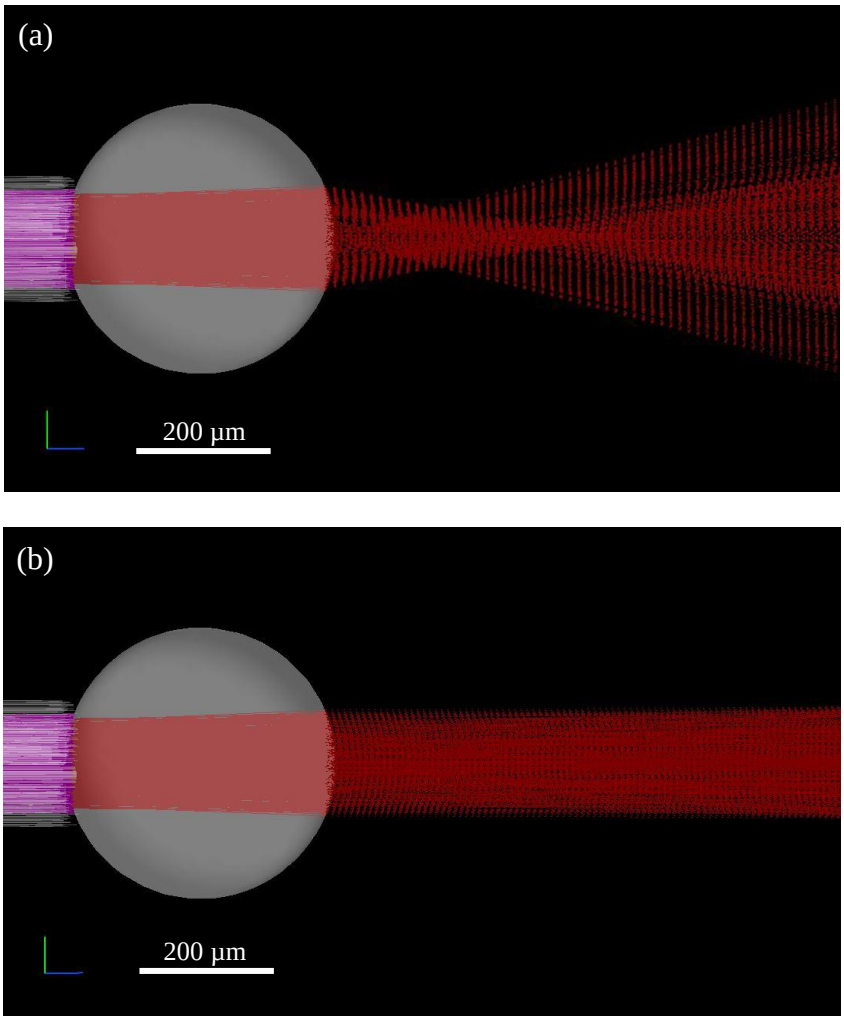

Figure 7.11: (a) Propagation of HeNe laser beam through experimental 100-µm-core / 300-µm-diameter ball tip fiber immersed in air. Circle of least confusion occurs 100 µm from final element surface. (b) Propagation of HeNe laser beam through experimental 100-µm-core / 300-µm-diameter ball tip fiber immersed in saline.

While focusing effects are evident in Figure 7.11 (a), where the ball tip is propagating TFL energy in air, the simulation in which the ball tip is immersed in saline provides a more accurate representation. The beam remains in a semi-collimated state for well past the penetration depth of the TFL in water. Analysis of high speed imaging of ball tip generated cavitation bubbles will provide insight as to where the water and air boundaries exist, allowing for an even more representative model.

7.4 Discussion

TFL procedure times for each data set were comparable to previously reported *in vitro* ureter model results, conducted with similar laser parameters (35 mJ, 500 µs, and 300 Hz) and a bare tip fiber, which reported an operation time of 54 ± 22 s [24]. TFL procedure times are also shorter than the procedure time of 167 ± 41 s previously reported using the conventional Holmium:YAG laser with a separate set of standard clinical parameters of 600 mJ, 350 µs, 6 Hz, and a 270-µm-core optical fiber [24]. It should be noted that Holmium laser lithotripsy using higher pulse energies during preliminary studies did not result in shorter procedure times due to an observed increase in stone retropulsion. The stone particles or dust created during TFL lithotripsy (Figure 7.3) also appear to be smaller than the stone fragments typically produced during conventional Holmium laser lithotripsy, which may potentially translate into lower stone re-treatment rates in the clinic. Initial saline irrigation rate measurements and ureteroscope deflection tests also indicate minimal losses due to the presence of the small ball tip fiber diameter. These results, coupled with stone ablation rate results comparable to bare fiber tips, suggest that ball tip fibers may serve as a viable replacement for traditional bare tip fibers for TFL lithotripsy.

While the stone ablation rates reported with ball tip fibers are promising, the ball tip fiber additionally serves to prevent fiber induced mechanical damage to the inner lining of the ureteroscope working channel and potential perforation of the ureter wall during initial fiber insertion. However, eventual degradation of the ball tips (Figure 7.2 and Table 7.2) with repeated fiber use in contact with multiple stone samples suggests that the current ball tip fiber design dimensions may not be optimal for reducing distal fiber tip

degradation. Several specifications could be altered, including ball tip size and/or shape, as discussed below.

In this study, the ratio of ball tip to fiber (300 μm ball diameter / 140 μm fiber core + cladding diameter) was 2.1. While it may be possible to increase this ratio to about 2.5, there are fundamental limits to the maximum ratio due to several factors. If the ratio is too high, there will be insufficient core and cladding glass material to draw the ball tip during fabrication. The neck or interface between the trunk fiber and ball tip may also become too fragile and susceptible to fracture. It may also be possible to slightly increase both fiber trunk and ball tip diameters (keeping ratio fixed) to yield a more robust fiber optic system resistant to degradation, without completely sacrificing the small fiber dimensions that are advantageous in providing both maximum saline irrigation rates and ureteroscope deflection during TFL laser lithotripsy

Furthermore, ball tip designs used during Holmium laser lithotripsy actually employ a tapered teardrop geometry as opposed to the more spherical experimental design used in our experiments. This teardrop shape may potentially improve its mechanical properties, making the neck or interface between trunk fiber and ball tip more robust for handling, however, it is unclear whether the design aids in increased stone ablation rates as well. Future studies will focus on the dependence of stone ablation and ball tip degradation rates on ball tip diameter and shape.

It should be noted that these preliminary studies were performed with fixed laser parameters (35 mJ, 500 μs, and 300 Hz), based on the optimal stone ablation rates reported during previous studies [24]. However, ball tip degradation rates may potentially be reduced through exploration of a wider range of laser parameters

(including pulse energy, pulse duration, and pulse rate), so that high stone ablation rates are also balanced with fiber longevity.

Exploration of stone ablation rates with the ball tip fiber in non-contact mode is also warranted. Previous studies suggest that TFL lithotripsy can be performed at working distances up to ~ 1 mm with a bare tip fiber, consistent with the length of the cavitation bubble stream observed in this study (Figure 7.6c) [77]. The longer cavitation bubble stream observed using the ball tip fiber (Figure 7.6a) may potentially translate into non-contact TFL lithotripsy at even longer working distances than 1 mm, but this remains to be studied in more detail.

The *in vitro* experimental setup in this study provided realistic manual manipulation of the fiber and imaging of the distal fiber tip after each study. However, this setup did not allow for constant saline irrigation, continuous imaging, or operation through an ureteroscope. A more robust experimental setup may be advantageous for imaging ball tip fiber degradation in real time during lithotripsy and to better understand the physical mechanism for ball tip fiber degradation. Also, stone samples were chosen, in part, for consistency in composition, mass, and diameter, to provide reproducible ablation results. Future studies will utilize a wider range of stone sample sizes and variety of stone compositions to demonstrate clinical viability.

7.5 Conclusion

The 100-µm-core, 300-µm-diameter, ball tip fibers used for TFL lithotripsy rapidly fragmented kidney stones at rates comparable to conventional 100-µm-core bare tip fibers, using laser parameters of 35 mJ, 500 µs, and 300 Hz. While the ball tip fibers did not demonstrate resistance to degradation with repeated use, the spherical geometry provides an additional safety feature for initial fiber insertion through the ureteroscope working channel and into the ureter as well. Additionally, the ball tip fibers used during this preliminary study are also smaller than 240-µm-core, 450-µm-diameter ball tip fibers used during Holmium:YAG laser lithotripsy, which should translate into improved saline irrigation rates and ureteroscope deflection. In summary, the miniature ball tip fiber may provide a cost-effective design for safe fiber insertion through the ureteroscope working channel and into the ureter without risk of instrument damage or tissue perforation, and without compromising stone ablation efficiency during TFL lithotripsy.

CHAPTER 8: CONCLUSIONS

In chapter 2, the Thulium fiber laser was studied as an alternative laser lithotripter to the conventional solid-state, flashlamp-pumped Holmium:YAG laser. TFL operation at pulse rates up to 500 Hz resulted in rapid fragmentation of human uric acid and calcium oxalate monohydrate urinary stones at ablation rates practical for potential use in the clinic.

In chapter 3, we demonstrated that the TFL, operated in low pulse energy and high pulse rate mode, provides a greater safety margin than the clinical gold standard Holmium:YAG laser for lithotripsy. This is apparent from longer TFL ureter perforation times and shorter non-contact working distances for stone basket damage than previously reported with the Holmium laser.

In chapter 4, we verified that the proximal end of a 100-µm-core, low-OH silica fiber can sustain an excess of 3,000,000 pulses without degradation, affirming itself as a candidate for semi-permanent device integration. A novel 1.9 Fr integrated steel-tipped fiber and stone basket device was designed and tested (smaller than current commercially available integrated fiber/basket devices), enabling more efficient TFL ablation of urinary stones with minimal stone retropulsion and improved flexibility, enhanced saline irrigation rates, and decreased fiber burnback, compared to conventional non-integrated fiber and stone baskets. We proposed fiber integration with flexible ureteroscope device.

In chapter 5, we explored ureteroscope illumination optimization for ureteroscope detection for use in thulium laser lithotripsy. The design improved upon traditional scope lighting via ring-illumination style, emulating macro photography techniques. We further studied illumination source optimization via narrow band lighting as a result of white light reflectance spectroscopy measurements.

In chapter 6, we designed and tested a miniaturized ureteroscope polyamide tubing prototype for potential use in TFL lithotripsy, with the ultimate goal of performing office-based laser lithotripsy procedures under mild sedation, yielding 80 % cost savings compared to current OR procedures. Original designs created in a CAD program were translated into FDM and SLA printed prototypes, further progressing toward a fully functional, test ready prototype.

In chapter 7, we tested a 100-µm-core, 300-µm-diameter ball-tip fiber for TFL lithotripsy rapidly fragmented kidney stones at rates comparable to conventional 100-µm-core bare tip fibers at laser parameters of 35 mJ, 500 µs, 300 Hz. While the ball tip fibers did not demonstrate resistance to degradation, the spherical geometry does provide an additional safety feature for initial fiber insertion through the ureteroscope working channel at ablation rates comparable to those of the 100-µm-core traditional fiber used in TFL lithotripsy.

REFERENCES

[1] M. S. Pearle, E. A. Calhoun, and G. C. Curhan, "Urologic diseases in America project: urolithiasis," J. Urol. 173(3), 848–857 (2005).

[2] C. S. Saigal, G. Joyce, and A. R. Timilsina, "Direct and indirect costs of nephrolithiasis in an employed population: opportunity for disease management," Kidney Int. 68(4), 1808–1814 (2005).

[3] C. D. Scales et al., "Prevalence of kidney stones in the United States," Eur. Urol. 62(1), 160–165 (2012).

[4] T. H. Brikowski, Y. Lotan, and M. S. Pearle, "Climate-related increase in the prevalence of urolithiasis in the United States," Proc. Natl. Acad. Sci. 105(28), 9841–9846 (2008).

[5] National Kidney and Urologic Diseases Information Clearinghouse (NKUDIC). (n.d.). (NIH.gov) Retrieved January 21, 2015.

[6] J. C. Sung, W. P. Springhart, C. G. Marguet, J. O. L'Esperance, Y. Tan, D. Albala, and G. M. Preminger, "Location & etiology of flexible & semirigid ureteroscope damage," Urology 66(5), 958-963 (2005).

[7] F. Pasqui, F. Dubosq, K. Tchala, M. Tligui, B. Gattegno, P. Thibault, and O. Traxer, "Impact on active stone deflection and irrigation flow of all endoscopic working tools during flexible ureteroscopy," Eur. Urol. 45(1), 58-64 (2004).

[8] S. Griffin, "Fiber optics for destroying kidney stones," Biophoton. Int. 11(4), 44-47 (2004).

[9] O. A. Nazif, J. M. H. Teichman, R. D. Glickman, and A. J. Welch, "Review of laser fibers: a practical guide for urologists," J. Endourol. 18(9), 818-829 (2004).

[10] A. J. Marks, A. C. Mues, B. E. Knudsen, and J. M. H. Teichman, "Holmium:YAG lithotripsy proximal fiber failures from laser and fiber mismatch," Urology 71(6), 1049-1051 (2008).

[11] B. E. Knudsen, R. D. Glickman, K. J. Stallman, S. Maswadi, B. H. Chew, D. T. Beiko, J. D. Denstedt, and J. M. H. Teichman, "Performance and safety of Holmium:YAG laser optical fibers," J. Endourol. 19(9), 1092-1097 (2005).

[12] G. M. Hale and M. R. Querry, "Optical constants of water in the 200-nm to 200-mm wavelength region," Appl. Opt. 12(3), 555-563 (1973).

[13] E. D. Jansen, T. G. van Leeuwen, M. Motamedi, C. Borst, and A. J. Welch, "Temperature dependence of the absorption coefficient of water for midinfrared laser radiation," Lasers Surg. Med. 14(3), 258-268 (1994).

[14] B. I. Lange, T. Brendel, and G. Huttmann, "Temperature dependence of light absorption in water at holmium and thulium laser wavelengths," Appl. Opt. 41(27), 5797-5803 (2002).

[15] K. T. Schomacker, Y. Domankevitz, T. J. Flotte, and T. F. Deutsch, "Co:MgF2 laser ablation of tissue: effect of wavelength on ablation threshold and thermal damage," Lasers Surg. Med. 11(2), 141-151 (1991).

[16] R. L. Blackmon, P. B. Irby, and N. M. Fried, "Comparison of Holmium:YAG and Thulium fiber laser lithotripsy: ablation thresholds, ablation rates, and retropulsion effects," J. Biomed. Opt. 16(7), 071403 (2011).

[17] Scott NJ, Cilip CM, Fried NM. Thulium fiber laser ablation of urinary stones through small-core optical fibers. IEEE J Sel Top Quantum Electron 2009; 15:435-440.

[18] Blackmon RL, Irby PB, Fried NM. Thulium fiber laser lithotripsy using tapered fibers. Lasers Surg Med 2010; 42:45-50.

[19] Blackmon RL, Hutchens TC, Hardy LA, Wilson CR, Irby PB, Fried NM. Thulium fiber laser ablation of kidney stones using a 50-μm-core silica optical fiber. Opt Eng 2015; 54:011004.

[20] B. Struve G. and Huber, "Properties and medical applications of near-IR solid-state lasers," J. Physique IV 1(C7), 3-6 (1991).

[21] Santa-Cruz RW, Leveillee RJ, Krongrad A. Ex vivo comparison of four lithotripters commonly used in the ureter: what does it take to perforate? J Endourol 1998; 12:417-422.

[22] Sofer M, Watterson JD, Wollin TA, Nott L, Razvi H, Denstedt JD. Holmium: YAG laser lithotripsy for upper urinary tract calculi in 598 patients. J Urol 2002; 167:31-34.

[23] Althunayan AM, Elkoushy MA, Elhilali MM, Andonian S. Adverse events resulting from lasers used in urology. J Endourol 2014; 28:256-260.

[24] Hardy LA, Wilson CR, Irby PB, Fried NM. Thulium fiber laser lithotripsy in an in vitro ureter model. J. Biomed. Opt. 19(12): 128001, 2014.

[25] Lu, M. K., Chang, F. C., Wang, W. Z., Hsieh, C. C., & Kao, F. J. (2014). Compact light-emitting diode lighting ring for video-assisted thoracic surgery. Journal of biomedical optics, 19(10), 105004-105004.

[26] A. J. Hendrikx, W. E. Strijbos, D. W. de Knijff, J. J. Kums, W. H. Doesburg, and W. A. Lemmens, "Treatment for extended-mid and distal ureteral stones: SWL or ureteroscopy? Results of a multicenter trial," J. Endourol. 13(10), 727-733 (1999).

[27] K. Kijvikai, G. E. Haleblian, G. M. Preminger, and J. de la Rosette, "Shock wave lithotripsy or ureteroscopy for the management of proximal ureteral calculi: an old discussion revisited," J. Urol. 178 (4 Pt 1), 1157-1163 (2007).

[28] White MD, Moran ME, Calvano CJ, Borhan-Manesh A, Mehlhaff BA. Evaluation of retropulsion caused by Holmium:YAG laser with various power settings and fibers. J Endourol 1998; 12:183-186.

[29] Lee H, Ryan TR, Teichman JMH, Kim J, Choi B, Arakeri NV, Welch AJ. Stone retropulsion during Holmium:YAG Lithotripsy. J Urol 2003; 169:881-885.

[30] Marguet CG, Sung JC, Springhart WP, L'Esperance JO, Zhou S, Zhong P, Albala DM, Preminger GM. In vitro comparison of stone retropulsion and fragmentation of the frequency doubled, double pulse Nd:YAG laser and the Holmium:YAG laser. J Urol 2005; 173:1797-1800.

[31] Finley DS, Petersen J, Abdelshehid C, Ahlering M, Chou D, Borin J, Eichel L, McDougall E, Clayman RV. Effect of holmium:YAG laser pulse width on lithotripsy retropulsion in vitro. J Endourol 2005; 19:1041-1044.

[32] Kang HW, Lee H, Teichman JM, Oh J, Kim J, Welch AJ. Dependence of calculus retropulsion on pulse duration during Ho:YAG laser lithotripsy. Lasers Surg Med 2006; 38:762-772.

[33] Kalra P, Le NB, Bagley D. Effect of pulse width on object movement in vitro using holmium:YAG laser. J Endourol 2007; 21:228-231.

[34] Elashry OM, Tawfik AM. Preventing stone retropulsion during intracorporeal lithotripsy. Nat Rev Urol 2012; 9(12):691-698.

[35] D. M. Wilson, "Clinical and laboratory approaches for evaluation of nephrolithiasis," J. Urol. 141 (3 Pt 2), 770-774 (1989).

[36] R. L. Blackmon, P. B. Irby, and N. M. Fried, "Holmium:YAG laser lithotripsy at high pulse energies versus Thulium fiber laser lithotripsy at high pulse rates," J. Endourol. 24(12), A#72, 2136-2137 (2010).

[37] Sea Sea J, Jonat LM, Chew BH, Qiu J, Wang B, Hoopman J, Milner T, Teichman JM. Optimal power settings for Holmium:YAG lithotripsy. J Urol 2012;187:914–919.

[38] Cordes J, Lange B, Jocham D, Kausch I. Destruction of stone extraction basket during an in vitro lithotripsy--a comparison of four lithotripters. J Endourol 2011; 25:1359-1362.

[39] Cordes J, Nguyen F, Lange B, Brinkmann R, Jocham D. Damage of stone baskets by endourologic lithotripters: a laboratory study of 5 lithotripters and 4 basket types. Adv Urol 2013; 632790:1-6.

[40] Bader MJ, Gratzke C, Hecht V, Schlenker B, Seitz M, Reich O, Stief CG, Sroka R. Impact of collateral damage to endourologic tools during laser lithotripsy--in vitro comparison of three different clinical laser systems. J Endourol 2011; 25:667-672.

[41] Freiha GS, Glickman RD, Teichman JM. Holmium:YAG laser-induced damage to guidewires: experimental study. J Endourol 1997; 11:331-336.

[42] Honeck P, Wendt-Nordahl G, Hacker A, Alken P, Knoll T. Risk of collateral damage to endourologic tools by holmium:YAG laser energy. J Endourol 2006; 20:495-497.

[43] Fried NM, Tesfaye Z, Ong AM, Rha KH, Hejazi P. Optimization of the Erbium: YAG laser for precise incision of ureteral and urethral tissues: In vitro and in vivo results. Lasers Surg Med 2003; 33:108-114.

[44] Hardy LA, Wilson CR, Irby PB, Fried NM. Rapid vaporization of kidney stones, ex vivo, using a thulium fiber laser opperated at pulse rates up to 500 Hz using a stone basket. IEEE J Sel Top Quantum Electron 2014; 20:0902604.

[45] Molina WR, Silva IN, da Silva RD, Gustafson D, Sehrt D, Kim FJ. Influence of saline on temperature profile of laser lithotripsy activation. J Endourol 2014 Oct. 10 [Epub].

[46] Blackmon RL, Case JR, Trammell SR, Irby PB, Fried NM. Fiber optic manipulation of urinary stone phantoms using Holmium:YAG and Thulium fiber lasers. J Biomed Opt 2013;18:028001.

[47] Chan KF, Vassar GJ, Pfefer TJ, Teichman JMH, Glickman RD, Weintraub ST, Welch AJ. Holmium:YAG laser lithotripsy: A dominant photothermal ablative mechanism with chemical decomposition of urinary calculi. Lasers Surg Med 1999;25:22–37.

[48] Asshauer T, Rink K, Delacretaz G. Acoustic transient generation by holmium laser induced cavitation bubbles. J Appl Phys 1994;76:5007–5013.

[49] Brinkmann R, Hansen C, Mohrenstecher D, Scheu M, Birngruber R. Analysis of cavitation dynamics during pulsed laser tissue ablation by optical on-line monitoring. IEEE J Sel Top Quantum Electron 1996;2:826–835.

[50] Vogel A, Venugopalan V. Mechanisms of pulsed laser ablation of biological tissues. Chem Rev 2003;103:577–644.

[51] H. Lee, R. T. Ryan, J. M. Teichman, J. Landman, R. V. Clayman, T. E. Milner, and A. J. Welch, "Effect of lithotripsy on holmium: YAG optical beam profile," J. Endourol. 17(2), 63-67 (2003).

[52] A. C. Mues, J. M. H. Teichman, and B. E. Knudsen, "Quantification of holmium:yttrium aluminum garnet optical tip degradation," J. Endourol. 23(9), 1425-1428 (2009).

[53] B. E. Knudsen, R. Pedro, B. Hinck, and M. Monga, "Durability of reusable holmium:YAG laser fibers: a multicenter study," J. Urol. 185(1), 160-163 (2011).

[54] T. C. Hutchens, R. L. Blackmon, P. B. Irby, and N. M. Fried, "Hollow steel tips for reducing distal fiber burn-back during thulium fiber laser lithotripsy," J. Biomed. Opt. 18(7), 078001-078001 (2013).

[55] T. C. Hutchens, R. L. Blackmon, P. B. Irby, and N. M. Fried**, "**Detachable fiber optic tips for use in Thulium fiber laser lithotripsy," J. Biomed. Opt. 18(3), 038001 (2013).

[56] U. Nagele, M. Horstmann, J. Hennenlotter, U. Walcher, M. A. Kucyk, K. D. Sievert, A. Stenzl, and A G. Anastasiadis, "Size does matter: 1.5 Fr stone baskets almost double irrigation flow during flexible ureteroscopy compared to 1.9 Fr stone baskets," Urol. Res. 34(6), 389-392 (2006).

[57] T. Bach, B. Geavlete, T. W. R. Herrman, and A. J. Gross, "Working tools in flexible ureterorenoscopy – influence on flow and deflection: What does matter?" J. Endourol. 22(8), 1639-1643 (2008).

[58] J. Bedke, U. Leichtle, A. Lorenz, U. Nagele, A. Steinzl, and S. Kruck, "1.2 French stone retrieval baskets further enhance irrigation flow in flexible ureterorenoscopy," Urolithiasis 41(2), 153-157 (2013).

[59] A. C. Mues, J. M. H. Teichman, and B. E. Knudsen, "Quantification of holmium:yttrium aluminum garnet optical tip degradation," J. Endourol. 23(9), 1425-1428 (2009).

[60] S. M. Al-Qahtani, B. Geavlete, S. G. de Medina SG, O. P. Traxer OP, "The new Olympus digital flexible ureteroscope (URF-V): Initial experience," Urology Annals 3(3), 133-137 (2011).

[61] R. L. Blackmon, P. B. Irby, and N. M. Fried, "Holmium:YAG (λ = 2120 nm) versus Thulium fiber (λ = 1908 nm) laser lithotripsy," Lasers Surg. Med. 42(3), 232-236 (2010).

[62] R. L. Blackmon, P. B. Irby, and N. M. Fried, "Enhanced thulium fiber laser lithotripsy using micro-pulse train modulation," J. Biomed. Opt. 17(2), 028002 (2012).

[63] Bryan RT, Billingham LJ, Wallace DM. Narrow-band imaging flexible cystoscopy in the detection of recurrent urothelial cancer of the bladder. BJU Int 2007;101:702–6.

[64] Herr HW, Donat SM. A comparison of white-light cystoscopy and narrow-band imaging cystoscopy to detect bladder tumour recurrences. BJU Int 2008;102:1111–4.

[65] Cauberg, E. C., de Bruin, D. M., Faber, D. J., van Leeuwen, T. G., de la Rosette, J. J., & de Reijke, T. M. (2009). A new generation of optical diagnostics for bladder cancer: technology, diagnostic accuracy, and future applications. European urology, 56(2), 287-297.

[66] Inoue T, Murano M, Murano N, et al. Comparative study of conventional colonoscopy and pan-colonic narrow-band imaging system in the detection of neoplastic colonic polyps: a randomized, controlled trial. J Gastroenterol 2008;43:45–50.

[67] Sharma P, Bansal A, Mathur S, et al. The utility of a novel narrow band imaging endoscopy system in patients with Barrett's esophagus. Gastrointest Endosc 2006;64:167–75.

[68] Kuznetsov K, Lambert R, Rey JF. Narrow-band imaging: potential and limitations. Endoscopy 2006;38:76–81.

[69] Song LM, Adler DG, Conway JD, et al. Narrow band imaging and multiband imaging. Gastrointest Endosc 2008;67:581–9.

[70] Olympus. (2016, January 2). NBI for enhancing the visualization of the capillary network and mucosal morphology. [Online]. Available: http://www.olympus-global.com/en/technology/technology/luceraelite/

[71] Lange, B., Jocham, D., Brinkmann, R., & Cordes, J. (2014). Stone/tissue differentiation during intracorporeal lithotripsy using diffuse white light reflectance spectroscopy: In vitro and clinical measurements. Lasers in surgery and medicine, 46(8), 614-619.

[72] Wallace, M. B., Wax, A., Roberts, D. N., & Graf, R. N. (2009). Reflectance Spectroscopy. Gastrointestinal Endoscopy Clinics of North America, 19(2), 233–242. http://doi.org/10.1016/j.giec.2009.02.008

[73] Lange, B., Cordes, J., & Brinkmann, R. (2015). Stone/tissue differentiation for holmium laser lithotripsy using autofluorescence. Lasers in surgery and medicine, 47(9), 737-744.

[74] Ocean Optics. (2015, December 23) Reflectance and Transmittance. [Online]. Available: http://oceanoptics.com/measurementtechnique/reflectance-transmittance/

[75] M.E. Dailey, et al. Nikon. (2015, December 21) The Automatic Microscopic. [Online]. Available: http://www.microscopyu.com/articles/livecellimaging/automaticmicroscope.html

[76] S. G. Hubosky, K. A. Healy, M. Grasso, and D. H. Bagley, "Accessing the difficult ureter and the importance of ureteroscope miniaturization: history is repeating itself," Urology, 84(4), 740-742 (2014).

[77] C.R. Wilson, L.A. Hardy, P.B. Irby, and N.M. Fried, "Collateral damage to the ureter and Nitinol stone baskets during Thulium fiber laser lithotripsy," Lasers Surg. Med. 47(5): 403-410 (2015).

[78] C.R. Wilson, T.C. Hutchens, L.A. Hardy, P.B. Irby, and N.M. Fried, "A Miniaturized, 1.9F Integrated Optical Fiber and Stone Basket for Use in Thulium Fiber Laser Lithotripsy," J. Endourology. 29(10), 1110-1114 (2015).

[79] Haberman, K., Ortiz-Alvarado, O., Chotikawanich, E., & Monga, M. (2011). A dual-channel flexible ureteroscope: evaluation of deflection, flow, illumination, and optics. Journal of Endourology, 25(9), 1411-1414.

[80] Ortiz-Alvarado The Cobra Dual-Channel Flexible Ureteroscope: Novel Function, Novel Applications

[81] Caballero, J. P., Galán, J. A., Verges, A., Amorós, A., & Garcia-Segui, A. (2015). Micro-ureteroscopy: Initial experience in the endoscopic treatment of pelvic ureteral lithiasis. Actas Urológicas Españolas (English Edition).

[82] Formlabs. (2015, November 7). Formlabs Form 1+ High Resolution 3D Printer. [Online]. Available: http://formlabs.com/products/3d-printers/form-1-plus/

[83] M. R. Prince, G. M. LaMuraglia, C. E. Seidlitz, S. Prahl, C. Athanasoulis, and R. Birngruber, "Ball-tipped fibers for laser angioplasty with the pulsed-dye laser," IEEE J. Sel. Top. Quantum Electron. 26 (12), 2297-2304 (1990).

[84] R. M. Verdaasdonk, F. C. Holstege, E. D. Jansen, and C. Borst, "Temperature along the surface of modified fiber tips for Nd: YAG laser angioplasty," Lasers Surg. Med. 11(3), 213-222 (1991).

[85] W. P. Vandertop, R. M. Verdaasdonk, and C. F. van Swol, "Laser-assisted neuroendoscopy using a neodymium-yttrium aluminum garnet or diode contact laser with pretreated fiber tips," J. Neurosurg. 88(1), 82-92 (1998).

[86] A. Cavallini, D. Marcer, G. Bernardini, and S. F. & Ruffino, "Endovenous laser ablation of great saphenous veins performed using tumescent cold saline solution without local anesthesia," Ann. Vasc. Surg. 28(4), 951-956 (2014).

[87] A. Cavallini, D. Marcer, and S. F. Ruffino, "Endovenous ablation of incompetent saphenous veins with a new 1,540-nanometer diode laser and ball-tipped fiber," Ann. Vasc. Surg. 28(3), 686-694 (2014).

[88] A. Cavallini, D. Marcer, and S. F. Ruffino, "Endovenous treatment of incompetent anterior accessory saphenous veins with a 1540 nm diode laser," Int. Angiol. (2014).

[89] M. Hirokawa and N. Kurihara, "Comparison of bare-tip and radial fiber in endovenous laser ablation with 1470 nm diode laser," Ann. Vasc. Dis. 7(3), 239 (2014).

[90] T. R. Herrmann, T. Bach, F. Imkamp, C. von Klot, H. Tezval, U. Nagele, and A. J. Gross, "Insertion sheaths prevent breakage of flexible ureteroscopes due to laser fiber passage: a video-endoluminal study of the working channel," J. Endourol. 24(11), 1747-1751 (2010).

[91] C. Sung, H. Singh, M. Schwartz, G. Mirabile, G. W. Hruby, C. D. Ryan, and J. Landman, "Evaluation of efficacy of novel optically activated digital endoscope protection system against laser energy damage," Urology 72(1), 57-60 (2008).

[92] E. Durak, G. Hruby, R. Mitchell, F. Marruffo, J. O. Abundez, and J. Landman, "Evaluation of a protective laser sheath for application in flexible ureteroscopy," J. Endourol. 22(1), 57-60 (2008).

[93] R. A. Chapman, B. K. Somani, A. Robertson, S. Healy, and S. G. Kata, "Decreasing cost of flexible ureterorenoscopy: single-use laser fiber cost analysis," Urology 83(5), 1003-1005 (2014).

[94] A. Lusch, C. Abdelshehid, M. A. Liss, R. Alipanah, E. M. McDougall, and J. Landman, "In vitro evaluation of ScopeSafe fibers and the Scope Guardian sheath in prevention of ureteroscope endolumenal working damage," J. Endourol 27(6), 768-773 (2013).

[95] R. Shin, J. Lautz, F. Cabrera, Z. Goldsmith, N. Kuntz, R. Youssef, A. Neisius, C. Scales, M. Ferrandino, P. Zhong, W. Simmons, G. Preminger, and M. Lipkin, "Ball-tip holmium laser fiber: in vitro stone comminution and fiber tip degradation," J. Urol. 191 (4S), e947 (2014).

[96] B. Knudsen, S. De, and M. Monga, "Ball tipped holmium: YAG optical fiber: pulse energy settings increase degradation during clinical use," J. Urol. 191 (4s), e947 (2014).

[97] S. Johnson, D. Lew, C. Davis, and A. Guise, "The impact on cost and frequency of ureteroscope repairs using a ball-tipped laser fiber for ureteroscopy," J. Urol. 191 (4s), e948 (2014).

[98] S. Tarplin, N. Farrell, M. Monga, and B. Knudsen, "Ball tipped Holmium:YAG optical fibers for flexible ureteroscopy: Is there a difference?" J. Urol. 193 (4S), e888 (2015).

[99] P. Kronenberg and O. Traxer, "Lithotripsy performance of traditional and special designed laser fibers," J. Urol. 193 (4s), e413 (2015).

[100] E. C. Akar and B. E. Knudsen, "Evaluation of 16 new Holmium:Yttrium-Aluminum-Garnet laser optical fibers for ureteroscopy," Urology 86, 230-235 (2015).

[101] R. H. Shin, J. M. Lautz, F. Cabrera, C. J. Shami, Z. Goldsmith, N. Kuntz, A. G. Kaplan, A. Nelsius, W. N. Simmons, G. M. Preminger, and M. E. Lipkin, "Evaluation of a novel ball tip holmium laser fiber: impact on ureteroscope performance and fragmentation efficiency," J. Endourol. Epub (2015).

[102] R. M. Verdaasdonk, J. Klaessens, R. de Roode, T. de Boorder, and J. Blanken, "Dynamic change of characteristics of (modified) fiber tips used with micro second pulsed lasers in a liquid environment influencing the effectiveness and safety of treatment," Proc. SPIE 6435, 64350S1-8 (2007).

[103] P. M. Verdaasdonk and C. Borst, "Ray tracing of optically modified fiber tips. 1: spherical probes," Appl. Opt. 30(16), 2159-2171 (1991).

[104] C. R. Wilson, L. A. Hardy, P. B. Irby, and N. M. Fried, "Comparison of proximal fiber tip damage during Holmium:YAG and Thulium fiber laser lithotripsy," Engineering and Urology Society annual meeting, New Orleans, LA (2015).

[105] Welch, A. J., & Van Gemert, M. J. (Eds.). (1995). Optical-thermal response of laser-irradiated tissue (Vol. 1). New York: Plenum press.

[106] C. R. Wilson, T. C. Hutchens, L. A. Hardy, P. B. Irby, and N. M. Fried, “A miniaturized 1.9 French integrated optical fiber and stone basket for use in Thulium fiber laser lithotripsy,” J. Endourol. 29(10), 1110-1114 (2015).

APPENDIX A: LIST OF PEER-REVIEWED PUBLICATIONS

[1] Hardy LA, **Wilson CR**, Irby PB. Fried NM. Rapid vaporization of kidney stones, ex vivo, using a thulium fiber laser operated at pulse rates up to 500 Hz using a stone basket. IEEE J. Sel. Top. in Quantum Electron. 20(5), 0902604, 2014.

[2] Hardy LA, **Wilson CR**, Irby PB. Fried NM. Thulium fiber laser lithotripsy in an in vitro ureter model. J. Biomed. Opt. 19(12): 128001, 2014.

[3] Blackmon RL, Hutchens TC, Hardy LA, **Wilson CR**, Irby PB, Fried NM. Thulium fiber laser ablation of kidney stones using a 50-μm-core silica optical fiber. Opt. Eng. 54(1): 011004, 2015.

[4] **Wilson CR**, Hardy LA, Irby PB, Fried NM. Collateral damage to the ureter and Nitinol stone baskets during Thulium fiber laser lithotripsy. Lasers Surg. Med. 47(5): 403-410, 2015.

[5] **Wilson CR**, Hutchens TC, Hardy LA, Irby PB, Fried NM. A miniaturized, 1.9 french integrated optical fiber and stone basket for use in thulium fiber laser lithotripsy. J. Endourol. 29(10): 1110-1114, 2015.

[6] **Wilson CR**, Hardy LA, Kennedy JD, Irby PB, Fried NM. Miniature ball tip optical fibers for use in Thulium fiber laser ablation of kidney stones. J. Biomed. Opt. 21(1): 018003, 2016.

[7] **Wilson CR**, Hardy LA, Irby PB, Fried NM. Microscopic analysis of laser-induced proximal fiber tip damage during Holmium:YAG and Thulium fiber laser lithotripsy. Opt. Eng. (In Press).

[8] Hardy LA, Kennedy JD, **Wilson CR**, Irby PB, Fried NM. Cavitation bubble dynamics during thulium fiber laser lithotripsy. J. Biophotonics. (Submitted).

APPENDIX B: LIST OF CONFERENCE PROCEEDINGS

[1] **Wilson CR**, Hutchens TC, Hardy LA, Irby PB, Fried NM. A permanently integrated fiber and stone basket for thulium fiber laser lithotripsy. Proc. SPIE 8926-56, 2014.

[2] Hardy LA, **Wilson CR**, Irby PB. Fried NM. Rapid vaporization of kidney stones, ex vivo, using a thulium fiber laser operated at pulse rates up to 500 Hz. Proc. SPIE 8926-65, 2014.

[3] **Wilson CR**, Hardy LA, Irby PB, Fried NM. Thulium fiber laser damage to Nitinol stone baskets. Proc. SPIE 9303-1A, 2015.

[4] Hardy LA, **Wilson CR**, Irby PB. Fried NM. Kidney stone ablation times and peak saline temperatures during Holmium:YAG and Thulium fiber laser lithotripsy, ex vivo, in a ureteral model. Proc. SPIE 9303-10, 2015.

[5] Cilip CM, Hutchens TC, Kerr D, Latimer C, Rosenbury SB, Giglio NC, Schweinsberger GR, Perkins WC, **Wilson CR,** Ward A, Nau WH, Fried NM. Infrared laser sealing of porcine tissues: preliminary in vivo studies. Proc. SPIE 9303-19, 2015.

[6] **Wilson CR**, Hardy LA, Irby PB, Fried NM. Thulium fiber laser induced damage to porcine ureter, in vitro. Proc. SPIE 95420C, 2015. (Invited Paper)

[7] Chang CH, **Wilson CR**, Fried NM. Comparison of four lasers (λ = 647, 808, 980, and 1075 nm) for noninvasive creation of deep subsurface lesions in tissue. Proc. SPIE 95420G, 2015.

[8] **Wilson CR**, Hardy LA, Irby PB, Fried NM. Thulium fiber laser lithotripsy using miniature ball tip optical fibers. Proc. SPIE 96891G, 2016.

[9] **Wilson CR**, Hardy LA, Irby PB, Fried NM. Proximal fiber optic tip degradation during Holmium:YAG and Thulium fiber laser lithotripsy. Proc. SPIE 96891B, 2016.

[10] Hardy LA, **Wilson CR**, Irby PB. Fried NM. Cavitation bubble dynamics during thulium fiber laser lithotripsy. Proc. SPIE 96891Q, 2016.

[11] Chang CH, **Wilson CR**, Fried NM. Comparison of diffusing and side-firing laser balloon catheters for creation of subsurface thermal lesions in tissue. Proc. SPIE 96891S, 2016.